Interactions between SOFC Interconnect Spinel Coating Materials and Chromia

by

Yingjia Liu

A dissertation submitted to the Graduate Faculty of
Auburn University
in partial fulfillment of the
requirements for the Degree of
Doctor of Philosophy

Auburn, Alabama
December 8, 2012

Keywords: SOFC interconnect, interaction, $(Mn,Co)_3O_4$ coating, Cr_2O_3 oxidation layer, doping

Approved by

Jeffrey W. Fergus, Chair, Professor of Materials engineering
Bart Prorok, Associate Professor of Materials engineering
Dong-Joo Kim, Associate Professor of Materials engineering
Curtis Shannon, Professor of Chemistry and biochemistry

Abstract

The SOFC technology has been developed toward lower operation temperature in the range of 500^{o}C - 800^{o}C, which brings wider materials choice for the interconnect. Ferritic stainless steels have been widely used as SOFC interconnect candidates, but their high temperature oxidation and chromium volatilization can lead to cathode poisoning and cell degradation. Applying ceramic conductive coating is an effective technique to protect the metallic interconnects, and manganese cobalt spinel oxides $Mn_{1.5}Co_{1.5}O_4$ have demonstrated promising performances as coating material. However, the reasons for their excellent properties have not been completely understood.

This work aims to provide a fundamental understanding of $(Mn,Co)_3O_4$ coating in high-temperature operation, and to improve the performance of protective coatings. The interactions between $(Mn,Co)_3O_4$ spinel coatings and chromia at high temperature were investigated, and Chapter 2 discusses the mass transport behavior. The interactions lead to the change in chemical composition and microstructure of the original coating. To evaluate the long-term stability, the properties of the reaction layer need further characterization. Chapter 3 focuses on the effect of chromium doping on the electrical conductivity, cation distributions and thermal expansion of $Mn_{1.5}Co_{1.5}O_4$ at SOFC operation condition. The relationship of cation distributions with transport properties in the reaction layer was also discussed. In addition, the effects of different transition metal dopants in the spinel coating material on the mass transport behavior were studied to identify the improved coatings. The effects of iron doping in spinel oxides are investigated on

transport behavior in the interaction, and compared with that of titanium doping in Chapter 4. The interaction of nickel or copper substituted $(Mn,Co)_3O_4$ with chromia at high temperature are evaluated in Chapter 5. The differences in the mass transport behavior of transition metal dopants studied in this work provide helpful information on selection in novel spinel coatings.

Acknowledgments

I would like to express my genuine gratitude to my advisor, Dr. Jeffrey Fergus, for his academic guidance and support. His constructive suggestions helped me a lot in my research work and dissertation writing. Besides the knowledge of materials science, the research attitude he conveyed is the most important spirit I learn from him during these years.

I also want to thank my committee member, Dr. Dong-Joo Kim, Dr. Bart Prorok and Dr. Curtis Shannon for their valuable advices and insight, which is beneficial to finish this dissertation. The appreciation will also be given to the outside reader Dr. Wei Zhan for his kind help in this work.

I would like to further thank Dr. Clarina Dela Cruz at Oak Ridge National Laboratory for providing me great help in analyzing the samples with neutron diffraction.

The special thanks are given to Dr. Kangli Wang, who helped me a lot on the chromium reaction experiment at the early stage of this work, and gave me useful discussions. Besides, I also thank Dr. Yu Zhao, Henglong Wang, Alex, et al., for helping me solve problems during my research. The friendship from my friends in Materials Engineering is highly appreciated. I enjoy the happy time in Auburn during my PhD study.

I also acknowledge the financial support from the Department of Energy through the Building EPSCoR-State/Nation Laboratory Partnerships Program.

Last but not least, I would like to express my great gratitude to my family for their consistent company, love and encouragement which enable me to discover life is always beautiful.

Table of Contents

List of Tables

List of Figures

List of Abbreviations

SOFC	Solid Oxide Fuel Cell
PEM	Proton Exchange Membrane
8-YSZ	8 mol% Yttria-stabilized Zirconia
VOC	Volatile Organic Carbon
TPB	Three Phase Boundary
APU	Auxiliary Power Unit
CHP	Combined Heat and Power Generation
OCV	Open Circuit Potential
CTE	Coefficient of Thermal Expansion
AE	Alkaline Earth
TM	Transition Metal
ODS	Oxide Dispersion Strengthened
DBTT	Ductile-to-Brittle Transition Temperature
BCC	Body Centered Cubic
FCC	Face Centered Cubic
ASR	Area Specific Resistance
FSS	Ferritic Stainless Steel
ASS	Austenitic Stainless Steel
LSM	Lanthanum Strontium Manganite
MOCVD	Metal Organic Chemical Vapour Deposition

RF	Radio-Frequency
APS	Atmospheric Plasma Spraying
SEM	Scanning Electron Microscope
EDS	Energy-Dispersive X-ray Spectroscopy
XRD	X-Ray Diffraction

CHAPTER 1

Introduction

It is a severe challenge for people to achieve sustainable development, and energy is one of these key issues that have to be considered due to resource shortage.[1] Therefore, it is necessary to develop new energy resources and materials.

Fuel cells are promising energy conversion devices that can produce electrical energy directly from chemical energy through electrochemical processes.[2] Due to their high energy conversion efficiency, low emissions and little pollution, they have become more and more attractive throughout the world.

1.1 Background of SOFC

Solid oxide fuel cells (SOFCs) are one kind of fuel cells. A SOFC stack usually consists of four key components, including the anode, cathode, electrolyte and interconnects. Unlike other fuel cells (except proton exchange membrane (PEM) fuel cell), SOFCs are all-solid-state configurations. The most widely used materials for SOFC components are: 8 mol% yttria-stabilized zirconia (8-YSZ) electrolyte, nickel/yttria-zirconia cermet anode (Ni/ZrO_2), strontium-doped lanthanum manganite ($La_{1-x}Sr_xMnO_3$) cathode and doped lanthanum chromite ($LaCrO_3$) interconnect.[3] The solid-state characteristic of cell

components gives little restriction that required on the cells' design. Currently, there are four common stack configurations for SOFCs' fabrication: sealless tubular design, segmented-cell-in-series design, monolithic design, and flat-plate design. [4] Among all the configurations, it is reported by Mori et al that the planner cell design exhibits highest power density, shortest conductive path and lowest production cost. [5] The schematic diagram of a planar SOFC structure is shown in Fig. 1.1. [6]

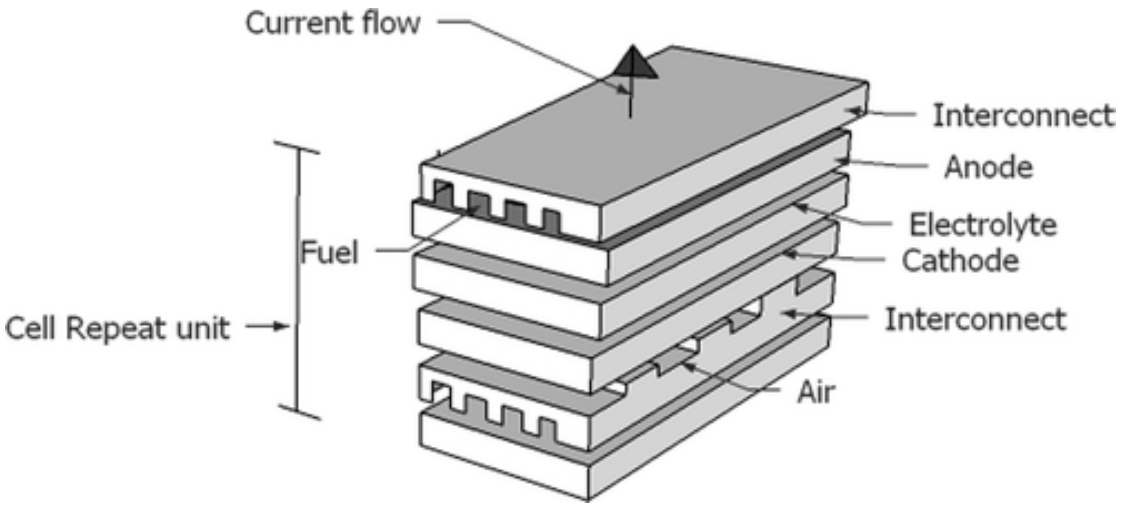

Fig. 1.1 Schematic diagram of a planar SOFC structure. Adapted with permission from D. Bhattacharyya, and R. Rengaswamy 2009, [6] Courtesy American Chemical Society.

A SOFC unit contains two porous electrodes separated by a gas-tight oxygen-conducting electrolyte. During operation, fuel gas, such as hydrogen, methane, and carbon monoxide is fed into the anode (fuel electrode). On the other side, the air containing oxygen is supplied to the cathode (air electrode), where the oxygen (O_2) is reduced to the ions (O^{2-}). The ions of oxygen pass through the electrolyte to the interface of electrolyte and anode, and react with the fuel which is then oxidized. Simultaneously the electrons (e) are released. The solid

electrolyte is nonconductive to electrons, so if there exists an external electrical connection between the cathode and anode for the electrons to flow through, direct current will be produced. All the reactions happen at the three phase boundaries (TPBs), where gas, electrolyte, and porous electrode meet together. The total reactions of different fuels can be expressed by the following equations:

$$H_2+O_2 \rightarrow 2H_2O \quad (1.1)$$

$$CH_4+2O_2 \rightarrow 2H_2O+CO_2 \quad (1.2)$$

$$2CO+O_2 \rightarrow 2CO_2 \quad (1.3)$$

The principles of electrochemical processes with hydrogen as fuel in SOFC are illustrated in Fig. 1.2. [7]

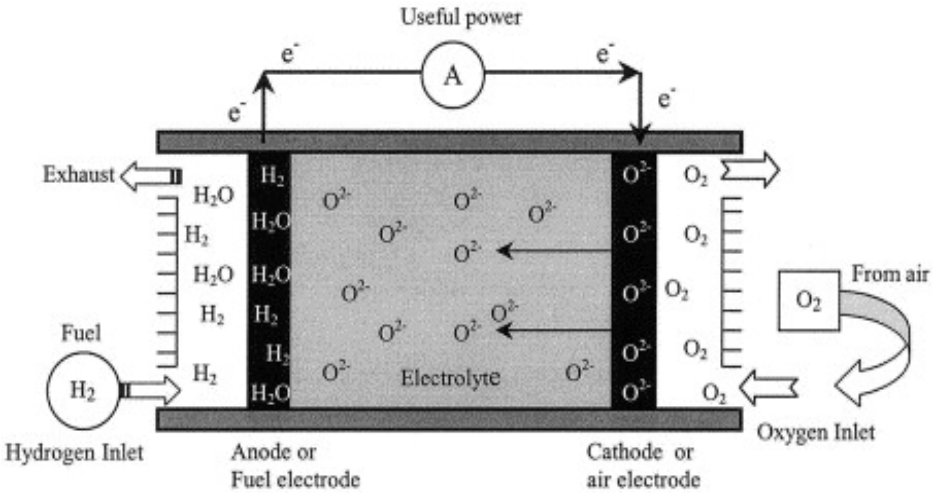

Fig. 1.2 Schematic diagram of SOFC principles. Adapted from A. Boudghene Stambouli, and E. Traversa 2002, [7] Courtesy Elsevier.

The internal electrochemical reactions make the SOFC quite unlike the conventional combustion engine. Because the SOFC converts the chemical energy into electrical energy without fuel combustion as an intermediate step, its conversion efficiency is not subject to the

Carnot limitation.[4] Similar to other fuel cells, SOFC has much low level of pollutants (e.g., SO_x, NO_x, volatile organic carbon (VOC)). However it shows more unique advantages. Its high working temperature, 500 ^oC - 1000 ^oC, promotes rapid reaction kinetics, realizes hydrocarbon fuels reforming within SOFC (internal reforming), and produces high-quality byproduct heat suitable for use in cogeneration or bottoming cycle. [2] It has higher energy conversion efficiency, 70-80%, compared with other kinds of fuel cells. [8] Besides, its solid-state construction gives SOFC more merits like modular construction, non-erosion, and reliability during operation. It can be used as auxiliary power unit (APU) in vehicles and trucks, combined heat and power generation (CHP) devices, or battery replacements on remote sites. Due to its superior performance and promising potential, SOFC technology is being extensively developed for military, residential and industrial applications. [9,10]

1.2 Interconnect of SOFC

1.2.1 Materials requirements for SOFC interconnect

High temperature operation makes the SOFC work higher efficient, but also limits its choice of material, so the major challenge of the SOFC is to develop suitable component materials. [3,4] The interconnect is a critical part in the SOFC. An open circuit potential (OCV) of a single hydrogen-air SOFC at 1000^oC is about 1V. To obtain higher voltage output, SOFCs are operated in series or in form of a stack, in which interconnects connect the cathodes and anodes of the adjacent cells electrically. Besides, it also separates the air and fuel atmospheres of different units from contacting. Therefore, the requirements of the

interconnect are stringent. To pursuit better performance, the interconnect must fulfill the following criteria [4,11]:

(1) Sufficiently high electrical conductivity and low ohmic losses.

(2) Low permeability for fuel gas and air during cell operation. It is the leakage in interconnects that results in a noticeable decline in the cell efficiency.

(3) The coefficient of thermal expansion (CTE) of the interconnect is supposed to be compatible with those of the other cell components. As the CTE of 8-YSZ electrolyte, around 10.5 x $10^{-6}/^{o}C$, remains constant regardless of temperature and oxygen partial pressure, interconnects should have close CTE value to 8-YSZ electrolyte to minimize the thermal stresses.

(4) The interconnect is exposed to both reducing and oxidizing atmospheres, so it must have excellent physical and chemical stability under different working conditions.

(5) Adequate mechanical strength at high temperature.

(6) Reasonable thermal conductivity, which is beneficial for the internal reforming within SOFC.

(7) Easy to fabricate, and low manufactural cost for the industrial production and wide application of SOFC.

The requirements above for interconnect eliminate all but a few materials from consideration. There are in general two types of materials - ceramics and metallic alloys.

1.2.2 Lanthanum chromites interconnect

In early times, $CoCrO_4$ was used as ceramic interconnect, but soon replaced by

lanthanum chromite ($LaCrO_3$), which is now widely used in high-temperature SOFCs (800-1000^oC). $LaCrO_3$ is a perovskite oxide with a melting point over 2400^oC.[12] But due to the high vapor pressure of chromium species, $LaCrO_3$ has a poor sinterability even at high temperature.[13] Many efforts have been made, and doping is found an effective way to improve its sinterability. An acceptable relative density was reported greater than 94% by doping with calcium and strontium. [14] Dopants can help to reduce the volatility of chromium from the surface during sintering, and also form a transient liquid phase and enhance its densification. Several other approaches have been developed to decrease the sintering temperature of $LaCrO_3$ below 1600^oC, including synthesis of highly reactive $LaCrO_3$ by sol-gel method, controlling sintering atmospheres, employing non-stoichiometric compositions, sintering with Cr_2O_3 plates in sandwich configuration, etc. [15-20]

To increase the output power, the internal resistance of the cell should be decreased. Undoped $LaCrO_3$ is a p-type conductor, and its electrical conductivity is quite low, about 0.6-1.0 S/cm at 1000^oC in air. [5,21,22] Studies have shown its conductivity can be improved by doping with alkaline-earth elements (AE) on lanthanum site or transition metals (TM) on chromium sites. [2,5,25] In air atmosphere, for doped $LaCrO_3$ charge neutrality is maintained by $Cr^{3+} \rightarrow Cr^{4+}$ transition and release of an electron. These released electrons are in semi-bound state and easy to be stimulated, which cause a considerable increase in the electrical conductivity. The charge neutrality can be described as[2]:

$$\left[M'_{La}\right] \text{or} \left[N'_{Cr}\right] = \left[Cr^{\bullet}_{Cr}\right] \qquad (1.4)$$

where, [ ] indicates the concentration,

M is the AE cation, and N is the TM cation.

Its electrical conductivity also shows dependence on temperature, dopant content and oxygen partial pressure.[23-26] Jiang et al investigated the electrical conductivity of different cations doped $LaCrO_3$ in air and 10% H_2/N_2 atmospheres, respectively.[25] It is shown in Fig. 1.3 that doping with calcium, strontium, or barium can increase the conductivity of $LaCrO_3$, and conductivities of doped and undoped $LaCrO_3$ in air were higher than that in 10% H_2/N_2 atmosphere. According to Equation 1.4, the concentration of Cr^{4+} increases with the dopant content, and then conductivity is improved. Under the reducing atmosphere (anode side), the conductivity decrease a lot due to the existence of oxygen vacancies from ionic compensation mechanism, which can be described by:

$$\left[M'_{La}\right] \text{or} \left[N'_{Cr}\right] = \left[Cr^{\bullet}_{Cr}\right] + 2\left[V^{\bullet\bullet}_{O}\right] \qquad (1.5)$$

where, $V_o^{\cdot\cdot}$ is the oxygen vacancy.

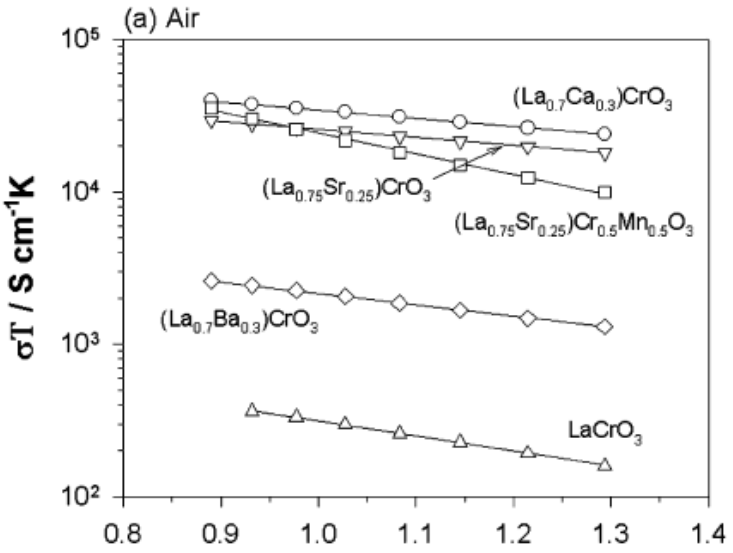

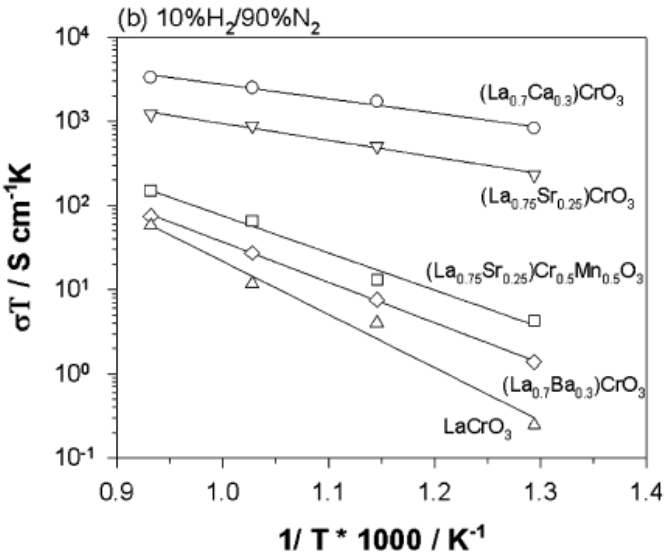

Fig. 1.3 Electrical conductivity for undoped $LaCrO_3$, doped $LaCrO_3$, and $(La_{0.73}Sr_{0.25})(Cr_{0.5}Mn_{0.5})O_3$ perovskite in (a) air and (b) 10% H_2/N_2. Adapted from S. Jiang et al 2008, [25] Courtesy Elsevier.

The interconnects tend to distort due to isothermal expansion in the reducing and oxidizing environment on both sides. Then thermal stresses could be generated, and may lead to a crack if the thermal expansion behavior between interconnect and other components are not matched. The CTE of undoped $LaCrO_3$ is around $8.6\times10^{-6}/^{o}C$ from room temperature to 1000 ^{o}C, which is lower than that of 8-YSZ electrolyte. [27] Doping is also effective to adjust its CTE with calcium, strontium, magnesium. [27-30] Strontium doping is efficient to increase the CTE. Mori et al also studied the thermal expansion behavior of Cr-site doped $La_{0.9}Sr_{0.1}CrO_3$. [27] Their results summarized in Table 1.1 showed doping with Co can increase the CTE of $La_{0.9}Sr_{0.1}CrO_3$ close to that of 8-YSZ electrolyte in air. Similar to conductivity behavior, the thermal expansion of $LaCrO_3$ also depends on oxygen partial pressure. This is related to the increase in oxygen vacancies concentration under the reducing atmosphere. At

the same oxygen partial pressure, higher dopant content can generate more oxygen vacancies, and thus higher thermal expansion. [2,26]

Table 1.1 CTEs of $La_{0.9}Sr_{0.1}Cr_{1-x}M_xO_3$ (M= Mg, Al, Sc, Ti, Mn, Fe, Co, Ni, 0<x<0.10) perovskites at 50-1000 ^oC in air or H_2 atmosphere. Adapted from M. Mori, Y. Hiei, and T. Yamamoto 2008, [27] Courtesy John Wiley and Sons.

Sample	CTE ($\times10^{-6}/^oC$)		
	In air	In H_2	
		1st	2nd
8-YSZ	10.3	10.3	10.3
$LaCrO_3$	8.6	8.6	8.6
$La_{0.9}Sr_{0.1}CrO_3$	9.5	10.5	10.6
$La_{0.9}Sr_{0.1}Cr_{0.95}Mg_{0.05}O_3$	9.2	10.3	10.1
$La_{0.9}Sr_{0.1}Cr_{0.95}Al_{0.05}O_3$	9.7	10.8	10.3
$La_{0.9}Sr_{0.1}Cr_{0.95}Ti_{0.05}O_3$	9.0	9.3	9.2
$La_{0.9}Sr_{0.1}Cr_{0.95}Mn_{0.05}O_3$	10.2	11.2	10.9
$La_{0.9}Sr_{0.1}Cr_{0.95}Fe_{0.05}O_3$	9.5	10.2	10.1
$La_{0.9}Sr_{0.1}Cr_{0.95}Co_{0.05}O_3$	10.4	11.5	10.9
$La_{0.9}Sr_{0.1}Cr_{0.95}Ni_{0.05}O_3$	9.4	10.1	9.7

Although the properties of $LaCrO_3$ have been much improved through cation doping, it still faces some challenges. With sintering aids, it still needs high temperature above 1400^oC

to achieve high relative density. Lanthanum and its rare-earth element dopants also are expensive. As a ceramic material, processing is difficult for $LaCrO_3$, which limits the geometry design of interconnect. So significant efforts have been made to find alternative interconnect materials.

1.2.3 Metallic alloy interconnect

The SOFC technology has been developed toward lower operation temperature in the range of 500^{o}C - 800^{o}C, but their power density and performance still remain at the same level as high-temperature SOFCs. This progress is realized by decreasing the thickness of 8-YSZ electrolyte for lower ohimc polarization in anode-supported SOFC or using new electrolyte materials like doped CeO_2 and $LaGaO_3$ with higher ionic conductivity.[31-35] The reduced working temperature also brings wider materials choice for the interconnect, and therefore metallic alloys seem to be good candidates. Compared with $LaCrO_3$-based ceramic counterparts, their fabrication is much easier for the production of large components and raw materials are inexpensive, both of which decrease the manufacturing cost. Besides, metallic alloys have higher electrical conductivity, and their excellent thermal conductivity can promote internal endothermal fuel reforming. Their ductility enables metallic alloys more durable and reliable from environmental attack under the dual atmospheres. Their thermal-grown oxide scale on the surface in the cathode side can provide sufficient oxidation resistance as long as 40 000 h for the service lifetime of SOFC.[2] In addition, the interconnect provides mechanical support for other ceramic components and gas channel, and metallic alloys possess superior strength to $LaCrO_3$-based ceramics.

The metallic alloys also have some challenges, e.g. the oxidation when simultaneous exposure to both air and fuel atmospheres during high temperature. [36-38] According to Wagner's oxidation theory, the growth of oxidation scale is related to the transport of oxygen ions or chromium cations through the scale by lattice diffusion.[39,40] The growth of the oxide scale obeys the parabolic law:

$$\xi^2 = k_p t = \frac{k_g}{(\chi\rho)^2} t = \frac{t}{d^2} k_g^0 e^{-E_{ox}/KT} \qquad (1.6)$$

where, ξ is the oxide scale thickness at time t and t=0;

k_p and k_g are the rate constants in thickness and weight, respectively;

χ is the weight fraction of oxygen in the oxide (e.g. for Cr_2O_3, $\chi = 0.316$);

ρ is the oxide density (e.g. Cr_2O_3, $\rho = 5.225$ g/cm^3);

and E_{ox} is the activation energy for the oxide scale growth.

The parabolic law can be applied to the thick and homogeneous oxide scale. The parabolic rate constant k_g is an important parameter to measure the oxidation resistance property of alloys. The candidate metallic interconnect materials should have a low k_p.

High-temperature oxidation-resistant alloys (namely, superalloys) are often considered as the choice for interconnect materials.[37,41] Alumina forming alloys have good oxidation resistance during high temperature, because their active element Al is easy to oxidize at the alloy surface and form Al_2O_3 layer to prevent further oxidation.[42,43] But Al_2O_3 is insulating, so alumina forming alloy is not as good as chromia forming alloy in terms of electrical conduction, whose oxidation scale Cr_2O_3 is a p-type semiconductor and has a higher conductivity, about 0.01 S/cm at 800^{o}C in air. [44-48] Different kinds of chromia forming alloys for SOFC interconnect application can be represented in a Fe-Cr-Ni phase diagram illustrated

in Fig. 1.4. [49] Their details are introduced in the following part.

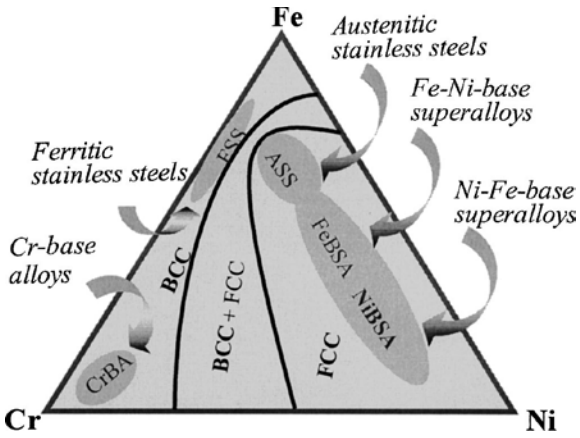

Fig. 1.4 Schematic of alloy design for SOFC applications. Adapted from Z. Yang et al 2003, [49]

Courtesy The Electrochemical Society.

1.2.3.1 Chromium-based alloys

Chromium metal has been considered as an alloy base since the late 1940s due to its high melting point (1863^{o}C), good oxidation resistance, lower density and higher thermal conductivity than most superalloys.[49,50] Unalloyed chromium has quite low strength, about 70 MPa at 1200°C under compression tests. [51] To reduce their embrittlement and increase mechanical strength at high temperature, trace mount of reactive elements like Y, La, Ce, etc are added as elements or oxides to form the oxide dispersion strengthened (ODS) alloys. [41,52,53] Strengthening is realized by increasing its ductile-to-brittle transition temperature (DBTT) or the alloy density. Their oxidation resistance to the thermal cycling is also increased by dispersion of the rare-earth oxides, because these oxides effectively improve the adherence of the scale to the metallic matrix and reduce the oxidation rate.[54] A good example is Plansee Ducrolloy with a composition of 94 wt% Cr, 5 wt% Fe and 1 wt% Y_2O_3 (Cr-5Fe-1Y_2O_3). Larring et al studied its high-temperature corrosion under different water

vapor pressure. [55] The rates of both Cr_2O_3 formation and its evaporation was found to decrease after dip-coating in $Ce(NO_3)_3$ solution and heating in H_2/Ar atmosphere at 900^oC for 3 h (Ce-treatment on the alloy surface). CeO_2 have high oxygen ion conductivity, and if it segregated on the surface, the reason why the rate of Cr_2O_3 evaporation was reduced could be ascribed to the Cr_2O_3-free surface area. Chromium based alloys is body centered cubic (BCC) structure. Besides lower electrical resistance, their another advantage is their thermal expansion is close to that of 8-YSZ electrolyte. Quadakkers et al made a comparison of thermal expansion behavior between chromium based alloys and stainless steels, and stainless steels showed larger thermal expansion than Cr-0.4La_2O_3 and Cr-5Fe-1Y_2O_3. [56] The CTE value of Cr-5Fe-1Y_2O_3 is 11.8 x $10^{-6}/^oC$ from room temperature to 1000^oC.

Although ODS chromium based alloys possess excellent oxidation resistance, mechanical properties and compatible CTE, their fabrication is still difficult and costly especially compared with other commercial metallic alloys. In addition, some problems are inevitable. Their higher chromium concentration can lead to excessive Cr_2O_3 scale growth, and volatile chromium species cause cathode poisoning [56], which will be discussed in detail later. Therefore, increasing efforts have been focused on other Cr forming alloys.

1.2.3.2 Ni-Cr-based alloys

Ni-Cr-based alloys have a face centered cubic (FCC) structure. Compared with ferric stainless steels, they exhibit lower scale growth rate and much higher mechanical strength.[57] The chromium content is required to be around 15% in Ni-Cr-based alloys to form a continuous chromia layer, lower than that of Fe-Cr based alloys, which is a optimum content

of 18-19%.[38] England et al reported the oxidation kinetics of different Ni-based alloys in air and humidified hydrogen. [58,59] Their major composition in the oxidation scale is Cr_2O_3, and $(Mn,Cr)_3O_4$ was detected as a second phase. Their oxidation behavior obeys the parabolic law. Haynes 230 with the highest Cr content showed the slowest oxidation rates in air, corresponding with lowest ASR. However, the oxidation kinetics of these Ni-based alloys at 800^{o}C in wet hydrogen was faster than that in air. The ASR of the oxidation layer grown in wet hydrogen was also higher in comparison with that in air. Yang et al studied the oxidation behavior of different Ni-Cr-based alloys with different chromium content in air, hydrogen and moist air-moist hydrogen dual atmospheres. [60] A thin layer of Cr_2O_3 and $(Mn,Cr,Ni)_3O_4$ spinels formed in air on Haynes 230 and Hastelloy with a relative high Cr content (22 wt% and 16 wt%, respectively). However, a thicker double layer more than 5 μm with NiO scale on top of a chromia-rich substrate was observed in Haynes 242 with only 8 wt% Cr in the moist air and at the air side of dual-atmosphere conditions. A similar thin layer formed on the three alloys after oxidation in moist hydrogen, indicating high oxidation resistance. The layer's composition are Cr_2O_3 and $(Mn,Cr,Ni)_3O_4$ spinels for Haynes 230 and Hastelloy S, and Cr_2O_3 for Haynes 242. NiO did not appear due to its thermodynamical instability in the reducing condition. At dual atmosphere hydrogen flux from the fuel side to the air side is likely to alleviate NiO growth and make the interface between the scale and metal dense. The FCC Ni–Cr-base alloys usually demonstrate a higher CTE than the BCC ferritic stainless steels, which typically have a CTE of 12 - 13 x10^{-6}/^{o}C. [49] Haynes 230 and Hastelloy S showed a higher CTE value about 15 x10^{-6}/^{o}C from room temperature to 800°C. Lowest CTE was obtained in Haynes 242, 13.1 x10^{-6}/^{o}C, which is ascribed to heavy additions of Mo, and

the limited amount of Cr. Haynes 242 is the recently developed Ni-Cr-based alloy. It can be used as gas turbine components, because it has high mechanical strength and lower CTE than other Ni-based alloy like Haynes 230.[61] Its thermal exapnsion is more compatible with other SOFC components. Geng et al also investigated Haynes 242 alloy in different environments.[62, 63] Consistent with Yang et al's work, a NiO scale was observed on the top of Cr_2O_3 and $(Mn,Cr)_3O_4$ scale in the air oxidation too. The NiO scale did not continuously distributed on the alloy surface, however there is no apparent scale spallation. Its mass gain after isothermal oxidation at 800 °C for 500 h in air was less than that of Crofer, and its ASR of the oxide scale was lower that that of Ebrite and Crofer. Haynes 242 showed a quite different behavior in Ar + 4 vol% H_2 + 3vol% H_2O atmosphere. The oxidation layer consisted of a top thin $(Mn,Cr)_3O_4$ spinel scale and an inner Cr_2O_3 scale. The calculated activation energy of oxidation was near that of chromium self-diffusion in Cr_2O_3, which suggested the chromia layer is formed by the outward diffusion of chromium.

Ni–Cr-base alloys have shown excellent oxidation resistance and sufficient strength for SOFC interconnect. Its significant challenge is the CTE mismatch to other components. To take advantages of it potential, new designs are required for interconnects and stacks. The identification to optimize alloy compositions is also a good solution.[64]

1.2.3.3 Fe-Cr-based alloys

Fe-Cr-based alloys include a large number of alloys, and they are also termed as stainless steel (SS). Compared with Cr-based alloys and Ni-Cr-based alloys, they are more promising due to their easy fabrication, reasonable thermal expansion and low maunfactural

cost. Stainless steels are often divided into four groups based on their crystal structure: (1) ferritic stainless steels (FSS); (2) austenitic stainless steels (ASS); (3) martensitic stainless steels; and (4) precipitation hardening steels.[49] Among them, the ferritic stainless steels are the most attractive due to their BCC structure which enable them to have more matched CTE (11.5-14 $x10^{-6}/^{o}C$ from room temperature to $800^{o}C$) with other SOFC components. Besides, they also have good oxidation resistance and low fabrication cost.

In order to develop a continuous Cr_2O_3 scale, enough chromium content is required in the substrate alloy. According to the Fe-Cr phase diagram, at least 13 wt% Cr should be contained to stabilize their ferritic structure phase.[65] In the commercial stainless steels, the Cr content is usually in the range of 11- 30 wt%.[49] High-Cr ferritic alloys with Cr concentration over 16 wt% showed good oxidation resistances.[66,67] The minimum chromium content to form a homogenous dense Cr_2O_3 scale is also affected by the oxidation environments. Othman et al's work showed water vapor and high temperature (700 ^{o}C - $950^{o}C$) both can accelerate isothermal scaling rates, and increaser the chromium level.[68] The elements like C and N which lead to form austenite must be controlled in a low content. The impurities e.g. Si and S should be eliminated, because Si can easily produce continuous insulating layers at the interface, and trace amounts of S can cause spallation of oxide scale. [69]

E-Brite is a highly pure ferritic stainless steel which was developed by Allegheny Ludlum Steel Corporation for SOFC. Its typical compositions are: Fe (balance), Cr (27.5 wt% max), Ni+Cu (0.5wt% max), Mn(0.4 wt% max), Si (0.4 wt% max), Mo (1.5 wt% max), N (0.0015 wt% max), and C (0.01 wt% max).[70] Huang et al studied its oxidation kinetics in

stagnant air. [37] Its scale contained primary Cr_2O_3, and its growth rate showed a parabolic dependence on time. Its CTE was 11.8 $x10^{-6}/^oC$ from room temperature to 500^oC, quite close to other cell materials. However, its ASR with oxide electrodes was also near the limit for SOFC. A similar results was also observed in Geng et al's work.[71] The weight gain of Ebrite was the smallest among the ferritic alloys they studied, which was related to the dense Cr_2O_3 to prevent further oxidation. Besides, no oxide scale spallation was detected after the cyclic oxidation test.

Crofer 22 APU is another widely-used high-temperature ferritic stainless steel for SOFC interterconnect, which was developed by Thyssenkrupp Steel AG. Its chemical compositions are: Fe (balance), Cr (24 wt% max), Mn (0.80 wt% max), Si (0.50 wt% max), Cu (0.5wt% max), Al (0.5 wt% max), S (0.0020 wt% max), P (0.050 wt% max), Ti (0.020 wt% max), and C (0.03 wt% max).[72] This alloy contains high concentration of Mn, and its protective oxide scale consist of Cr_2O_3 and $(Cr,Mn)_3O_4$ spinel, which is different from E-brite. The diffusion rate of different alloy elements in Cr_2O_3 follows the increasing rank of Cr, Ni, Co, Fe, Mn. [73] So during oxidation, the rapid outward diffusion of Mn lead to the raction with Cr and oxygen and formation of a Mn-containing spinel layer on top of the continuous Cr_2O_3 matrix. Liu also reported MnO was observed with Mn-Cr spinel on the surface of Crofer 22 APU after oxidation at 900 °C for 1000 h in the reducing atmosphere of Ar + 5 vol.% H_2 + 3 vol.% H_2O. [74] Fontana et al compared oxidation resistance of Crofer 22 APU with Fe30Cr (30 wt% Cr but no Mn). [75] Fe30Cr (k_p= 3.14 $x10^{-13}g^2/cm^4s$ in air, and 1.54 $x10^{-12}g^2/cm^4s$ in H_2/10%H_2O) showed higher mass gain than Crofer 22 APU (k_p = 2.5 $x10^{-14}g^2/cm^4s$ in air, and 3 $x10^{-14}g^2/cm^4s$ in H_2/10%H_2O) after heating at 800^oC for 100 h.

Crofer 22 APU also possessed low rate of chromium vaporization. Konysheva et al evaluated the chromium release of Crofer 22APU and ODS Cr-5Fe-1Y_2O_3 alloy.[76] A $(Cr,Mn)_3O_4$ spinel scale with a thickness of 0.5 micrometer effectively decreased the Cr evaporation rate of Crofer 22 APU by a factor of 3 compared with alloy only forming Cr_2O_3 scale at 800^oC in humidified air for a time up to 1300 h. They also found change in the minor additives like Al and Si in Crofer 22 APU can influence the oxide scale thickness, morphology and the $(Cr,Mn)_3O_4/Cr_2O_3$ ratio. Yang et al evaluated oxidation behavior and the conductivity of Crofer 22 APU and other ferritic Fe-Cr-Mn steels.[66] A chromia-rich scale beneath $(Mn,Cr)_3O_4$ spinel rich layer was formed both in air and moist hydrogen (97%H_2/3%H_2O) at 800 ^oC for 1200 h. Its ASR was only 13.0 mΩcm^2 after 1800 h at 800 ^oC, much lower than that of other ferritic steels like E-Brite and AISI-SAE 446. The low value is ascribed to higher electrical conductivity of the $(Mn,Cr)_3O_4$ spinel phases than Cr_2O_3.[77] Overall, Crofer 22 APU appears to be one of the most promising candidate for SOFC interconnect alloys.

It should be noted that the presence of reactive elements could affect the oxidation behavior of alloy. AISI-SAE 430 is a commercial ferritic grade without reactive elements. AISI-SAE 441 alloy is based on AISI-SAE 430's composition, but with the addition of reactive elements Ti and Nb. Rufner et al' work showed their oxidation behavior at the dual atmosphere is quite different.[78] A porous Fe_2O_3-rich surface layer was formed on the surface of AISI 441 at the air side, while AISI 430 had isolated Fe-rich surface nodules. This may be partly related to Nb promoting the hydrogen transport in 441 by segregating at grain boundaries as a short-cut pathway. Then hydrogen would react with the oxide layer to enhance the iron outward diffusion from its substrate. A study by Shaigan et al compared the

metal-oxide scale performance between ZMG 232 and AISI-SAE 430. [79] ZMG 232 is Fe-22% Cr based alloy with small amounts of reactive elements like Zr and La, developed by Hitachi Metals especially for SOFC interconnect. [80,81] Both of them were oxidized at 800^{o}C in static air for various periods. Scale spallation was observed in AISI-SAE 430 just after oxidation less than 100 h, while it did not appear in ZMG 232 ever after longer hours. This is attributed to the segregation of impurity elements like Si, S, Cl and so on at the interface between alloy and oxide scale in AISI-SAE 430, and therefore the scale adhesion and its contact area with alloy is reduced. However, the reactive elements Zr and La effectively prevent the segregation of impurity elements in ZMG 232. The reactive elements can suppress the oxide growth rate and impurities of segregation by influencing the diffusion of chromium and oxygen. [82-85] The reactive element oxide segregate at the interface between scale and substrate, and inhibit voids formation. A dynamic-segregation model of the reactive element outward diffusion during high temperature oxidation is illustrated in Fig. 1.5.[69]

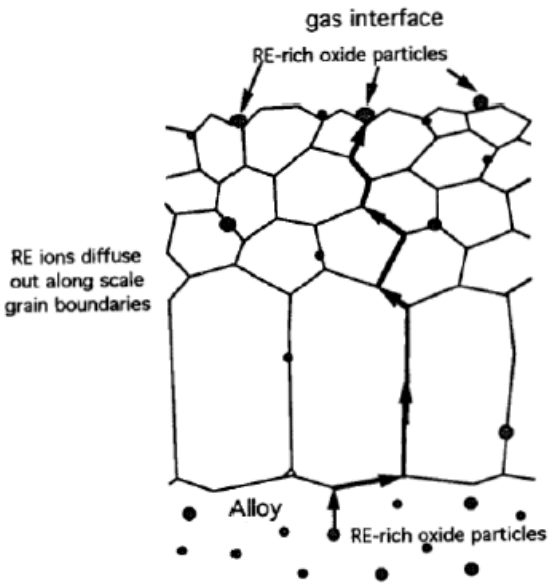

Fig. 1.5 A dynamic-segregation model of the reactive element function during high

temperature oxidation. Adapted from B. A. Pint 1995, [69] Courtesy Springer.

A comparison between different chromia forming alloys is listed in Table 1.2. [49] Ferritic stainless steel is considered as the most attractive candidate in terms of its good oxidation resistance, compatible thermal expansion with 8-YSZ electrolyte, and the low cost.

Table 1.2 Properties of different chromia forming alloys for SOFC interconnect. Adapted from Z. Yang et al 2003, [49] Courtesy The Electrochemical Society.

Alloys	Matrix Structure	CTE $x10^{-6}/^{o}C$ (RT-800^{o}C)	Oxidation Resistance	Mechanical Strengths	Manufacturability	Cost
Cr base alloys	BCC	11.0-12.5	Good	High	Difficult	Very Expensive
Ferritic stainless steels	BCC	11.5-14	Good	Low	Fairly Readily	Less Expensive
Austenitic stainless steels	FCC	18-20	Good	Fairly High	Readily	Less Expensive
Fe-Ni-Cr base alloys	FCC	15-20	Good	High	Readily	Fairly Expensive
Ni(-Fe)-Cr base alloys	FCC	14-19	Good	High	Readily	Expensive

In addition, some low-Cr Fe based alloys are also studied. A Fe-Co-Ni based steel with only 6wt% Cr was evaluated by Geng et al.[86] After oxidation at 800 °C in air for 12 weeks, a Cr-free $(Fe,Co,Ni)_3O_4$ spinel layer formed atop Cr_2O_3 scale, which effectively blocked Cr violation, decreased the scale growth rate and ASR. The low-Cr alloy also showed good scale adherence and compatibility with the $La_{0.8}Sr_{0.2}MnO_3$ cathode material.

1.2.4 Problems with metallic interconnect materials

Although ferritic stainless steels are the promising metallic interconnects material, they still face some challenges at SOFC operation condition, like high growth rate of oxide scale, evaporation of Cr species, etc.

1.2.4.1 Oxidation problem

The thermally grown Cr_2O_3 scale is inevitable during oxidation for all chromium forming alloys. For Fe-Cr-Mn stainless steels, their oxidation layer also contain $(Mn,Cr)_3O_4$ spinel. The electrical conductivity of both Cr_2O_3 and $(Mn,Cr)_3O_4$ is much lower than that of alloy matrix. Intensive studies have shown the thickness of Cr_2O_3 scale on stainless steels can reach several micrometers or even tens of micrometers after oxidation for thousands of hours under SOFC working environment. The existence of water vapor can also promote the growth of Cr_2O_3 scale at high temperature.[68,87,88] Even there is no crack, as the scale grows further, the overall ASR will increase. In practical, attributed to the thermal stress between scale and alloy substrate, crack or spallation will take place, and results in the degradation of SOFC stack. Therefore, an improvement to alleviate oxidation of metallic alloys is required.

1.2.4.2 Chromium poisoning

Another inherent weakness of chromium forming alloys is Cr poisoning of electrodes, which can cause severe degradation in SOFC electrochemical performance. The negative effect of chromium on lanthanum strontium manganite (LSM) cathode poisoning has been confirmed by different groups when applying chromium forming alloys.[89-93] In the cathode side, the Cr_2O_3 layer on the surface of metallic alloy reacts with water and oxygen molecules, and generates volatile $CrO_2(OH)_2$ and/or CrO_3 with Cr in the oxidation state of +6. The reactions can be expressed by the following equations[94-96]:

$$2Cr_2O_3(s) + 3O_2(g) \leftrightarrow 4CrO_3(g) \quad (1.6)$$

$$2Cr_2O_3(s) + 3O_2(g) + 4H_2O(g) \leftrightarrow 4CrO_2(OH)_2(g) \quad (1.7)$$

Then the volatile Cr species migrate through the cathode, and segregate at the three-phase boundary (TPB, cathode, electrolyte and oxygen) as Cr_2O_3. The reduction of $CrO_2(OH)_2$ to solid Cr_2O_3 can dramatically deteriorate the cathode electrochemical activity, described by Equation 1.9 and 1.10.

$$2CrO_3(g) + 6e^- = Cr_2O_3(s) + 2H_2O(g) + 3O^{2-} \quad (1.8)$$

$$2CrO_2(OH)_2(g) + 6e^- = Cr_2O_3(s) + 3O^{2-} \quad (1.9)$$

Yokokawa et al also analyzed the reactions of cathode with chromium vapors in thermodynamics, and found the Cr_2O_3 deposition or $CrMn_2O_4$ formation at the cathode/electrolyte interface is the direct reason for the chromium poisoning which results in slow oxygen ion diffusivity in LSM cathode. [97]

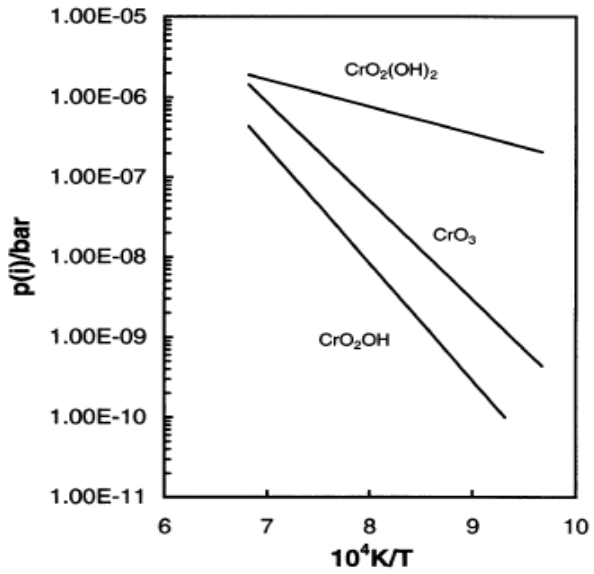

Fig. 1.6 Vapor pressures of different volatile chromium species as a function of temperature.

Adapted from W. Z. Zhu, and S.C. Deevi 2003, [2] Courtesy Elsevier.

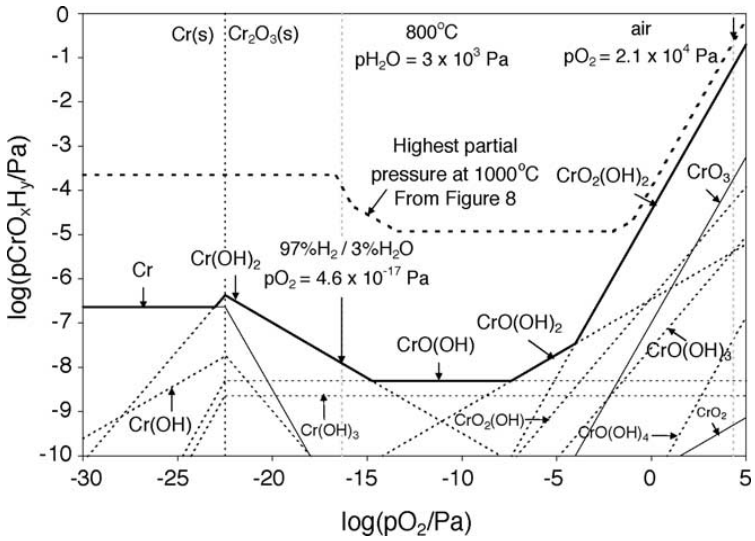

Fig. 1.7 Equilibrium vapor pressures of chromium–oxygen–hydrogen gas species at 800 ^{o}C with a water vapor pressure of 3 kPa as a function of oxygen partial pressure. Adapted from J. Fergus 2005, [54] Courtesy Elsevier.

The vapor pressures of different volatile chromium species as a function of temperature is displayed in Fig. 1.6. [2] It is obvious that $CrO_2(OH)_2$ possesses the highest vapor pressure

in the IT-SOFC working temperature range of 600-800 ^{o}C among all Cr species. Fig. 1.7 shows the equilibrium vapor pressures for Cr-O-H species at 800^{o}C with a water vapor pressure of 3 kPa as a function of oxygen partial pressure.[54] Their equilibrium vapor pressure increases with oxygen partial pressure. So chromium poisoning favors to happen in the cathode side. Currently increasing studies has been focused on novel cathode materials with higher catalysis activity to resist chromium poisoning.[98-104]

Chromium forming alloy is difficult to achieve satisfactory performance when using directly without any surface modification. To suppress its excessive Cr_2O_3 scale growth and chromium violation to cathode, many efforts have been made such as alloy composition optimization, surface treatment, etc. Among them, applying protective ceramic coating on the alloy surface is an effective method.

1.3 Interconnect coating materials for SOFC

The coating material is applied between alloy interconnect and cathode. It servers as a barrier to chromium outward diffusion and oxygen inward diffusion, and therefore decreases the oxidation rate of metallic interconnect and chromium evaporation rate. To fulfill its function, it should satisfy the following requirements:

(1) Dense and low diffusion rate of chromium and oxygen to hinder their migration in the coating;

(2) Matched thermal expansion with substrate and cathode material to avoid internal stress and local spallation after thermal cycling;

(3) High electrical conductivity to decrease the cell resistance;

(4) Non- volatile and chemical stability with the alloy interconnect, cathode, and contact layer at high temperature.

Various coatings have been developed to protect metallic interconnects, and they can be categorized mainly into three kinds: reactive element oxide, perovskite oxide, and spinel oxide coatings.[43]

1.3.1 Reactive elements coating

As discussed in the above section, the addition of reactive elements or its oxides in Cr-forming alloys to form dispersed phase effective improved the adherence of the oxide scale to the substrate and reduce the oxidation rate by changing the diffusion mechanisms of chromium and oxygen. They can also be used as protective coating on the alloy surface, and the often used coating elements are Y, La, Nd and Ce.[105-107] Fontana et al studied three coatings including La_2O_3, Nd_2O_3 and Y_2O_3 on different metallic alloys (Crofer 22 APU, AL 453 and Haynes 230) applied by metal organic chemical vapour deposition (MOCVD).[108] The oxidation behavior was compared between coated and uncoated alloys after aging at 800^{o}C for 100 h in air. The Cr_2O_3 scale thickness of Crofer 22 APU was reduced by a factor of 1.5 after applying coating. La_2O_3 was acted as barrier that limits the chromium diffusion during oxidation. It reacted with chromia and formed $LaCrO_3$ perovskite. Similarly, Nd_2O_3 was concentrated at the chromia scale/top spinel grains interface as $NdCrO_3$ perovskite. However, Y_2O_3 has high oxygen permeability. The chromia scale formed between Y_2O_3 coating and alloy, and the generated stresses cause cracks in all Y_2O_3 coated samples. In their another study of Crofer 22 APU under H_2/10%H_2O atmosphere, Y_2O_3 coating also has a

different oxidation behavior with other coatings.[74] It did not react with chromia to form $YCrO_3$ perovskite. The weight gain of Y_2O_3 coated Crofer 22 APU was higher than that of the other two coated samples. Kim et al compared thin coatings of Y, Co and Y/Co in the oxidation behavior of ferritic stainless steel AISI 444 in wet air up to 1000 h at 800 ^oC. [109] Y(30 nm), Co(50 nm) and Y(30 nm)/Co (50 nm) coatings were applied using electron beam evaporation method. The scale growth was reduced after coating with Y and Y/Co. The average scale thicknesses of the uncoated, Y-coated, and Y/Co-coated samples were 1.9 μm, 0.9 μm, and 1.1 μm. An $YCrO_4$ layer was formed between $MnCrO_4$ region and Cr_2O_3 scale, which was responsible for the suppressing of Cr_2O_3 sub-layer growth. Y_2O_3 coated sample showed the lowest and stable ASR value. Reactive element oxide coatings increase the oxidation resistance of stainless steels and the adhesion of oxide scale, however, their coating layers are usually porous and quite thin which makes them not effective as barriers to chromium outward diffusion compared to other types of coatings.[110]

1.3.2 Perovskite coating

Perovskite oxides are widely used as cathode and interconnect of SOFC, due to their higher electrical conductivity and compatible thermal expansion. The formula of perovskites is expressed as ABO_3, where A is rare earth cation (e.g. La, Pr, Ce, etc), and B is transition metal cation (e.g. Cr, Co, Mn, Fe, Cu, V, etc). [43] They are also applied as conductive coatings on alloy interconnect. The advantages of perovskite coating include their rare earth elements can retard the oxidation. Besides, as discussed in $La_{1-x}Sr_xCrO_3$ interconnect, the conductivity of perovskites can be improved by A-site or B-site doping.

Lu et al deposited a dense $LaCrO_3$-based coating on AISI 444 stainless steel by sol–gel process.[111] A smooth and uniform coating can be formed after annealing at 800^{o}C for 1 h in air. The ASR of the coated AISI 444 is much lower than that of uncoated sample after oxidation at 850 ^{o}C for 100 h. Uncoated AISI 444 showed notable weigh loss due to the several spallation of the scale, while the sol–gel coatings provided the protection during the cyclic oxidation and improved scale adhesion. Shaigan et al also developed the Co/$LaCrO_3$ coating on AISI 430 by electrodeposition.[112] After thermal exposure at 800^{o}C in air up to 2040 h, the Co/$LaCrO_3$-coated AISI 430 has a triple-layer scale including a Cr_2O_3 inner layer, $(Co,Fe)_3O_4$ mid-layer and Co_3O_4 outer layer. Compared with bare AISI 430, the Co/$LaCrO_3$-coated AISI 430 had a lower ASR, not exceed 0.02 Ω cm^2 after 900 h at 800 °C in air, which could be attributed to high conductivity of $LaCrO_3$ perovskite and the Co containing spinel scale.

The high temperature SOFC cathode $LaMnO_3$ is also investigated as coating material of interconnect. Shong et al deposited $La_{0.8}Sr_{0.2}MnO_3$ on Crofer 22 APU using spin coating method, and both the coated and uncoated samples were oxidized in ambient air at 800 °C up to 1600 h.[113] All samples had $(Mn,Cr)_3O_4$ spinel phase in the scale, but the Mn/Cr ratio of the coated sample was higher, in which $La_{0.8}Sr_{0.2}MnO_3$ coating promotes the growth of $(Mn,Cr)_3O_4$ spinel and increases its Mn content. The ASR of coated Crofer 22 APU was reduced to almost one third of that of uncoated sample, which could be attributed to the higher Mn content in $(Mn,Cr)_3O_4$ spinel phase. Another work focused on the $LaMn_{0.9}Ti_{0.1}O_3$ coating, which was applied on the surface of Haynes 230 by radio-frequency (RF) sputtering.[114] Ti was doped in Mn site to suppress the oxygen ion transport. After oxidation

at 800 ^{o}C in air for 1080 h, the thickness of oxide scale of uncoated Haynes 230 was around 2.2 μm, while it was only 0.63 μm in $LaMn_{0.9}Ti_{0.1}O_3$-coated samples. Its ASR was also reduced after coating.

$La_{1-x}Sr_xCoO_3$, $La_{1-x}Sr_xMnO_3$ and $La_{1-x}Sr_xFeO_3$ have much high electrical conductivity than $La_{1-x}Sr_xCrO_3$, but these three are mixed electrical and ion conductor which means they can promote the oxygen ion diffusion at the same time. Yang et al compared $La_{0.8}Sr_{0.2}FeO_3$ and $La_{0.8}Sr_{0.2}CrO_3$ coating on different ferritic stainless steels (E-brite, Crofer 22 APU, and AL453).[115] Both of the pervoskites coatings reduced the oxidation rate of Crofer 22 APU after oxidation at 800 ^{o}C in air up to 1200 h, however, $La_{0.8}Sr_{0.2}CrO_3$ coating (k_g= 3.2 x10^{-14} $g^2cm^{-4}s^{-1}$) was more effective than $La_{0.8}Sr_{0.2}FeO_3$ (k_g= 6.2 x10^{-14} $g^2cm^{-4}s^{-1}$). The similar results were also obtained in the oxidation of AL453 and E-brite. The ionic conductivity of $La_{0.8}Sr_{0.2}CrO_3$ is 2-3 orders of magnitude lower than that of $La_{0.8}Sr_{0.2}FeO_3$. At the same condition, oxygen ions can diffuse inward more easily through $La_{1-x}Sr_xFeO_3$ coating at high temperatures. In addition, chromium was detected to diffuse into the $La_{0.8}Sr_{0.2}FeO_3$ coating. Their work indicates $La_{0.8}Sr_{0.2}CrO_3$ is superior to $La_{0.8}Sr_{0.2}FeO_3$ coating as barrier to prevent chromium migration. However, one potential problem for $La_{1-x}Sr_xCrO_3$ is that it contains chromium element, and chromium is easy to evaporate at high temperature. Then the released chromium could still diffuse though the coating and cause cathode poisoning.[42,43]

1.3.3 Spinel coating

Recently, the research trend has been focused on spinel oxides as the coating material. Spinel oxides are always attractive due to their excellent electronic and magnetic properties

over a wide range of temperatures. Especially, the spinel oxides with 3d transition metals occupied on the octahedral sites possess the unique physical properties like ferromagnetism, antiferromagnetism, charge ordering, superconductivity, which are depended on the valence of the cations.[116]

The general formula of spinel oxide is AB_2O_4, where O^{2-} ion are in a close packing, and A and B are divalent, trivalent or quadrivalent cations occupying the octahedral and tetrahedral sites, respectively. Its crystal structure is illustrated in Fig. 1.8.[38] Spinel oxides have normal and inverse structures. In a spinel unit cell, there are 32 octahedral sites, and 64 tetrahedral sites. In the normal structure, B^{3+} cations occupy half of the octahedral holes, and A^{2+} cations occupy 1/8 of the tetrahedral holes. A normal spinel case is Co_3O_4 at room temperature, in which Co^{2+} on tetrahedral sites and Co^{3+} on octahedral sites.[118] In the inverse structure, all A^{2+} cations occupy the octahedral sites, and push half of the B^{3+} cations from the octahedral sites to the tetrahedral sites. An ideal case of inverse spinel is Fe_3O_4, which can be expressed crystallographically in $(Fe^{3+})_{tetra}[Fe^{2+}Fe^{3+}]_{oct}O^{2-}{}_4$.[119] However, for most spinel oxides, their cations distributions are between the above two structures.[120]

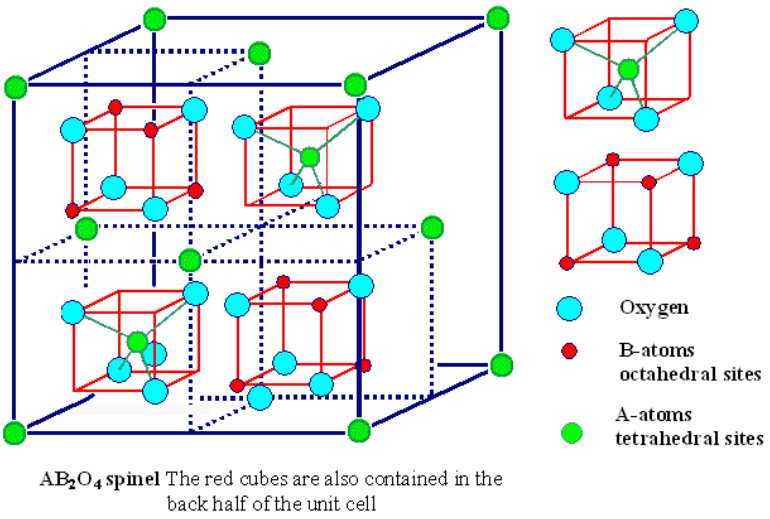

Fig. 1.8 Schematic diagram of crystal structure of AB_2O_4 spinel. Adapted from J. Wu, and X. Liu 2010, [38] Courtesy Elsevier.

The high electrical conductivity and compatible thermal expansion can be obtained by adjusting the A and B cations' composition and their ratio. Spinel coatings have indicated promising performance. Petric's group did an extensive study on the electrical conductivity of spinel oxides, and found $Cu_xMn_{3-x}O_4$ system had much higher conductivity than most other tested spinels.[121,122] The conductivity of $Cu_{1.3}Mn_{1.7}O_4$ can reach up to 225 S/cm at 750°C. They further applied $Cu_{0.4}Mn_{1.6}O_4$ by electroplating technique on stainless steel UNS 430, and the Cu-Mn spinel coating restricted Cr_2O_3 growth at the interface between coating and UNS 430 and still had good adhesion to alloy matrix after cyclic oxidation at 750°C as long as 28 days due to its matched thermal expansion with the substrate. [123-125]

Hua et al developed $NiCo_2O_4$ coating on the surface of SUS 430 by sol-gel process.[126] The oxidation resistance of SUS 430 was significantly improved with $NiCo_2O_4$ coating by limiting the access of oxygen to the cations via outward diffusion during thermal exposure at 800°C for 200 h in air (k_g: 8.3 $x10^{-14}$ $g^2cm^{-4}s^{-1}$ for uncoated sample, and k_g: 8.1 $x10^{-15}$

$g^2cm^{-4}s^{-1}$ for coated sample). A recent work evaluated $CoFe_2O_4$ spinel oxide as a potential coating on Crofer 22 APU by electroplating for cell testing as long as 180 h.[127] The channeled Crofer 22 APU interconnect with $CoFe_2O_4$ coating showed higher cell performance and lower degradation rate (3×10^{-5} Wcm^{-2} h^{-1}) than the bare interconnect (about 3×10^{-4} Wcm^{-2} h^{-1}).

In addition, other spinel oxides were also studied like $NiMn_2O_4$, $NiFe_2O_4$, etc.[128,129] They all exhibit to improve the oxidation resistance and block Cr diffusion effectively. Among these spinel coating, $(Mn,Co)_3O_4$ oxides are the most promising coating candidates due to their reasonable CTE (11.4×10^{-6}/°C for $Mn_{1.5}Co_{1.5}O_4$ and $12\text{-}13\times10^{-6}$/°C for ferritic stainless steel) and high electronic conductivity(60 S/cm for $Mn_{1.5}Co_{1.5}O_4$ at 800°C). [121, 130,131]

As early as 2000, Larring et al first reported $(Mn,Co)_3O_4$ coating was more effective to prevent Cr outward diffusion. [132] Then much more extensive studies have been focused on $(Mn,Co)_3O_4$ system as coating candidate currently. Chen et al applied a dense $MnCo_2O_4$ layer by slurry coating on AISI 430. After oxidation at 800°C for 60 h and 850°C for 120 h, its scale thickness was only sub-micron, and the ASR was significantly reduced by one order of magnitude.[133] Similar results for $MnCo_2O_4$ coating are confirmed by other researchers.[134-136] Yang et al investigated the effect of $Mn_{1.5}Co_{1.5}O_4$ coating by screen printing on E-brite. [130] According to the Mn-Co binary phase diagram, $Mn_{1.5}Co_{1.5}O_4$ is a single cubic phase at 800°C.[137] Besides, its electrical conductivity is much higher than that of Cr_2O_3 and $MnCr_2O_4$. A dense coating was formed by first heat treatment in a reducing atmosphere and then in air. Their result showed the contact resistance between cathode and coated E-brite was as low as

7 mΩcm^2 at early stages, and only slightly increased after 400 h at 800^{o}C. The thickness of Cr_2O_3 scale was just about 1.0 μm, which indicated $Mn_{1.5}Co_{1.5}O_4$ coating can effectively inhibit the Cr_2O_3 growth and prevent chromium outward migration through coating. They also tried $Mn_{1.5}Co_{1.5}O_4$ on Crofer 22 APU. [138] After applying $Mn_{1.5}Co_{1.5}O_4$ coating, the contact ASR between Crofer 22 APU and LSF cathode was reduced from 38.6 mΩcm^2 to 12.8 mΩcm^2 after testing at 800^{o}C for 400 h. A steep Cr decrease was still observed from the subscale/spinel coating interface after a half-a-year test of thermal cycling as shown in Fig. 1.9.[138] The matched CTE between Crofer 22 APU and $Mn_{1.5}Co_{1.5}O_4$ and dense coating structure both give rise to a good long-term stability. Xin et al reported a $Mn_{0.9}Y_{0.1}Co_2O_4$ spinel oxide applied on Crofer 22 APU by slurry coating. [139] With the protection of $Mn_{0.9}Y_{0.1}Co_2O_4$ coating, the ASR was significantly lowered to 4 mΩcm^2 from 17 mΩcm^2 after operation at 800^{o}C for 538 h even including several thermal circles. $MnCo_{1.9}Fe_{0.1}O_4$ is also $(Mn,Co)_3O_4$-based coating. X. Montero et al's study showed it can improve the oxidation resistance of Crofer 22 APU and F18TNb after screen coating. [140] They also compared it with reactive oxide coating (CeO_2, Y_2O_3) and pervoskite oxide coating ($La_{0.8}Sr_{0.2}FeO_3$, and $La_{0.6}Sr_{0.4}FeO_3$). [141] The $MnCo_{1.9}Fe_{0.1}O_4$ coated sample still showed the lowest ASR, and it was more effective to limit the outward migration of chromium cations than the other coatings. The superior performance of $(Mn,Co)_3O_4$-based coating over pervoskite oxide coating was also confirmed in Larring et al's work.[132]

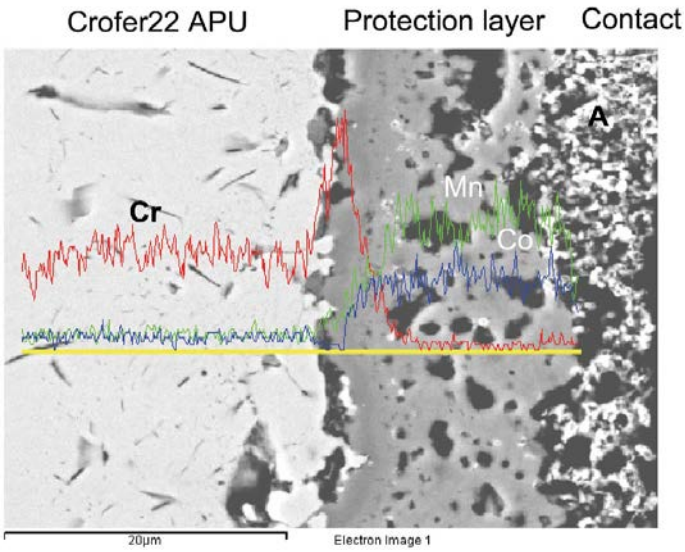

Fig. 1.9 SEM images and EDS analysis on Crofer 22 APU with $Co_{1.5}Mn_{1.5}O_4$ coating after a period of 6 months under thermal cycling. Adapted from Z. Yang et al 2005, [138] Courtesy The Electrochemical Society.

$(Mn,Co)_3O_4$ system have attracted increasing focuses in recent years, and different coating techniques have been developed on them, e.g. electrodeposition of metals, thermal-growth or RF-sputtering, magnetron sputtering, atmospheric plasma spraying (APS), aerosol deposition, etc. [136,142-146] All these work indicate $(Mn,Co)_3O_4$ system are the promising coating candidate for SOFC metallic interconnects. However, more works are still needed to achieve satisfactory performance.

1.4 Objectives of the dissertation

The excellent performances of $(Mn,Co)_3O_4$ spinel oxides have been demonstrated as coating material for metallic interconnect by extensive works. However, the reasons for their superior properties have not been fully understood, so further study is considered necessary.

This work focuses on their interfacial reaction and long-term stability, electrical conduction behavior and materials optimization for improvement in coating performance and effectiveness. The major objective of this dissertation is to investigate the growth mechanism of the interaction layer and the effect of its existence on the coating and interconnect performance.

The interaction between $(Mn,Co)_3O_4$ spinel coatings and chromia at high temperature is first studied to simulate the spinel coatings' working condition. The mass transport behavior of $(Mn,Co)_3O_4$ spinel oxide will be proposed. Then the physical properties of reaction layer formed during the interaction between $(Mn,Co)_3O_4$ spinel coatings and chromia is investigated by analogous bulk analyses. The transport properties (e.g. electrical conductivity and interface reaction) are related to cation distribution. In spinel oxides, transition metals cations usually have multiple valences. Their site preferences, valence state and electrical conductivity are interrelated, so the cation distribution study can help to understand the degradation in electrical conduction and composition change after the interaction. In the work, the cystal structure and cation distribution in the $(Mn,Co)_3O_4$ based spinel solid solution at SOFC operation temperature is also studied. Finally, the effect of different transition metals doping in manganese cobalt spine coatings is presented on the interaction with chormia for the identification of potential coatings.

In all, this work provide a fundamental understanding of the mass transport properties and phase stability of the $(Mn,Co)_3O_4$ coatings during high temperature operation, which will be beneficial for the development of protective spinel coatings.

CHAPTER 2

Interactions between $(Mn,Co)_3O_4$ coating materials and Cr_2O_3 scale

2.1 Introduction

As described in the first chapter, ceramic coating can provide long-time protection for metallic SOFC interconnects. As compared with perovskite oxides, spinel oxide coatings have shown better performance in reducing the contact resistance and suppressing Cr outward diffusion through the coating layer. However, a relatively thick scale of chromium-rich oxides grows between the spinel coating and chromium forming alloy after long-term operation in the SOFC environment. The interactions between the coating and chromia scale can result in the change in chemical composition and microstructure of the coating, which will then affect coating properties and cell performance.

$(Mn,Co)_3O_4$ spinel oxide is currently considered to be the one of the most promising candidate coatings for SOFC interconnect.[130, 138] The purpose of this part is to investigate the interaction between $(Mn,Co)_3O_4$ coating material and chromia scale at high temperature, and to understand the mass transport properties and phase stability of the $(Mn,Co)_3O_4$ coating. In this chapter, results on the mass transport behavior between manganese cobalt oxides and chromia are presented.

2.2 Experimental procedure

Manganese cobalt oxides $(Mn,Co)_3O_4$ were prepared by solid-state reaction method. MnO (99% pure, Alfa Aesar, Ward Hill, MA) and Co_3O_4 (99.83% pure, Fisher, Pittsburgh, PA) were weighed in appropriate ratio to form the desired stoichiometry. The powders were mixed by ball-milling for 48 h with zirconia milling medium in de-ionized water, and the slurry was dried in an oven at 80 ^oC overnight. The pre-mixed powders were die-pressed into pellets, and then sintered at 1200 ^oC in air to form spinel structure.

The interaction between the prepared $(Mn,Co)_3O_4$ pellets and Cr_2O_3 was studied by placing them together, and heating in air at high temperature in the range of 800 ^oC -1200 ^oC. The sample configurations are shown in Fig. 2.1 (a). In each case, the side of $(Mn,Co)_3O_4$ sample was in contact with Cr_2O_3 (labeled “solid”), while the other side was exposed to air (labeled “vapor”), so that vapor-phase transport from Cr_2O_3 to $(Mn,Co)_3O_4$ could occur. In the experiment, the location of the original interface was marked by applying platinum pastes on the $(Mn,Co)_3O_4$ sample surface prior to the reaction. After reaction, the microstructure and composition of the $(Mn,Co)_3O_4$ samples on the surface and cross sections were characterized using a JEOL JSM-7000F scanning electron microscope (SEM) equipped with energy-dispersive X-ray spectroscopy (EDS). The phase structures of the synthesized and reacted spinels were determined by x-ray powder diffraction (XRD).

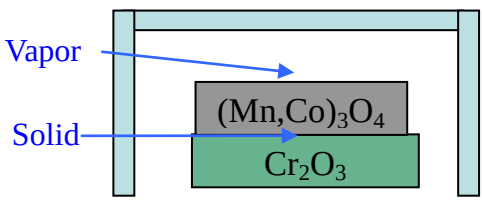

(a)

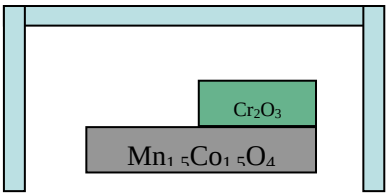

(b)

Fig. 2.1 Schematic diagrams of sample configurations.

2.3 Results and discussions

2.3.1 Surface morphology and structure

The surface morphologies of as-prepared three different $(Mn,Co)_3O_4$ compositions, $Mn_{1.5}Co_{1.5}O_4$, Mn_2CoO_4, and $MnCo_2O_4$ spinel oxides are shown in Fig. 2.2. [149] They were all sintered into a dense body with few isolated pores. The brighter stripe-like parts in Fig. 2.2 (c) have high Co-rich content determined by EDS, which indicates $MnCo_2O_4$ contains two phases after sintered at 1200 ^oC. According to the Mn-Co-O phase diagram, at 1200 °C Mn_2CoO_4 and $Mn_{1.5}Co_{1.5}O_4$ are single-phase spinel solid solution, but $MnCo_2O_4$ have dual phases which consists of a cubic spinel phase (lower cobalt) and a rocksalt phase (higher cobalt). [138]

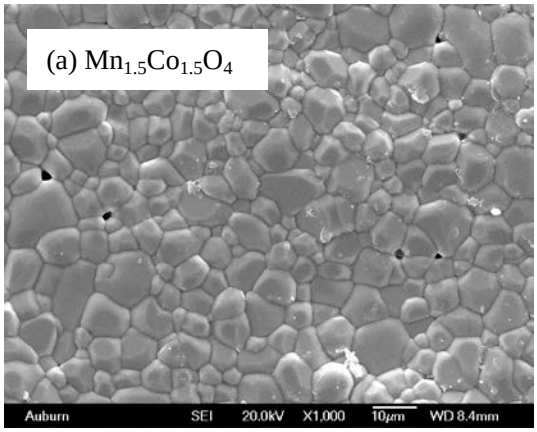

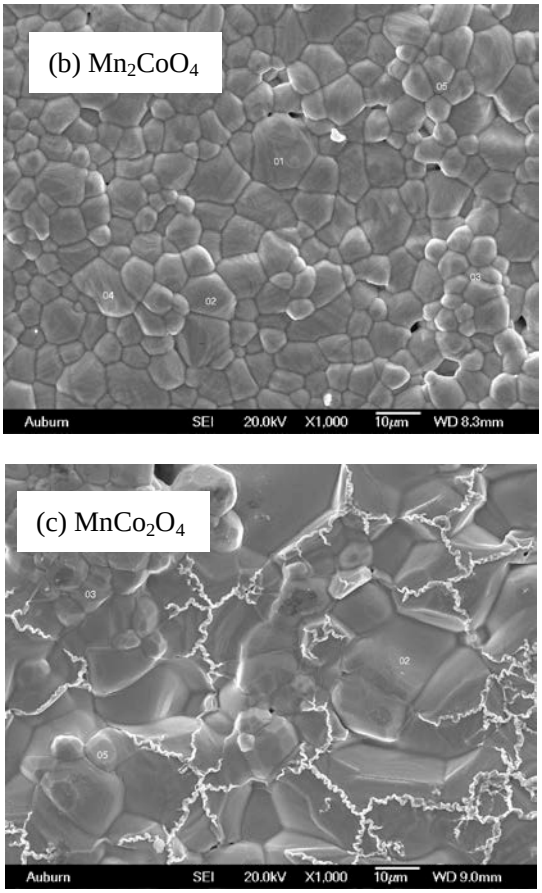

Fig. 2.2 SEM images of as-prepared three $(Mn,Co)_3O_4$ compositions surface: (a) $Mn_{1.5}Co_{1.5}O_4$, (b) Mn_2CoO_4, and (c) $MnCo_2O_4$. [149]

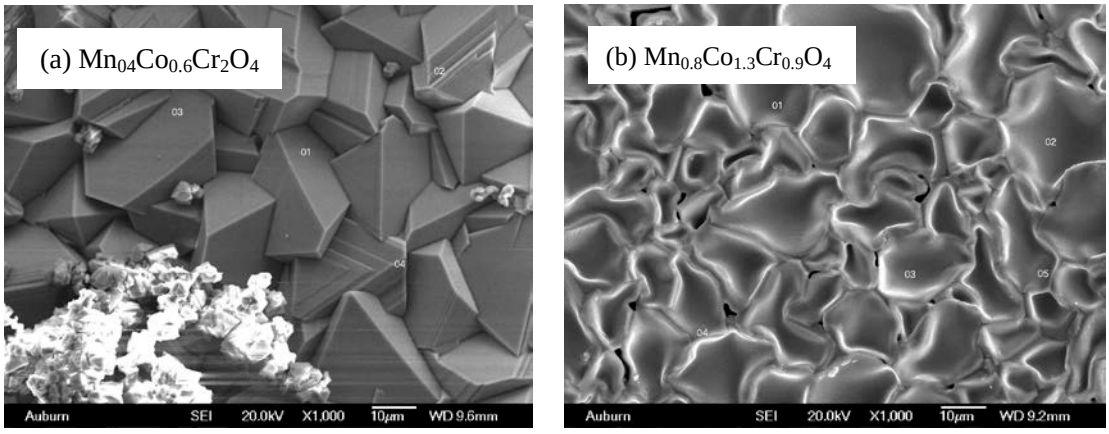

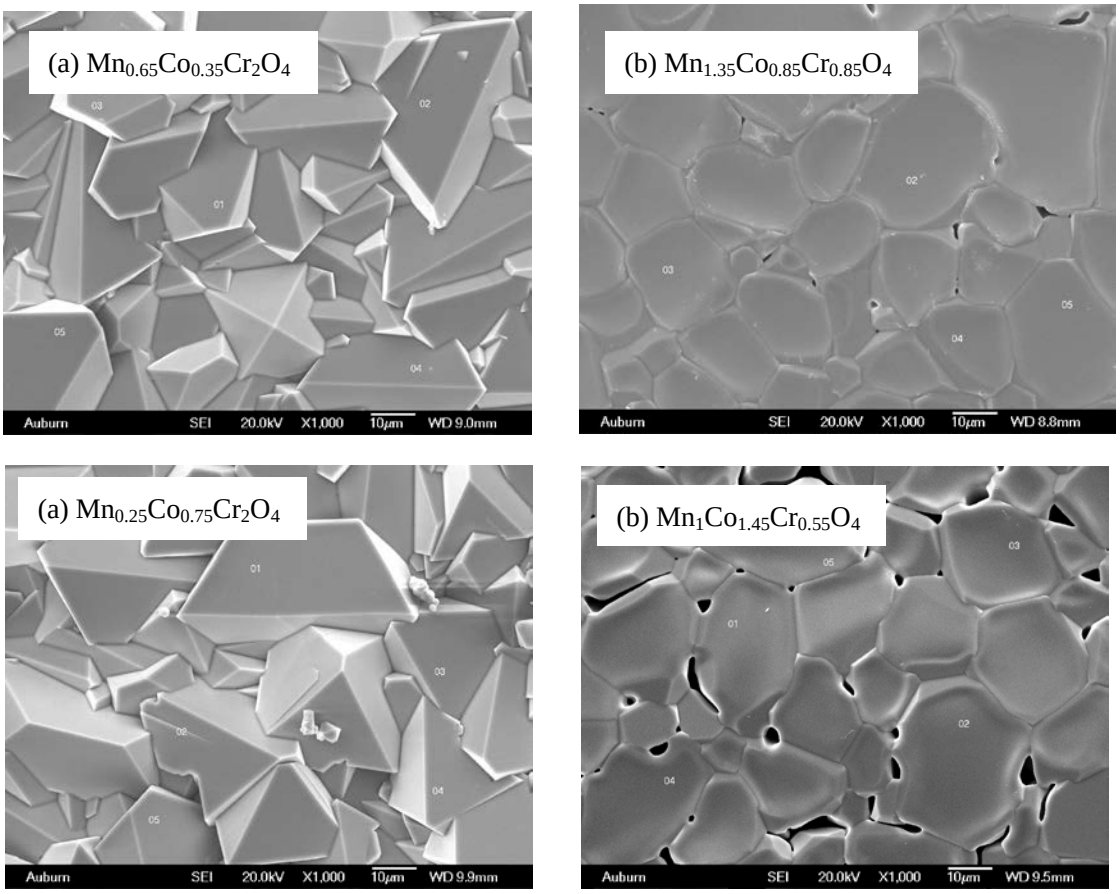

Fig. 2.3 SEM images of surfaces of (a-b) $Mn_{1.5}Co_{1.5}O_4$, (c-d) Mn_2CoO_4, and (e-f) $MnCo_2O_4$ after reaction at 1200 ºC for 72 h in contact with (left) or near chromia (right). [148]

The initial experiments were performed at temperatures higher than the SOFC operation temperature to overcome kinetic limitations. Fig. 2.3 show the SEM images of surface morphologies of $Mn_{1.5}Co_{1.5}O$, $_4Mn_2CoO_4$, and $MnCo_2O_4$ after reaction at 1200 ºC for 72 h in contact with or near chromia (namely, solid side and vapor side), respectively. [148] In spite of the differences in the surface morphology of as-prepared samples, their facetted surface morphologies for the regions in contact with Cr_2O_3 after reaction are similar. EDS analyses show that the reaction products are $(Mn,Co)Cr_2O_4$ spinels, in which the maximum chromium content reached to 2 per M_3O_4 unit. The upper side regions of the $(Mn,Co)_3O_4$ spinel oxides

that are not in direct contact with Cr_2O_3 also reacted via vapor phase transport, but their Cr content was relatively lower. It is shown that the faceted morphology did not form after reaction at 1200 ^oC and faster growth tends to take place at the grain boundary regions.

The chemical compositions of the reaction products by both solid and vapor phase transport are also shown in Fig. 2.3. The Co/Mn ratio in the reaction surfaces was always higher than the original ratio in $(Mn,Co)_3O_4$ spinel oxides, and increased with the cobalt content in the as-prepared $(Mn,Co)_3O_4$ samples, which may be attributed to higher diffusion rate of Co within the reaction layer than that of Mn or the greater preference for tetrahedral site of Co^{2+} compared with that of Mn^{3+}. [147]

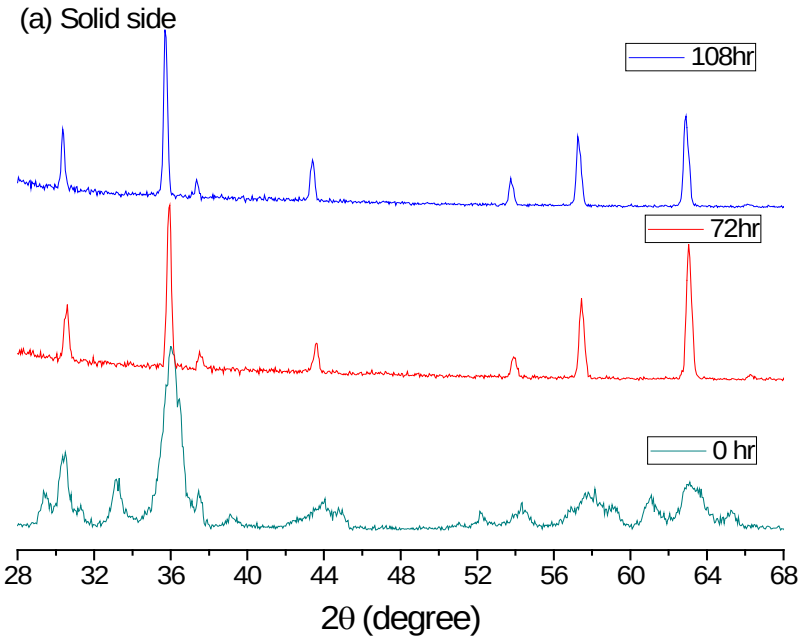

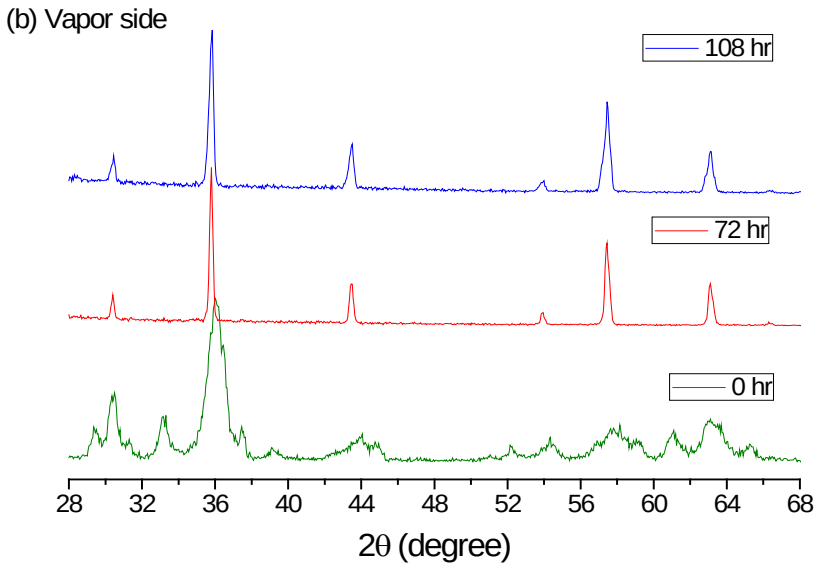

Fig. 2.4 XRD patterns of surfaces of $Mn_{1.5}Co_{1.5}O_4$ after reaction at 1200 ºC (a) in contact with or (b) near chromia for different hours.

Fig. 2.4 plots XRD patterns of surfaces of $Mn_{1.5}Co_{1.5}O_4$ after reaction at 1200 ºC (a) in contact with or (b) near chromia for 72 h and 108 h, respectively. The reaction layers produced by solid phase transport or vapor phase transport both have single cubic spinel structure, which is different from the dual-phase structure in $Mn_{1.5}Co_{1.5}O_4$ at room temperature. XRD analyses also indicate chromium migration can stabilize the cubic structure.

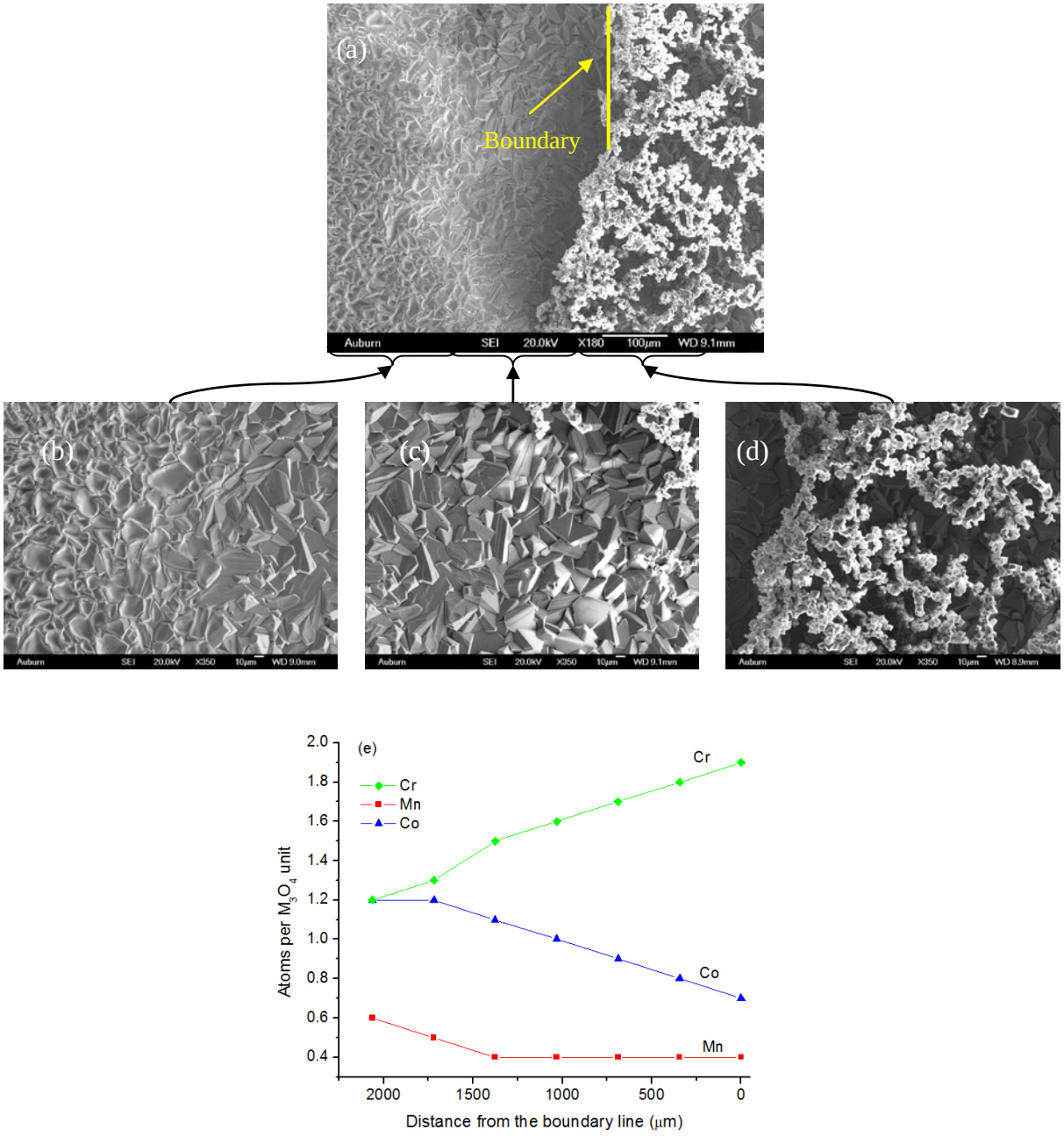

Fig. 2.5 Surface morphologies (a - d) and cation concentration profiles (e) of $Mn_{1.5}Co_{1.5}O_4$ at different distances from Cr_2O_3 (light regions on the right) after reaction at 1200 °C for 144 h.[148]

Fig. 2.5 shows the transition in surface microstructures (a-d) and corresponding cation concentration profiles (e) of $Mn_{1.5}Co_{1.5}O_4$ at different distances from Cr_2O_3 after reaction at

1200 °C for 144 h using sample configurations in Fig. 2.1(b).[148] In this experiment, half of $Mn_{1.5}Co_{1.5}O_4$ surface was covered with chromia shown as light regions on the right in Fig. 2.7(a). The morphology becomes less faceted and the chromium concentration at the surface decreases as moving away from the boundary to left. The Cr_2O_3 activity in the vapor phase is different from Cr_2O_3 scale boundary to the area far away, which would affect the morphology and chromium content in the reaction products. The transition in morphologies is consistent with the difference in the morphologies of interfaces that formed by solid phase transport and vapor phase transport as shown in Fig. 2.3.

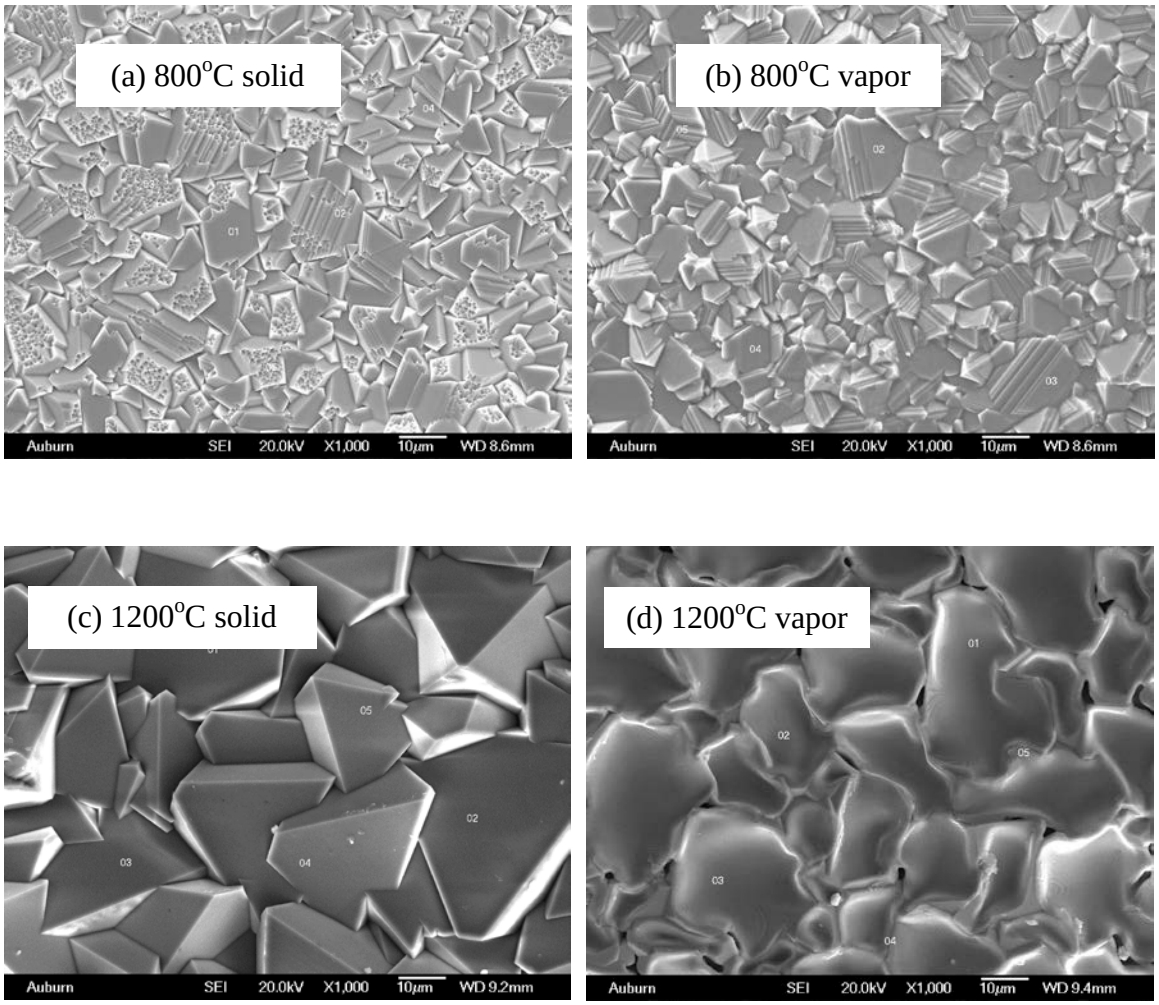

Fig. 2.6 SEM images of surfaces of $Mn_{1.5}Co_{1.5}O_4$ in contact with or near Cr_2O_3 after reaction

at 800 °C and 1200 °C for 144 h. [148]

Table 2.1 The chemical compositions and Co/Mn ratio in surfaces of $Mn_{1.5}Co_{1.5}O_4$ in contact with or near Cr_2O_3 after reaction at 800 °C, 1200 °C for 144 h.

Temperature	chemical compositions		Co/Mn ratio	
	Powder side	Vapor side	Powder side	Vapor side
800 °C	$Mn_{0.3}Co_{0.8}Cr_{1.9}O_4$	$Mn_{1.4}Co_{1.4}Cr_{0.2}O_4$	3.4	1.0
1200 °C	$Mn_{0.4}Co_{0.6}Cr_2O_4$	$Mn_{0.7}Co_{1.3}Cr_{1.0}O_4$	1.5	1.8

Then the reaction temperature is lowered to the typical SOFC operation temperatures. Fig. 2.6 shows surface morphologies of $Mn_{1.5}Co_{1.5}O_4$ in contact with or near Cr_2O_3 after reaction at 800 °C and 1200 °C for 144 h, and their chemical compositions and Co/Mn ratio of the reaction interface are summarized in Table 2.1. [148] For the solid side, a similar faceted microstructure still formed at 800 °C, but both the chromium concentration and grain size in the surface reaction layer decreased with decreasing the temperature. The Co/Mn ratios in the surface layer on both sides were always higher than the original ratio in $Mn_{1.5}Co_{1.5}O_4$ spinel oxide even after reaction at low temperature 800°C.

For the vapor side, chromium content was much lower than that in the side by solid phase transport. After reaction at 800 °C, trace amount of chromium in the reaction layer indicated only a small amount of reaction took place via vapor phase transport. However unlike the morphology for the vapor side at 1200 °C, a facet microstructure was generated as shown in Fig. 2.6 (b). The fact that the degree of faceting for lower Cr contents increases

while reducing the reaction temperature suggests that this faceting mechanism is favored at lower temperatures (e.g. 800 °C).

2.3.2 Mass transport properties in $Mn_{1.5}Co_{1.5}O_4$

The cross sections of $Mn_{1.5}Co_{1.5}O_4$ after reaction at 1000°C for 36 h in contact with Cr_2O_3 are shown in Fig. 2.7. [148] The lighter points in a line in Fig. 2.7 (a) are the platinum markers, which was used to locate the original surface of $Mn_{1.5}Co_{1.5}O_4$ before reaction. A dense layer formed on its surfaces by solid phase transport. For the reaction layer formed by solid phase transport as shown in Fig. 2.7 (a), the Cr_2O_3 layer was on its right side. EDS analysis in Fig. 2.7 (b) showed it contains two scales between $Mn_{1.5}Co_{1.5}O_4$ and Cr_2O_3: a dense $(Mn,Co)Cr_2O_4$ spinel outer scale and a Cr-containing $(Mn,Co,Cr)_3O_4$ intermediate scale. Throughout the outer reaction layer the chromium content remained relatively constant and its maximum value could be reached to 2 per M_3O_4 formula unit. However, in the $(Mn,Co,Cr)_3O_4$ intermediate layer the chromium content was observed to decrease dramatically. Although both reaction layers have the spinel structure, they grow by different mechanisms. After reaction with Cr_2O_3, the fact that $(Mn,Co)Cr_2O_4$ spinel scale on the right of the platinum marker (which locate the original interface) indicates that this outer layer grows by the outward diffusion of manganese and cobalt from $Mn_{1.5}Co_{1.5}O_4$ to the Cr_2O_3, while the $(Mn,Co,Cr)_3O_4$ intermediate layer grows by the inward diffusion of chromium through the outer layer.[149] The growth mechanisms of reaction layer are illustrated schematically in Fig. 2.8. The thickness of Cr-rich reaction layer can also be confirmed by both the platinum markers and Cr concentration profile.

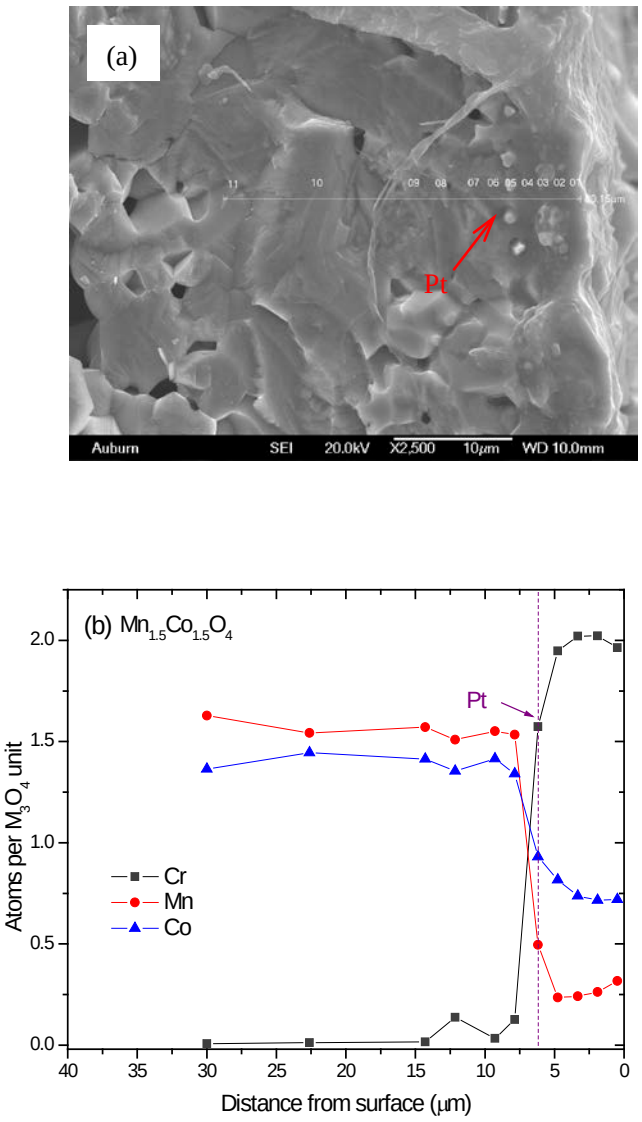

Fig. 2.7 (a) SEM images and (b) cations profile of cross section of $Mn_{1.5}Co_{1.5}O_4$ after reaction at 1000 °C for 36 h in contact with Cr_2O_3. [148]

If the spinel coating is quite thin or not dense enough, the dissolved chromium would finally diffuse throughout the coating to the cathode and then result in chromium poisoning. Therefore, both of the reaction layers are helpful to retard chromium migration and volatilization and then to protect SOFC components.

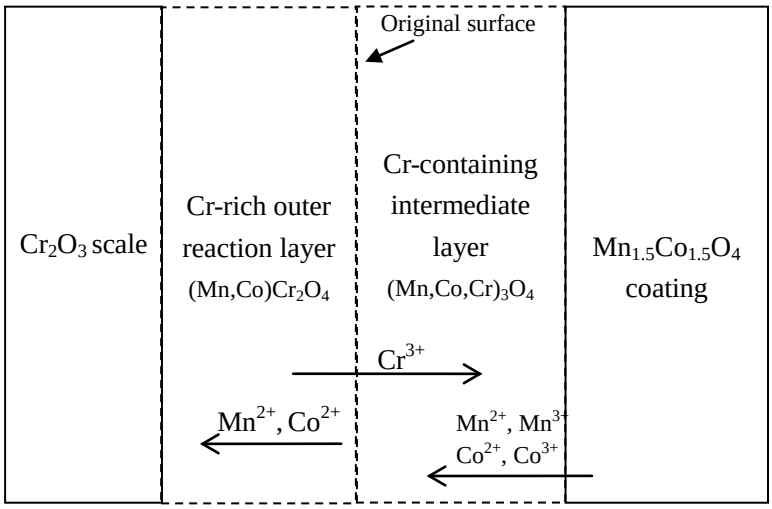

Fig. 2.8 Reaction layers formed during the reaction between $Mn_{1.5}Co_{1.5}O_4$ and Cr_2O_3 at high temperature.

2.4 Conclusions

The interaction between manganese cobalt $(Mn,Co)_3O_4$ spinel oxide coating materials and Cr_2O_3 layer was studied in this chapter. The facetted surface morphologies for the regions in contact with Cr_2O_3 were observed after reaction at both 800 ^oC and 1200 ^oC. EDS and XRD analyses showed that the outer reaction layer are $(Mn,Co)Cr_2O_4$ spinel oxide with a cubic structure, in which the chromium content is reached to the maximum 2 per M_3O_4 unit at steady state (e.g. at 1200 ^oC).

The reaction layer contains two scales, Cr-rich $(Mn,Co)Cr_2O_4$ outer scale and Cr-containing $(Mn,Co,Cr)_3O_4$ intermediate scale. They both have spinel structures, but their growth mechanisms are obviously different. In the outer layer in contact with Cr_2O_3, $(Mn,Co)Cr_2O_4$ grew by the outward diffusion of cobalt and manganese from $(Mn,Co)_3O_4$

coating material. At the same time, chromium dissolved into $(Mn,Co)_3O_4$ and formed the other $(Mn,Co,Cr)_3O_4$ intermediate layer. The growth of the Cr-rich reaction layer is helpful to minimize the migration of chromium species and protect the cathode from poisoning.

.

CHAPTER 3

Electrical properties, cation distributions and thermal expansion of manganese cobalt chromite $Mn_{1.5-0.5x}Co_{1.5-0.5x}Cr_xO_4$ (x = 0 - 2) spinels

3.1 Introduction

As discussed in the first chapter, chromia-forming alloys, especially ferritic stainless steels are widely used as SOFC metallic interconnect. However, their chromium composition also brings some problems. The volatile $CrO_2(OH)_2$ and CrO_3 species deposit on the cathode/electrolyte interface, and cause degradation of cathode electrochemical performance.[43,49] In addition, the electrical conductivity of Cr_2O_3 scale formed on the surface of stainless steels is lower that of alloys, which would increase the overall resistance of fuel cell. [150] Different conductive ceramic coatings have been applied on the surface of metallic interconnects to prevent chromium volatilization and increase oxidation resistance, and $Mn_{1.5}Co_{1.5}O_4$ spinel oxide has been reported to be a promising coating candidate.

To evaluate the long-term stability of $Mn_{1.5}Co_{1.5}O_4$ coating, the transport properties of the reaction layer formed between $Mn_{1.5}Co_{1.5}O_4$ and the Cr_2O_3 scale on the surface of chromium forming alloys need to be characterized, because the interaction can change the coating's composition, and thus its properties, e.g. crystal structure, electrical conductivity and thermal expansion. The mass transport properties of the reaction layer have been

discussed in the second chapter. The reaction layer between $Mn_{1.5}Co_{1.5}O_4$ and Cr_2O_3 is detected to contain two regions in the second chapter, a chromium rich outer layer $(Mn,Co)Cr_2O_4$, and a chromium-containing intermediate layer $(Mn,Co,Cr)_3O_4$. Although both layers have the spinel structure, they form by different mechanisms. Another interesting phenomenon is that the Co/Mn ratio in the reaction layer was observed to be higher than 1, the original coating composition (i.e. $Mn_{1.5}Co_{1.5}O_4$). Both the mass transport and ion transport (reaction layer growth and conductivity behavior) in the reaction layer are highly interrelated with how the cations are distributed on the octahedral and tetrahedral sites in spinel structure. Thus, determination of the atomic occupancies in manganese cobalt chromium spinel system, especially at the SOFC operation temperature 600 ^oC – 800 ^oC, will be useful in understanding the growth and conduction mechanism of reaction layer. Although $(Mn,Co,Cr)_3O_4$ are the major compositions in the reaction layer, the information on their cation distributions is still lacking at high temperature under oxidizing atmosphere relevant to SOFC working environment. Since Mn, Co and Cr have similar numbers of electrons, the differences in x-ray scattering between them are small. However their neutron scattering lengths are quite different, 3.635 $x10^{-15}$m for Cr, -3.73 $x10^{-15}$ m for Mn, and 2.49 $x10^{-15}$m for Co.[151] So the in-situ neutron diffraction technique is employed here as an effective method to study cation distributions and other crystallographic parameters of $(Mn,Co,Cr)_3O_4$ in the temperature range of 600 ^oC - 800^oC in air.

To investigate the effect of Cr migration on the $Mn_{1.5}Co_{1.5}O_4$ coating performance, manganese cobalt spinels with different chromium content, $Mn_{1.5-0.5x}Co_{1.5-0.5x}Cr_xO_4$ (x = 0 - 2), were synthesized. This work focuses on their electrical conductivity, cation distributions

and thermal expansion at SOFC operation condition. The relationship of cation distributions with transport properties in the reaction layer was also discussed.

3.2 Experimental

$Mn_{1.5-0.5x}Co_{1.5-0.5x}Cr_xO_4$ (x = 0 - 2) spinel oxides were synthesized by solid state reaction. MnO (99% pure, Alfa Aesar, Ward Hill, MA), Co_3O_4 (99.83% pure, Fisher, Pittsburgh, PA) and Cr_2O_3 (99% pure, Acros, Geel, Belgium) were weighed in appropriate ratio to form the desired stoichiometry. Then the powder mixtures were ball-milled for 48 h with zirconia milling medium in de-ionized water, and dried overnight in an oven. The pre-mixed powders were die-pressed, and then sintered at 1200 ^oC in air to form spinel structure. X-ray diffraction (XRD) was used for phase analysis by a Bruker D8 X-ray diffractometer. The samples were scanned over the 2θ range of 28^o-70^o with the Cu K_α radiation at room temperature. The in-situ high-temperature neutron diffraction measurements were performed on the high resolution neutron powder diffractometer (HB-2A) with a wavelength of $\lambda = 1.537\,\overset{o}{A}$ at Oak Ridge National Lab, Oak Ridge, USA. Since the vanadium could be easily oxidized in air at high temperature, a quartz sample holder was used due to its excellent chemical stability. Samples were placed in a quartz holder, and loaded into a tube furnace, which would be heated up to 800 ^oC under air atmosphere. The data were collected in the 2θ range of 8^o to 152^o, and refined by the FULLPROF program using Rietveld method.[152] The electrical conductivities of spinel samples were measured by four-probe d.c. method on rectangular bars with the dimension about 14 mm x 5 mm x 2 mm which were cut from sintered specimens. The measurements were conducted between 500^oC

and 900^{o}C in random direction leaving enough time (10 h) to reach equilibration. Pt paste and wire were used as current collector and electrodes. A current chosen from 10-100 mA was applied during measurement. The coefficients of thermal expansion (CTEs) of the specimens were tested from a Unitherm^{TM} model 1161V high temperature vertical dilatometer (Lewisville, TX) from room temperature up to 1000 ^{o}C with a heating rate of 10 ^{o}C/min in air. The average CTE value was obtained from the difference of thermal expansion between 1000 ^{o}C and room temperature divided by temperature difference.

3.3 Results and Discussion

3.3.1 X-ray diffraction

The spinel structures include cubic phase (e.g. JCPDS No. 23-1237 for manganese cobalt oxide and No. 26-0474 for manganese cobalt chromium oxide) or tetragonal phase (e.g. JCPDS No. 18-0408 for manganese cobalt oxide). [153] Fig. 3.1 shows the XRD patterns of $Mn_{1.5-0.5x}Co_{1.5-0.5x}Cr_xO_4$ (x= 0 - 2) spinel oxides at room temperature. Peaks positions indicated $Mn_{1.5}Co_{1.5}O_4$ contains two phases, which is consistent with Yang *et al*'s results.[130,138] The crystal structure of $Mn_{1.5}Co_{1.5}O_4$ at room temperature is dual-phase including cubic Co-rich $Mn_{1+\alpha}Co_{2-\alpha}O_4$ (Space group: $Fd\bar{3}m$) and tetragonal Mn-rich $Mn_{2-\delta}Co_{1+\delta}O_4$ (Space group: $I4_1/amd$), respectively. [130,154] As Cr content increased, the tetragonal phases become vanished. When x is greater than 1, XRD indicated $Mn_{1.5-0.5x}Co_{1.5-0.5x}Cr_xO_4$ forms the single cubic phase. With increasing chromium doping, the cubic spinel structure can be stabilized at room temperature.

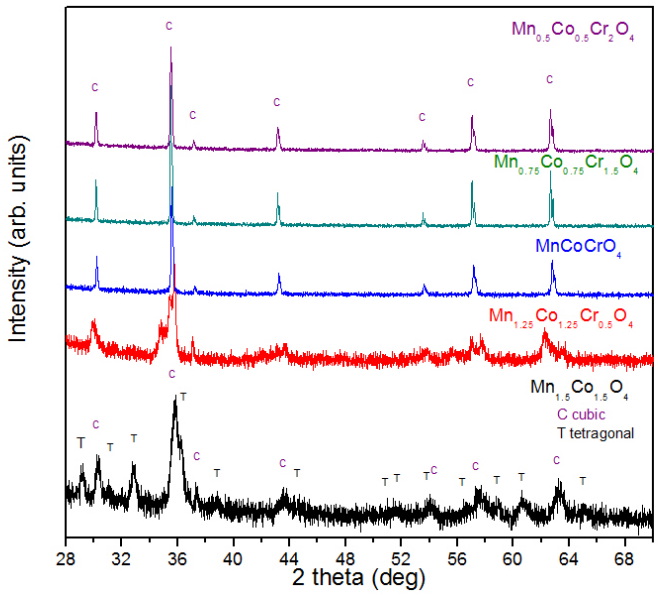

Fig. 3.1 XRD patterns of $Mn_{1.5-0.5x}Co_{1.5-0.5x}Cr_xO_4$ (x= 0 - 2) spinel oxides at room temperature.

Table 3.1 lists the lattice parameter and different kinds of density of cubic $Mn_{1.5-0.5x}Co_{1.5-0.5x}Cr_xO_4$ (x=1, 1.5, and 2). Their lattice parameter did not change much as chromium content increased. The lattice size of the cubic spinel structure is related to the ionic radius and site atomic occupancies. The different cations' radii are listed as following: R_{Cr}^{3+}(CN=VI) = 0.615 Å, R_{Mn}^{3+} (CN=VI) = 0.645 Å, R_{Mn}^{2+}(CN=IV) = 0.66 Å, R_{Co}^{3+}(CN=VI) = 0.545 Å, and R_{Co}^{2+}(CN=IV) = 0.58 Å.[155] It is shown that the size of Cr^{3+}(VI) is intermediate between those of Mn and Co cations. The distribution occupancies of these three cations at the octahedral (M) and tetrahedral (T) sites would vary when Cr concentration increased. Both factors could affect the change in lattice parameters. Their measured density was obtained from the weight and geometric dimensions of samples, and the theoretical density was calculated from lattice parameters. A decrease in the relative density was shown as Cr content increased, which indicates that Cr-rich spinel oxides have a

poor sinterability.

Table 3.1 Lattice parameter and density of cubic $Mn_{1.5-0.5x}Co_{1.5-0.5x}Cr_xO_4$ (x= 1, 1.5, and 2).

	Lattice parameter a(Å)	Theoretical density (g/cm^3)	Measured density (g/cm^3)	Relative density (%)
$MnCoCrO_4$	8.366	5.214	3.64	70
$Mn_{0.75}Co_{0.75}Cr_{1.5}O_4$	8.379	5.130	3.18	62
$Mn_{0.5}Co_{0.5}Cr_2O_4$	8.380	5.076	2.79	56

3.3.2 Electrical conductivity

Fig. 3.2 shows the conductivity of $Mn_{1.5-0.5x}Co_{1.5-0.5x}Cr_xO_4$ (x=0 - 2) at 800 °C, the typical SOFC operation temperature. The conductivity decreases dramatically by several orders of magnitude as the Cr content increases. The conductivity at 800 °C drops from 60 S/cm [130] to 0.007 S/cm by three orders of magnitude as *x* increases from 0 to 2 in $Mn_{1.5-0.5x}Co_{1.5-0.5x}Cr_xO_4$. The increase in porosity may contribute to the decrease in the conductivity. The temperature dependences of conductivity of $Mn_{1.5-0.5x}Co_{1.5-0.5x}Cr_xO_4$ are shown in Fig. 3.3. The conductivity of all samples increased with the temperature. A linear dependence of $\log(\sigma T)$ with 1000/T is observed, which was also reported in other spinels, and suggests that the conduction in the spinel oxides occurs through the small polaron hopping mechanism on the octahedral site during high temperature as described by[121, 156-158]

$$\sigma = \frac{\sigma_0}{T}\exp(-\frac{E_a}{k_b T}) \quad (3.1)$$

where, σ is the electrical conductivity,

T is the absolute temperature,

σ_0 is the pre-exponential factor,

E_a is the activation energy,

and k_b is the Boltzmann's constant.

The activation energies (E_a) calculated from the slope of the fitting lines in Fig. 3.3 are shown in Fig. 3.4. The activation energy increases with the Cr content, which indicates Cr doping makes electrical conduction difficult in $Mn_{1.5}Co_{1.5}O_4$. With small Cr content doping, the conductivity decreases with unchanged increase in activation energy (e.g. x lower than 1.0), but the activation energy increases at higher Cr contents. This may indicate the mechanism does not change for low Cr content (i.e. a decrease number of available octahedral sites), but the change in activation energy at high Cr level doping may suggest other conduction process might be involved.

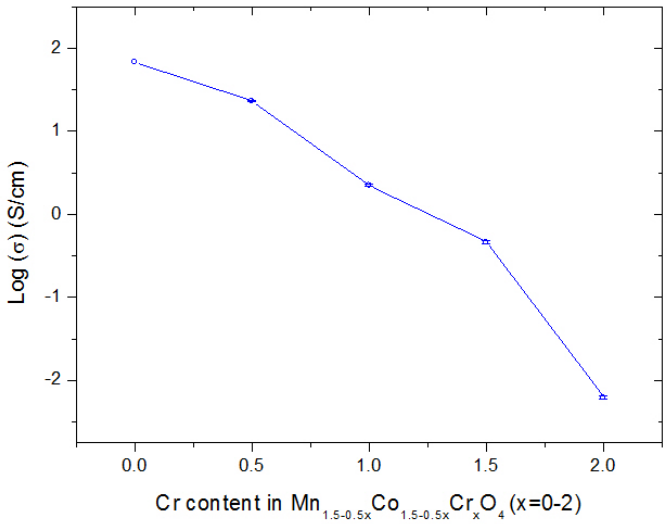

Fig. 3.2 Electrical Conductivity of $Mn_{1.5-0.5x}Co_{1.5-0.5x}Cr_xO_4$ (x = 0 - 2) spinel oxides at 800 ^oC in air.

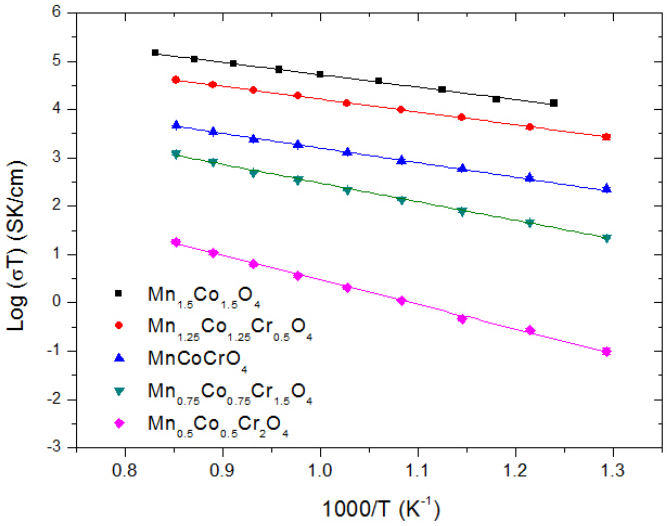

Fig. 3.3 Electrical Conductivity of $Mn_{1.5-0.5x}Co_{1.5-0.5x}Cr_xO_4$ (x = 0 - 2) spinel oxides as a function of 1000/T in air.

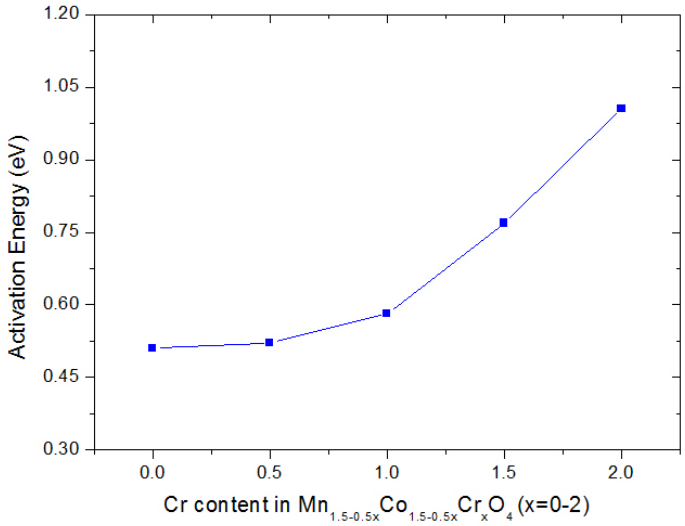

Fig. 3.4 Activation Energy as a function of Cr content in $Mn_{1.5-0.5x}Co_{1.5-0.5x}Cr_xO_4$ (x = 0 - 2) spinel oxides.

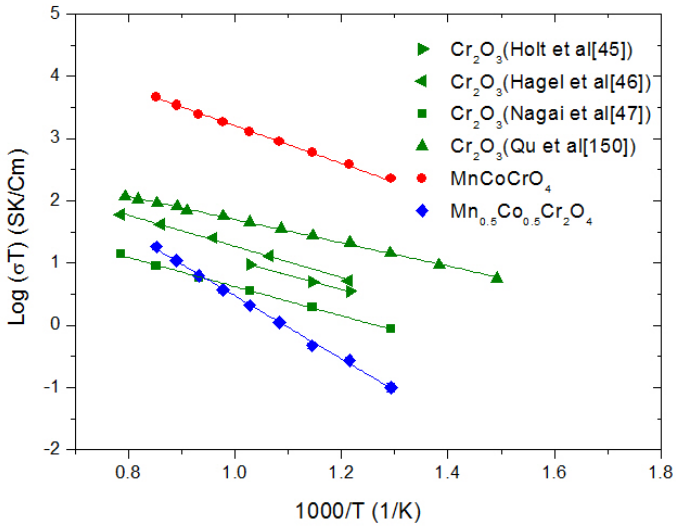

Fig. 3.5 Comparison between $Mn_{1.5-0.5x}Co_{1.5-0.5x}Cr_xO_4$ (x =1 and 2) and Cr_2O_3 in electrical conductivity in air.

Comparisons between $Mn_{1.5-0.5x}Co_{1.5-0.5x}Cr_xO_4$ (x = 1 and 2) and Cr_2O_3 in electrical conductivity in air are shown in Fig. 3.4. The Cr_2O_3 scale formed on the stainless steel interconnect will also be part of the cell circuit. The conductivity of Cr_2O_3 at 800^{o}C in air is in the range of 0.006 to 0.16 S/cm,[44-48] which is comparable to that of Cr-rich spinel samples with x =1.5 and 2. The results indicate that the existence of both reaction layer and Cr_2O_3 scale would increase the overall cell resistance, so it is important to suppress their further growth.

As for the conductivity in the spinel oxides, Lu et al attributed the electrical conduction in the $Mn_{1+x}Cr_{2-x}O_4$ system to the hopping of small polaron between Mn^{3+} and Mn^{4+} on the octahedral site. [77] So increasing Cr content will lead to a reduction in the concentrations of exchange pairs between Mn^{3+} and Mn^{4+} concentration and therefore the conductivity value. In the $Mn_{1.5-0.5x}Co_{1.5-0.5x}Cr_xO_4$ ternary system, Co can also have multiple valence states, and

all these three cations have quite different site preferences.[155,159] The details about cation distributions and its relationship to conductivity will be discussed with the neutron diffraction data in the following section.

3.3.3 Cation distribution in $Mn_{1.5}Co_{1.5}O_4$ and $MnCoCrO_4$ at high temperature

The neutron diffraction patterns for $Mn_{1.5}Co_{1.5}O_4$ and $MnCoCrO_4$ at 600 °C and 800 °C under air atmosphere are given in Fig. 3.6 and Fig. 3.7, respectively. These two samples' detailed crystallographic information can help to understand the transport properties of interactions between $Mn_{1.5}Co_{1.5}O_4$ coating and Cr_2O_3 scale during SOFC operation.

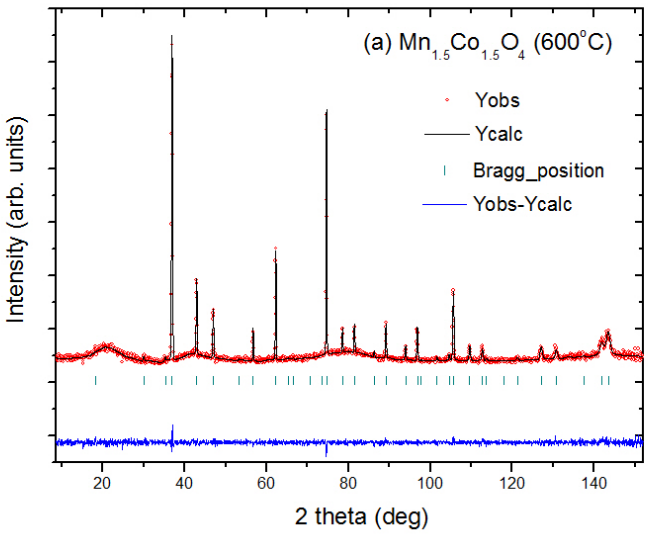

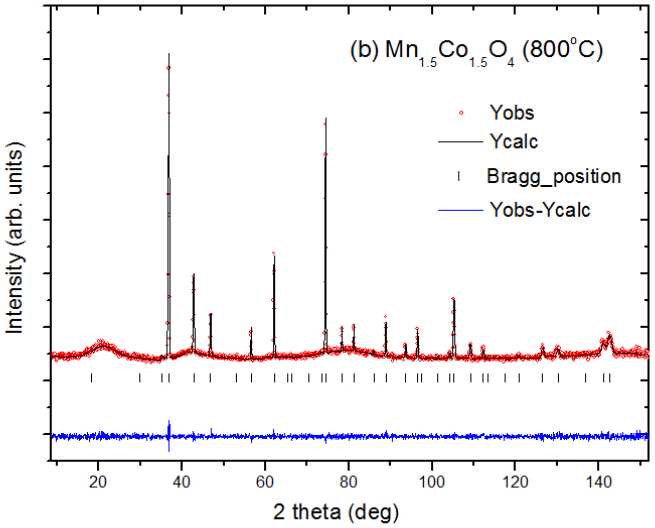

Fig. 3.6 Neutron diffraction patterns of $Mn_{1.5}Co_{1.5}O_4$ in air at (a) 600 ^oC and (b) 800 ^oC, respectively.

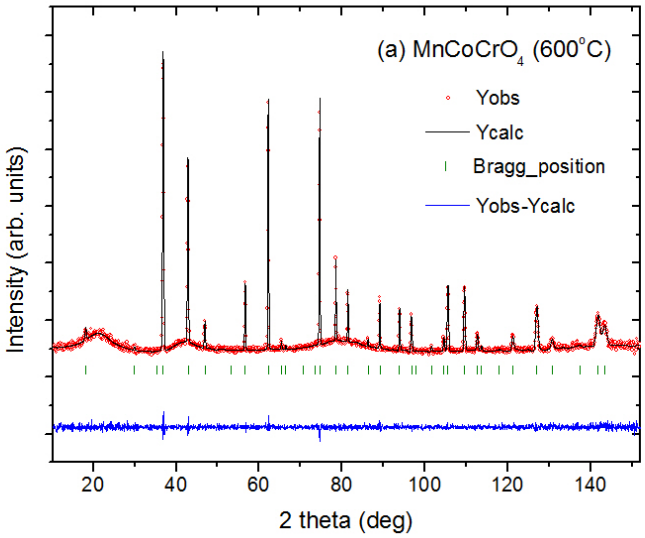

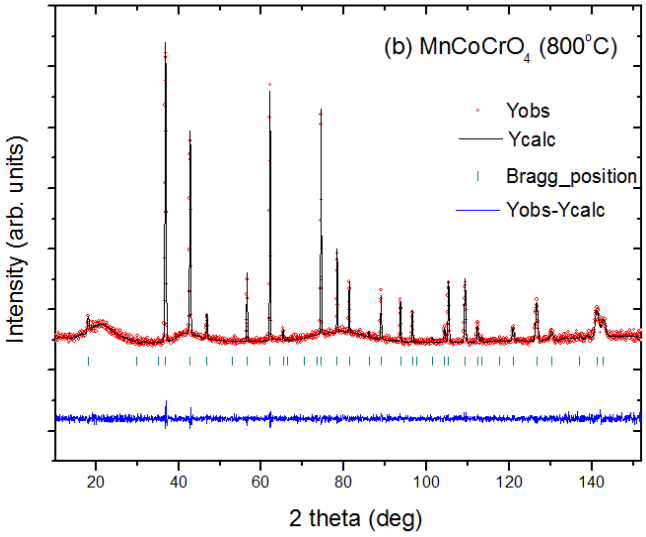

Fig. 3.7 Neutron diffraction patterns of $MnCoCrO_4$ at (a) 600 °C and (b) 800 °C, respectively.

Table 3.2 Crystal parameters of (a) $Mn_{1.5}Co_{1.5}O_4$ and (b) $MnCoCrO_4$ at high temperature

(a) Crystal parameters of $Mn_{1.5}Co_{1.5}O_4$ (Space group: $Fd\bar{3}m$ (227))

	600°C	800°C
a (A)	8.4129(1)	8.4331(1)
u oxygen	0.26164(9)	0.26176(9)
$[Mn]_T$	0.151(10)	0.209(9)
$[Co]_T$	0.849(10)	0.791(9)
$[Mn]_M$	0.689(7)	0.682(7)
$[Co]_M$	0.311(7)	0.318(7)
R_{wp} (%)	5.27	5.07
R_{exp} (%)	4.61	4.70

(b) Crystal parameters of $MnCoCrO_4$ (Space group: $Fd\bar{3}m$ (227))

	600°C	800°C
a (A)	8.4140(1)	8.4301(1)
u oxygen	0.26211(6)	0.26207(7)
$[Mn]_T$	0.252(9)	0.271(9)
$[Co]_T$	0.748(9)	0.729(9)
$[Mn]_M$	0.418(4)	0.398(5)
$[Co]_M$	0.082(4)	0.102(5)
$[Cr]_M$	0.500(0)	0.500(0)
R_{wp} (%)	4.82	4.86
R_{exp} (%)	4.35	4.35

* $R_{wp} = 100[(\sum_{i=1,n} w_i|y_i - y_{ci}|^2) / \sum_{i=1,n} w_i y_i^2]^{1/2}$, $R_{exp} = 100[(n-p) / \sum_i w_i y_{oi}^2]^{1/2}$, where y_i and y_{ci} are the observed and calculated numbers of counts at point i of the neutron diffraction pattern, w_i is the weigh of the observation = 1/variance$(obs)_i$, R_{exp} is calculated supposing the best possible mode, and n-p is the number of degrees of freedom.

The broad background spectrum was from the quartz sample holder, but a good contrast of diffraction peak intensity was still obtained. The refined crystal parameters of (a) $Mn_{1.5}Co_{1.5}O_4$ and (b) $MnCoCrO_4$ are listed in Table 3.2. $Mn_{1.5}Co_{1.5}O_4$ is shown a single cubic phase (Space group: $Fd\bar{3}m$) from 600 °C to 800°C in Fig. 3.6, which is different from its dual-phase structure at room temperature. In the general spinel AB_2O_4, O anions form a cubic close-packing in which A and B cations occupy the tetrahedral (T) and octahedral (M) sites,

and it can be expressed as $(A_{1-x}B_x)[A_{x/2}B_{1-x/2}]_2O_4$, where the parentheses represent cations on tetrahedral site, and square brackets represent cations on octahedral sites.[117,119] Since $Mn_{1.5}Co_{1.5}O_4$ contains only Mn and Co cations, the occupancies of these two at the same site are constrained to be one. Its refined crystallographic formula at 800°C is $(Mn_{0.209}Co_{0.791})[Mn_{0.682}Co_{0.318}]_2O_4$. Its lattice size increased from 600°C to 800°C due to thermal expansion, but its site occupancies did not vary significantly. More Mn cations occupied the octahedral sites, and more Co cations occupied on the tetrahedral sites, although the Co/Mn chemical ratio is 1 in $Mn_{1.5}Co_{1.5}O_4$.

For $MnCoCrO_4$, all cations' occupancies were first refined without any constraint, but the chemical formula obtained from the refinement is quite different from the nominal formula. For the ternary system, neutron diffraction is difficult to determine more than two cations' distributions in the same site (octahedral and tetrahedral) directly, so reasonable constraints have to be applied to the refinement. Navrotsky et al studied the thermodynamics of site preference for individual cations in the spinel structure, and found Cr^{3+} had the strongest octahedral site preference. [147] Cr^{3+} were also reported exclusively occupied the octahedral site in the Cr-containing spinels. [77,121,160] Based on these results, the octahedral site was constrained to be fully occupied with 50% occupation by Cr^{3+}, and an agreement between the refined chemical formula with its nominal was achieved. The reliability of the refinement results were estimated from the agreement factors R_{wp} and R_{exp}, which are listed in Table 3.2 (b). The crystal structure of $MnCoCrO_4$ at high temperature is also a single cubic phase with space group $Fd\bar{3}m$ (227), and its lattice parameter expanded as increasing the temperature. Similar to $Mn_{1.5}Co_{1.5}O_4$, the occupancy of Co at tetrahedral site was much

greater than that of Mn, which exhibited Co cations preferred the tetrahedral sites, while Mn cations like the octahedral sites. As mentioned above, the electrical conduction is related with cations on the octahedral sites. Both Mn and Co cations were found distributed in the octahedral sites in $Mn_{1.5}Co_{1.5}O_4$ and $MnCoCrO_4$, respectively. It was reported that Co could have multiple valences in spinel oxides, e.g. III (+3 valence state with low spin) and +2 which was determined by thermal analysis.[159] This indicates Co may also make contributions to the electrical conduction. In the unit cell of cubic spinel, there are four layers of octahedral chains, and each octahedral site is surrounded by six nearest octahedral neighbors. Using Mn on the octahedral sites as an example, the refined results at 800^{o}C indicate that there are about 4 (6 x 0.682) nearest Mn cations on average for small polaron hopping on Mn cation at octahedral sites in $Mn_{1.5}Co_{1.5}O_4$. In $MnCoCrO_4$ the number of nearest Mn cations is decreased to around 2 (6 x 0.398). There is also a reduction in the available neighboring octahedral sites for hopping between Co cations after Cr doping. Therefore, as more Cr cations occupy the octahedral site with a fixed valence +3, [77,121,160] the contents of exchange pairs Mn^{3+}/Mn^{4+} and Co^{2+}/Co^{III} decrease, so the conductivity of $Mn_{1.5-0.5x}Co_{1.5-0.5x}Cr_xO_4$ is reduced. In addition, the tetrahedral site preference of Co over Mn obtained from neutron diffraction data could somewhat explain the reason for higher Co/Mn ratio in the reaction layer between $Mn_{1.5}Co_{1.5}O_4$ and Cr_2O_3 as investigated in the second chapter. Both Cr^{3+} and Mn^{3+} prefer octahedral sites during the interaction between $Mn_{1.5}Co_{1.5}O_4$ coating and Cr_2O_3 scale, so Co^{2+} tends to occupy the tetrahedral site. The neutron diffraction technique provides useful crystallographic information in understanding the transport mechanism in the reaction layer.

3.3.4 Thermal expansion test

Thermal expansion compatibility is required to reduce the thermal stress and avoid component spallation for good long-term performance. Fig. 3.8 shows the CTEs of $Mn_{1.5-0.5x}Co_{1.5-0.5x}Cr_xO_4$ (x = 0 - 2) spinel oxides from room temperature to 1000°C in air. The CTE of Cr_2O_3 from 25°C - 900°C, 9.6 $x10^{-6}$/°C is shown for comparison.[151] As Cr content increased, CTE of $Mn_{1.5-0.5x}Co_{1.5-0.5x}Cr_xO_4$ spinel oxides decreased, which indicates Cr diffusion from Cr_2O_3 layer can reduce the thermal expansion of $Mn_{1.5}Co_{1.5}O_4$ coating. Thus, the growth of the reaction layer formed between $Mn_{1.5}Co_{1.5}O_4$ coating and Cr_2O_3 scale on the surface of metallic interconnects could lead to thermal stresses from the CTE mismatch and local spallation after long-time operation.

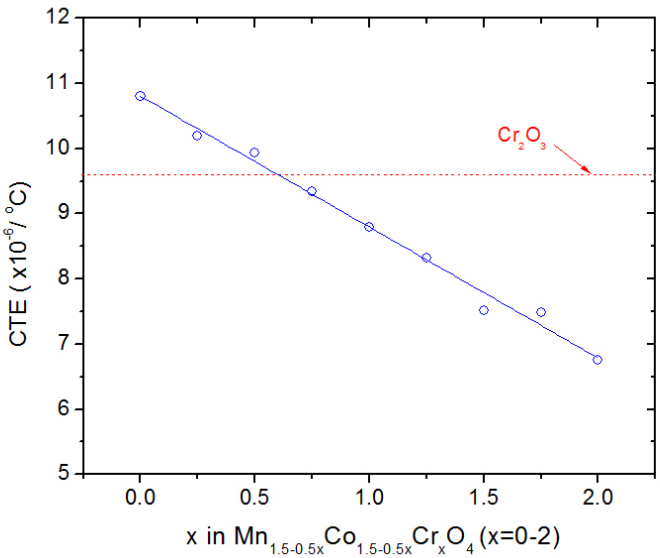

Fig. 3.8 CTEs of $Mn_{1.5-0.5x}Co_{1.5-0.5x}Cr_xO_4$ (x=0-2) spinel oxides and Cr_2O_3[151] from room temperature up to 1000°C in air.

3.4 Conclusions

$Mn_{1.5-0.5x}Co_{1.5-0.5x}Cr_xO_4$ (x = 0 - 2) spinel oxides were synthesized by solid state reaction. The effects of Cr doping were studied on the crystal structure, electrical conductivity and thermal expansion at SOFC operation condition, and the relationship between cation distributions and transport properties in the reaction layer were discussed. With increasing Cr content, the cubic phase at room temperature is stabilized, the electrical conductivity decreases dramatically by several orders of magnitude, and CTE also decreases. The temperature dependence of conductivity suggested a small polaron hopping conduction mechanism in $Mn_{1.5-0.5x}Co_{1.5-0.5x}Cr_xO_4$. The refinements of neutron diffraction data for $Mn_{1.5}Co_{1.5}O_4$ and $MnCoCrO_4$ show they both were cubic structure at SOFC operation temperature, and indicate Mn prefers the octahedral sites, while Co prefers the tetrahedral sites, which is consistent with the Co/Mn ratio in the reaction layer keeping higher than that in the original coating. The formation of a Cr-containing reaction layer between the oxidation scale and the $(Mn,Co)_3O_4$ spinel coating could lead to an increase in electrical resistance and thermal stresses. Based on this work, reducing the thickness of Cr-containing reaction layer could improve the overall electrical conduction of ceramic coating.

CHAPTER 4

Electrical properties of transition metal (TM)-doped $(Mn,Co)_3O_4$ (TM = Fe, Ti) spinels and their interaction with chromia for SOFC interconnect coatings

4.1 Introduction

Manganese cobalt spinel oxides $(Mn,Co)_3O_4$ are promising coating candidates which can be applied on SOFC metallic interconnect ferritic stainless steels. However, the CTE value of $MnCo_2O_4$ is larger than that of ferritic stainless steels. In addition, as discussed in the third chapter, the formation of the Cr-containing reaction layer between the Cr_2O_3 scale and the $(Mn,Co)_3O_4$ spinel coating could lead to an increase in the electrical resistance and thermal stresses due to its low electrical conductivity and CTE mismatch. Therefore, adjusting CTE of coating material and depressing the growth of its reaction layer could reduce its effect on the overall cell performance, and cation doping in the coating material is considered. In this work, the high temperature electrical properties of transition metal (TM)-doped $MnCo_{2-x}TM_xO_4$ (TM = Fe and Ti) and their interaction with chromia were investigated as potential SOFC interconnect coatings.

4.2 Experimental

$MnCo_{2-x}TM_xO_4$ (TM = Fe, x = 0 - 0.7; TM = Ti, x = 0.34) spinel oxides spinel oxides were synthesized by solid state reaction. MnO (99% pure, Alfa Aesar, Ward Hill, MA), Co_3O_4 (99.83% pure, Fisher, Pittsburgh, PA) and Fe_3O_4 (99.99% pure, Alfa Aesar, Ward Hill, MA) or TiO_2 (99.17% pure, Fisher, Pittsburgh, PA) were weighed in appropriate ratio to form the desired stoichiometry. Then the powder mixtures were ball-milled for 48 h with zirconia milling medium in de-ionized water, and the slurry was dried overnight in an oven. The pre-mixed powders were die-pressed, and then sintered at 1200^{o}C in air to form spinel structure.

X-ray diffraction (XRD) was used for phase analysis by a Bruker D8 X-ray diffractometer. The samples were scanned over the 2θ range of 28-68^o with the Cu K_α radiation at room temperature. The in-situ high-temperature neutron diffraction measurements were performed on the high resolution neutron powder diffractometer (HB-2A) with a wavelength of $\lambda = 1.539\,\text{Å}$ at Oak Ridge National Lab, Oak Ridge, USA. A quartz sample holder was used due to its excellent chemical stability. Samples were placed in a quartz holder, and loaded into a tube furnace, which would be heated in air atmosphere. The data were collected in the 2θ range of 8^o to 152^o, and refined by the FULLPROF program using Rietveld method.[153] The electrical conductivity of spinel samples were measured by four-probe d.c. method on rectangular bars with the dimension about 14 mm x 5 mm x 2 mm which were cut from sintered specimens. The measurements were conducted between 500^{o}C and 900^{o}C in random order leaving 10 h to reach equilibration. Pt paste and wire were used as current collector and electrodes. A current chosen from 300mA -500mA was applied during

measurement. The coefficients of thermal expansion (CTEs) of the specimens were tested from a Unitherm^{TM} model 1161V high temperature vertical dilatometer (Lewisville, TX) from room temperature up to 1000^{o}C with a heating rate of 10 ^{o}C/min in air. The average CTE value was obtained from the difference of thermal expansion between 1000 ^{o}C and room temperature divided by temperature difference.

The interaction between the prepared $MnCo_{2-x}TM_xO_4$ pellets and Cr_2O_3 was performed by placing the pellets in contact, and heating in air at high temperature at 800 ^{o}C and 900^{o}C using the sample configurations as shown in Fig. 2.1 (a). After reaction, the microstructure and composition of the $MnCo_{2-x}TM_xO_4$ samples on the surface and cross sections were characterized using a JEOL JSM-7000F scanning electron microscope (SEM) equipped with energy-dispersive X-ray spectrum (EDS).

4.3 Results and Discussions

4.3.1 X-ray diffraction

Fig. 4.1 shows the XRD patterns of $MnCo_{2-x}Fe_xO_4$ (x= 0 - 0.7) spinel oxides at room temperature. Peaks positions indicated all the $MnCo_{2-x}Fe_xO_4$ (x= 0.15-0.7) spinel samples have single cubic structure with space group $Fd\bar{3}m$ after sintering. It is shown that as the iron content increases, the diffraction peaks shift left to the lower angle range. According to the Bragg's Law, $2d \cdot \sin\theta = \lambda$, a smaller θ will lead to a larger d-spacing, and therefore a larger lattice parameter. So the lattice size increases as increasing the iron concentration in $MnCo_{2-x}Fe_xO_4$. The lattice parameter (a) of $MnCo_{2-x}Fe_xO_4$ unit cell is listed as follows:

8.285 Å, 8.318 Å, 8.341 Å, 8.372 Å, and 8.398 Å as x increases from 0 to 0.7. The ionic radius could affect the lattice size of this cubic spinel structure. The radii of manganese, cobalt, and iron cations are in the following: R_{Mn}^{3+} (CN=VI) = 0.645 Å, R_{Mn}^{2+}(IV) = 0.66 Å, R_{Co}^{3+}(VI) = 0.545 Å, and R_{Co}^{2+}(IV) = 0.58 Å, R_{Fe}^{3+}(CN=VI) = 0.645 Å, R_{Fe}^{2+}(IV) = 0.63 Å.[155] It is apparent that the size of Fe^{3+}(VI) or Fe^{2+}(IV) is bigger than those of Co^{3+}(VI) or Co^{2+}(IV) cations. In $MnCo_{2-x}Fe_xO_4$ spinel oxides, the Mn content is fixed to 1. So increasing Fe content, the Co concentrate will be decreased, and thus the lattice size will expand.

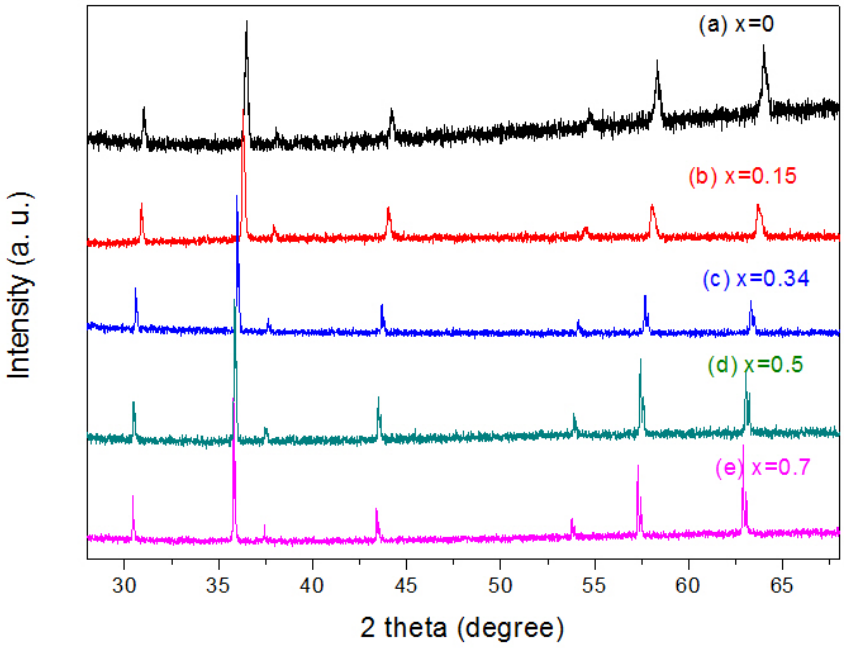

Fig. 4.1 XRD patterns of $MnCo_{2-x}Fe_xO_4$ (x= 0 - 0.7) spinel oxides at room temperature.

4.3.2 Neutron diffraction

The neutron diffraction patterns for $MnCo_{1.66}Fe_{0.34}O_4$ and $Mn_{0.67}Co_{1.22}Fe_{0.22}CrO_4$ at

600^{o}C under air atmosphere are shown in Fig. 4.2 and Fig. 4.3, respectively. The broad background spectra are due to the quartz sample holder.

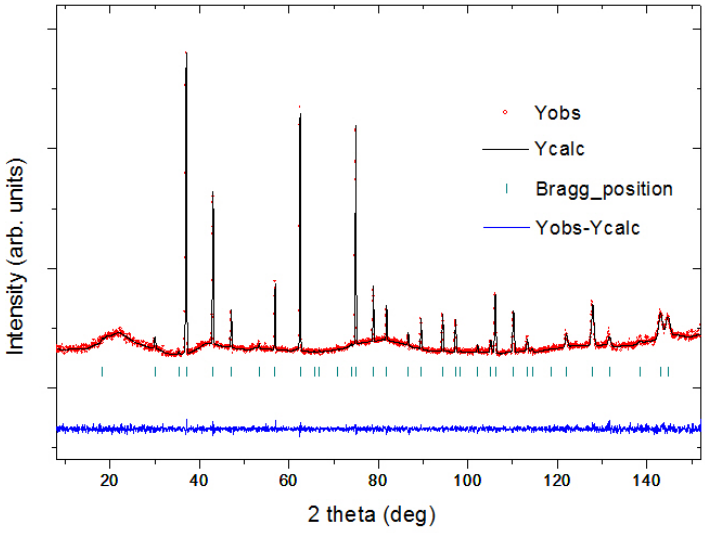

Fig. 4.2 Neutron diffraction patterns of $MnCo_{1.66}Fe_{0.34}O_4$ in air at 600 ^{o}C.

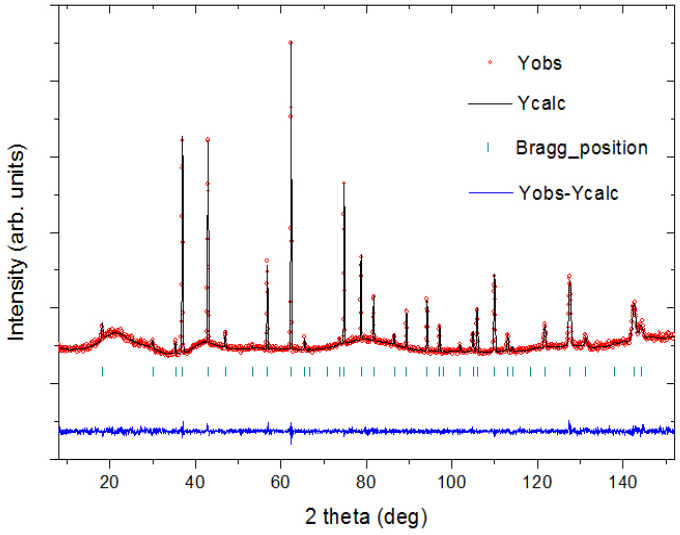

Fig. 4.3 Neutron diffraction patterns of $Mn_{0.67}Co_{1.22}Fe_{0.22}CrO_4$ at 600 ^{o}C in air.

Table 4.1 Crystal parameters of $MnCo_{1.66}Fe_{0.34}O_4$ and $Mn_{0.67}Co_{1.22}Fe_{0.22}CrO_4$ at 600 ^oC.

(a) 50% Fe on tetrahedral and octahedral sites, respectively.

	$MnCo_{1.66}Fe_{0.34}O_4$	$Mn_{0.67}Co_{1.22}Fe_{0.22}CrO_4$
Space group	$Fd\bar{3}m$	$Fd\bar{3}m$
a (A)	8.39329(12)	8.40503(9)
$[Mn]_T$	0.200(16)	0.206(9)
$[Co]_T$	0.630(16)	0.684(9)
$[Fe]_T$	0.17(0)	0.11(0)
$[Mn]_M$	0.445(5)	0.265(5)
$[Co]_M$	0.470(5)	0.180(5)
$[Fe]_M$	0.085(0)	0.055(0)
$[Cr]_M$	--	0.5(0)
R_{wp} (%)	3.71	3.57
R_{exp} (%)	3.52	3.02

(b) 70% Fe on tetrahedral and 30% Fe on octahedral sites, respectively.

	$MnCo_{1.66}Fe_{0.34}O_4$	$Mn_{0.67}Co_{1.22}Fe_{0.22}CrO_4$
Space group	$Fd\bar{3}m$	$Fd\bar{3}m$
a (A)	8.39329(12)	8.40504(9)
$[Mn]_T$	0.276(16)	0.256(9)
$[Co]_T$	0.486(16)	0.590(9)
$[Fe]_T$	0.238(0)	0.154(0)
$[Mn]_M$	0.407(5)	0.241(5)
$[Co]_M$	0.542(5)	0.226(5)
$[Fe]_M$	0.051(0)	0.033(0)
$[Cr]_M$	--	0.5(0)
R_{wp} (%)	3.70	3.56
R_{exp} (%)	3.52	3.25

(c) 30% Fe on tetrahedral and 70% Fe on octahedral sites, respectively.

	$MnCo_{1.66}Fe_{0.34}O_4$	$Mn_{0.67}Co_{1.22}Fe_{0.22}CrO_4$
Space group	$Fd\bar{3}m$	$Fd\bar{3}m$
a (A)	8.39328(12)	8.40503(9)
$[Mn]_T$	0.124(16)	0.157(9)
$[Co]_T$	0.774(16)	0.777(9)
$[Fe]_T$	0.102(0)	0.066(0)
$[Mn]_M$	0.483(5)	0.289(5)
$[Co]_M$	0.398(5)	0.134(5)
$[Fe]_M$	0.119(0)	0.077(0)
$[Cr]_M$	--	0.5(0)
R_{wp} (%)	3.70	3.57
R_{exp} (%)	3.52	3.25

For these two samples, all the cations' occupancies were first refined without any constraints, but the formula from the refinement is far away from the nominal formula. As discussed in the third chapter, for the ternary or even quaternary spinel system, neutron diffraction is difficult to determine more than two cations' distributions in the same site (octahedral and tetrahedral) directly, so constraints are required for the refinement. According to Navrotsky et al's work, both Fe^{3+} and Fe^{2+} do not have strong preference to either tetrahedral or octahedral site. [148] So it is reasonable to assume the Fe occupancy on both tetrahedral and the octahedral sites. First, half of the Fe content is assumed on tetrahedral site

and half on the octahedral site. The spectra indicate $MnCo_{1.66}Fe_{0.34}O_4$ has a single cubic phase (Space group: $Fd\bar{3}m$) at 600 °C in Fig. 4.2, which is consistent with its crystal structure at room temperature. Its refined crystallographic formula is $(Mn_{0.200}Co_{0.630}Fe_{0.17})[Mn_{0.442}Co_{0.473}Fe_{0.085}]_2O_4$, where the parentheses represent cations on tetrahedral site, and square brackets represent cations on octahedral sites. It is shown that more Mn cations prefer to occupy the octahedral sites. Then, different ratio of Fe on both sites are constrained (e.g., 70% of the Fe content on tetrahedral site and 30% on the octahedral site, 30% of the Fe content on tetrahedral site and 70% on the octahedral site). Their refined results are shown in Table 4.1 (b) and (c), respectively. In the three cases, they all have similar residuals, which may suggest the three cation distributions are possible. Because Fe cations do not have preference to tetrahedral or octahedral site, [148] it is more safely tentative to constrain half of the Fe content on tetrahedral site and half on the octahedral site in Table 4.1 (a).

For $Mn_{0.67}Co_{1.22}Fe_{0.22}CrO_4$, besides the application of above constraint on iron's distribution, the octahedral site was constrained to be fully occupied with 50% occupation by Cr^{3+} due to its strongest octahedral-site occupation.[77,122,148,154,160] $Mn_{0.67}Co_{1.22}Fe_{0.22}CrO_4$ also shows a cubic phase at 600 °C with space group $Fd\bar{3}m$ (227). The refined crystal parameters of $Mn_{0.67}Co_{1.22}Fe_{0.22}CrO_4$ with different Fe occupancy ratio assumptions are listed in Table 4.1. For the three conditions, the fitting results have similar residuals, and the occupancy of Mn in octahedral sites was higher than that in tetrahedral sites. Similar to $MnCo_{1.66}Fe_{0.34}O_4$, it is also more safe and reasonable to constrain half of the Fe content on tetrahedral site and half on the octahedral site in $Mn_{0.67}Co_{1.22}Fe_{0.22}CrO_4$.

4.3.3 Interaction with Chromia

4.3.3.1 Surface Morphology

The interactions with chromia were performed to simulate the SOFC working condition for 420 h. Fig. 4.4 (a) shows the surface of the as-prepared $MnCo_{1.5}Fe_{0.5}O_4$ pellet. The grains were densely packing with little isolated pores. After reaction with chromia at 800^oC, a dense faceted morphology was formed in the region in contact with Cr_2O_3 shown in Fig. 4.4 (b). EDS analysis indicate the chemical composition of this outer reaction scale is $Mn_{0.1}Co_{0.9}Cr_{2.0}O_4$ spinel oxide. The surface morphologies of other $MnCo_{2-x}Fe_xO_4$ (x= 0.15, 0.34 and 0.7) samples after reaction at 800^oC in contact with Cr_2O_3 for 420 h are shown in Fig. 4.5. $MnCo_{2-x}Fe_xO_4$ spinels (x= 0.15, 0.34 and 0.5) have similar faceted morphologies in the region in contact with Cr_2O_3, but the surface morphology of $MnCo_{1.3}Fe_{0.7}O_4$ after reaction is a little different, which could be related to its growth of the reaction layer.

Table 4.2 also lists the corresponding chemical composition and Co/Mn ratio of $MnCo_{2-x}Fe_xO_4$ (x= 0.15 - 0.7) after reaction at 800^oC. It is interesting to note that even Fe content is increased to 0.7 in $MnCo_{1.3}Fe_{0.7}O_4$, no iron is observed in the interface in contact with Cr_2O_3, with the composition of $Mn_{0.2}Co_{0.8}Cr_{2.0}O_4$, which suggested iron may not prefer the tetrahedral site as compared with manganese and cobalt during the interaction with Cr_2O_3. In addition, Co/Mn ratio of the outer reaction layer is decreased as that decreased in the samples before reaction, but is still much higher than that in the original $MnCo_{2-x}Fe_xO_4$ spinel oxides.

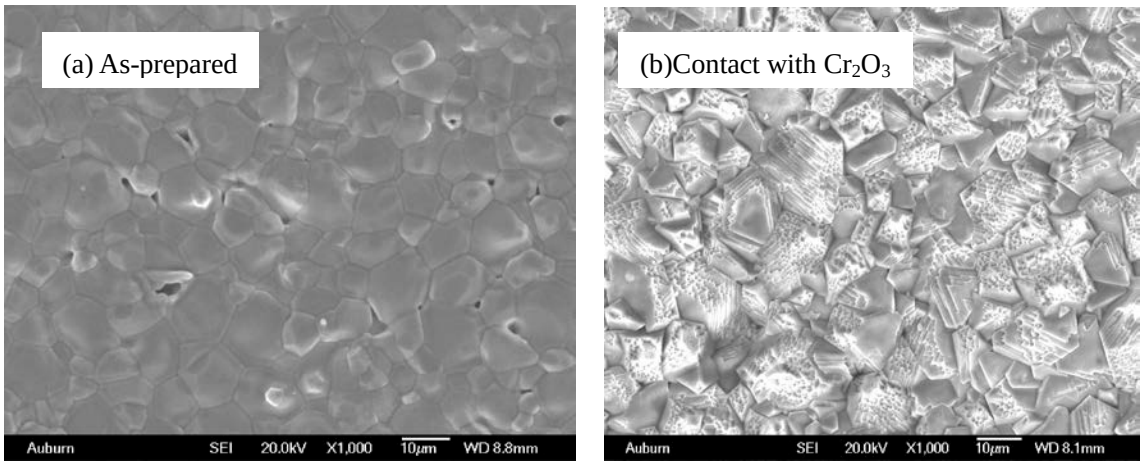

Fig. 4.4 SEM images of surface of $MnCo_{1.5}Fe_{0.5}O_4$ before (a) and after (b) reaction at 800 ^oC in contact with Cr_2O_3 for 420 h.

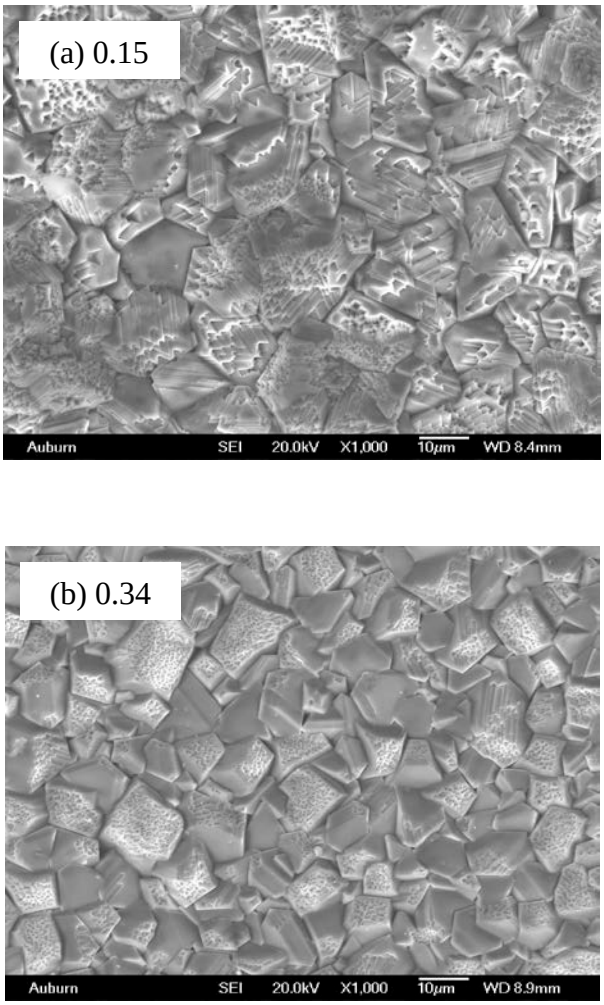

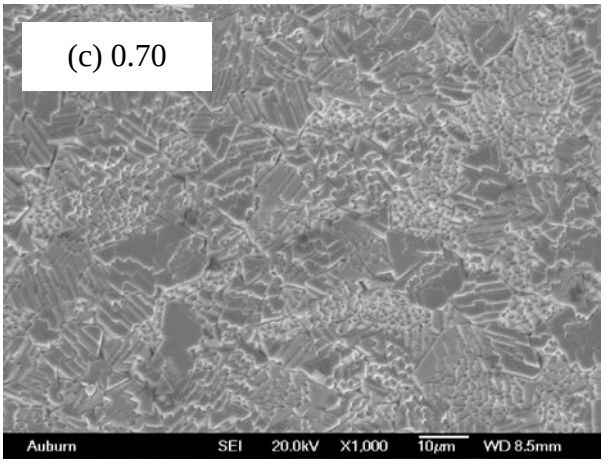

Fig. 4.5 SEM images of surface morphologies of $MnCo_{2-x}Fe_xO_4$ (x= 0.15, 0.34 and 0.7) after reaction at 800^oC in contact with Cr_2O_3 for 420 h.

Table 4.2 Chemical composition and Co/Mn ratio of $MnCo_{2-x}Fe_xO_4$ (x= 0.15 - 0.7) after reaction at 800 ^oC in contact with Cr_2O_3 for 420 h.

Chemical Composition		Co/Mn ratio	
As-prepared	After reaction	Before	After
$MnCo_{1.85}Fe_{0.15}O_4$	$Mn_{0.1}Co_{0.9}Cr_{2.0}O_4$	1.85	9
$MnCo_{1.66}Fe_{0.34}O_4$	$Mn_{0.1}Co_{0.9}Cr_{2.0}O_4$	1.66	9
$MnCo_{1.50}Fe_{0.50}O_4$	$Mn_{0.1}Co_{0.9}Cr_{2.0}O_4$	1.50	9
$MnCo_{1.30}Fe_{0.70}O_4$	$Mn_{0.2}Co_{0.8}Cr_{2.0}O_4$	1.30	4

4.3.2.2 Concentration Gradients

Fig. 4.6 shows the Cr concentration gradient of $MnCo_{2-x}Fe_xO_4$ after reaction with Cr_2O_3 at 800^oC for 420 h. The cation concentration gradients were measured at locations in different images of each sample. The Cr profile exhibited two layer forms in the reaction region, which is consistent with the earlier work in the second chapter. The outer Cr-rich spinel layer

contacted with chromia grew by diffusion of cobalt and manganese from $MnCo_{2-x}Fe_xO_4$. At the same time, chromium dissolved into $MnCo_{2-x}Fe_xO_4$ and formed the inner layer with Cr content decreased to 0. As for $MnCo_{2-x}Fe_xO_4$ samples, when the Fe content is from 0.15 to 0.5, the thickness of outer reaction layer did not change much. But for $MnCo_{1.3}Fe_{0.7}O_4$, its thickness increased. Fig. 4.7 shows the dopant (Fe) concentration gradient after high-temperature reaction. The thickness of outer reaction layer can also be reflected from Fe profile, because Fe did not appear throughout this scale in all $MnCo_{2-x}Fe_xO_4$ spinel oxides. The composition differences after reaction are probably attributed to the cation occupancy preference. In the Cr-rich outer layer, Cr^{3+} has the strongest preference for the octahedral site in the spinel structure, so during reaction Cr pushed Co and Mn to the tetrahedral site. Fig. 4.8 and Fig. 4.9 are the Co and Mn content profiles after reaction with Cr_2O_3, respectively. It was observed that the Co/Mn ratio in the outer reaction layer is much higher than that in the original $MnCo_{2-x}Fe_xO_4$ spinels, which could be due to higher diffusion rate of cobalt in the reaction layer than that of manganese or greater preference of cobalt cation for tetrahedral site than that of manganese cation which is also confirmed in the third chapter. Compared with Co and Mn, Fe seems not prefer the tetrahedral site, which may suggest why Fe was not detected in this region.

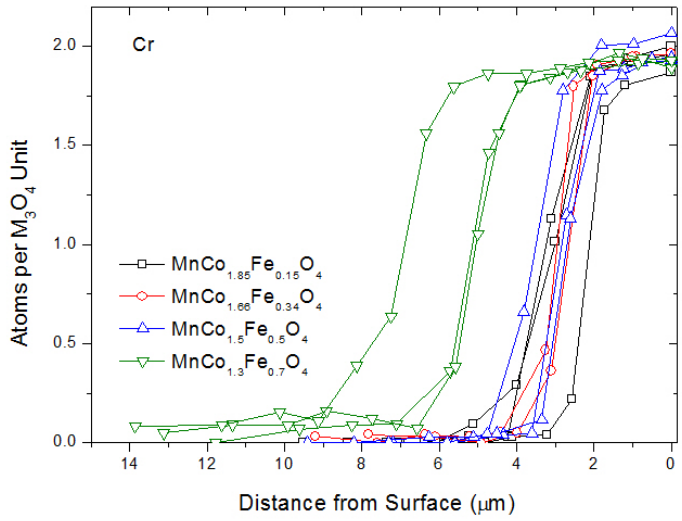

Fig. 4.6 Cr concentration profile in $MnCo_{2-x}Fe_xO_4$ after reaction for 420 h in contact with Cr_2O_3 at 800°C.

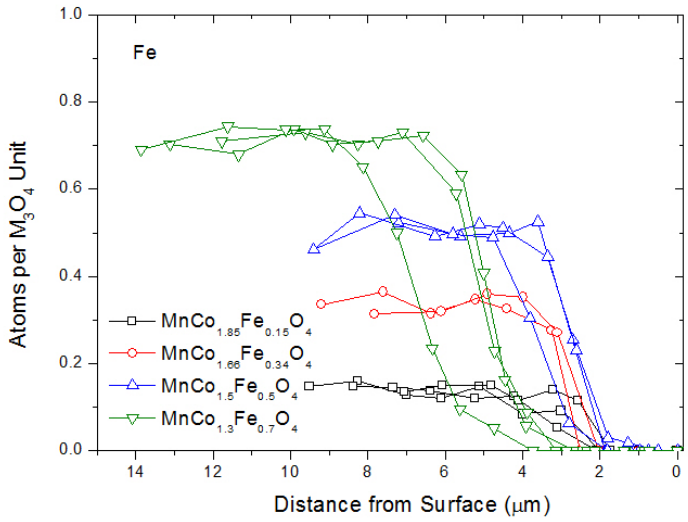

Fig. 4.7 Fe concentration profile in $MnCo_{2-x}Fe_xO_4$ after reaction for 420 h in contact with Cr_2O_3 at 800°C.

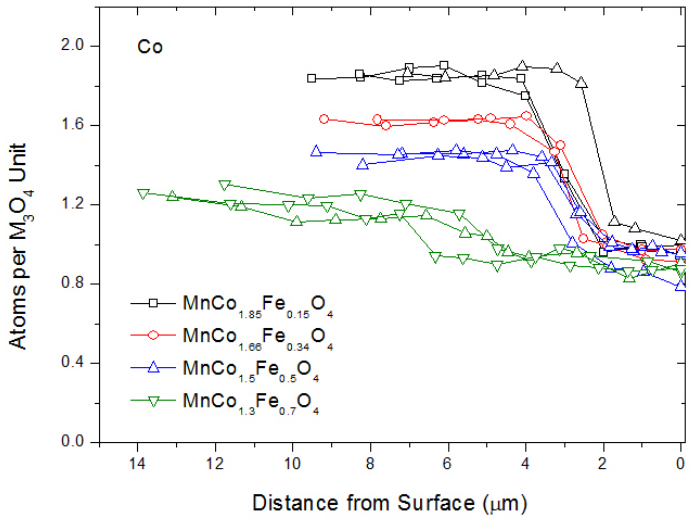

Fig. 4.8 Co concentration profile in $MnCo_{2-x}Fe_xO_4$ after reaction for 420 h in contact with Cr_2O_3 at 800°C.

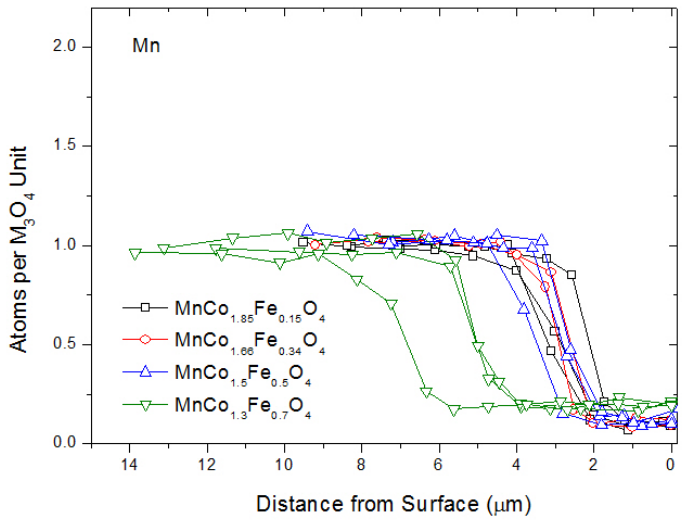

Fig. 4.9 Mn concentration profile in $MnCo_{2-x}Fe_xO_4$ after reaction for 420 h in contact with Cr_2O_3 at 800°C.

4.3.4 Electrical conductivity

The electrical conductivity is an important property for the interconnect coating. Fig. 4.10 shows the conductivity data of $MnCo_{2-x}Fe_xO_4$ at 800 ^oC in air. The conductivity increased when Fe was doped as 0.15 content. Then as Fe content was increased further, the conductivity at high temperature decreased. But still $MnCo_{1.66}Fe_{0.34}O_4$ had comparable electrical conductivity with $Mn_{1.5}Co_{1.5}O_4$, close to 60 S/cm at 800^oC in air [131]. Similar to other spinel oxides, the conductivities of $MnCo_{2-x}Fe_xO_4$ increased with temperature in a linear relationship between $\log(\sigma T)$ and 1000/T as shown in Fig. 11, and suggests their conduction belongs to the small polaron hopping mechanism. [122, 156-158] Their activation energy (E_a) was calculated from the slope of the fitting line in Fig. 4.11, and it does not vary significantly, in the range of 0.54-0.58 eV. Although the conductivity of $MnCo_{2-x}Fe_xO_4$ decreased further, it was still much higher than that of $(Mn,Co,Cr)_3O_4$, shown in Fig. 4.8. So considering both the reactivity with chromia and conductivity properties, the reasonable Fe doping content would be controlled less than 0.5.

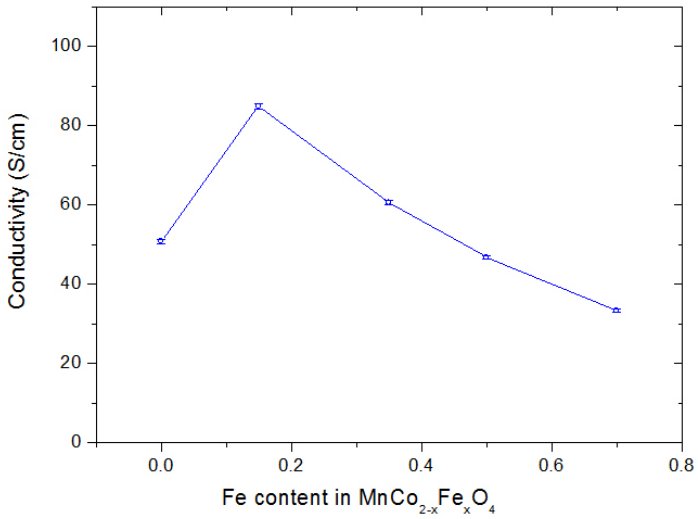

Fig. 4.10 Electrical conductivities of $MnCo_{2-x}Fe_xO_4$ at 800 ^oC in air.

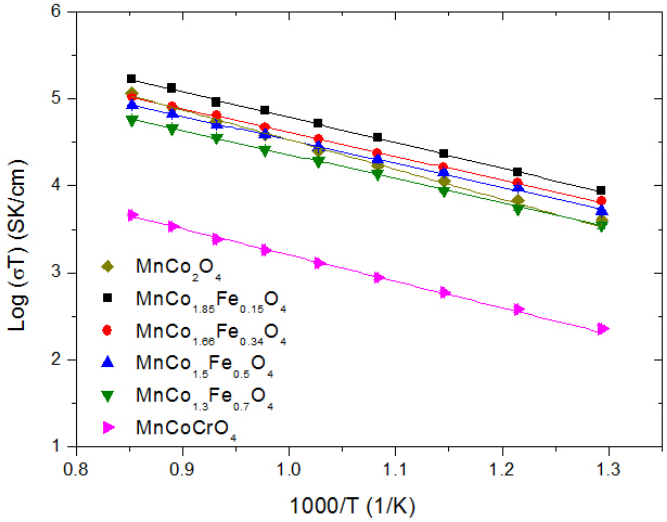

Fig. 4.11 Electrical conductivities of $MnCo_{2-x}Fe_xO_4$ and $MnCoCrO_4$ spinels as a function of temperature.

4.3.4 Comparison in the effect of Fe and Ti doping

The effect of iron and titanium doping on the reaction between the manganese cobalt

spinel oxide and Cr_2O_3 are illustrated in Fig. 4.12. [148] Similar to the results of $Mn_{1.5}Co_{1.5}O_4$, the Cr concentration profile indicated a two-layer interaction region formed between $MnCo_{1.66}TM_{0.34}O_4$ (TM=Fe and Ti) and Cr_2O_3, a Cr-rich outer layer and a Cr-containing intermediate layer. However, the thickness of the Cr-rich outer layer is reduced significantly after doping with iron and titanium. The Cr-rich layer formed in $Mn_{1.5}Co_{1.5}O_4$ was around 2 times as thick as that in $MnCo_{1.66}TM_{0.34}O_4$. The reason for the decreased extent of the reaction in $MnCo_{1.66}TM_{0.34}O_4$ is not fully understood yet, but would be related to the change in the transport properties of manganese cobalt spinel oxide doped with Fe and Ti or (octahedral/tetrahedral) site preferences. Even for the $MnCo_{1.66}Ti_{0.34}O_4$ oxide, its Co/Mn ratio at the interface after reaction was still higher than that in the original spinel, which is consistent with Fe doped or un-doped manganese cobalt spinel oxides. Fig. 4.13 shows Fe and Ti concentration profile in $MnCo_{1.66}TM_{0.34}O_4$ after reaction in contact with Cr_2O_3 for 72 h at 1000 ^oC. [148] It should be noted that similar to Fe, no Ti was detected by EDS in the Cr-rich layer, which could be attributed to the site (octahedral/tetrahedral) preferences. Ti is reported to prefer the octahedral sites in the spinel oxides.[147] So during the formation of the Cr-rich outer layer, when Cr^{3+} occupies the octahedral site, Ti cations would not be as competent as Mn^{2+} and Co^{2+} for the occupation in tetrahedral site.

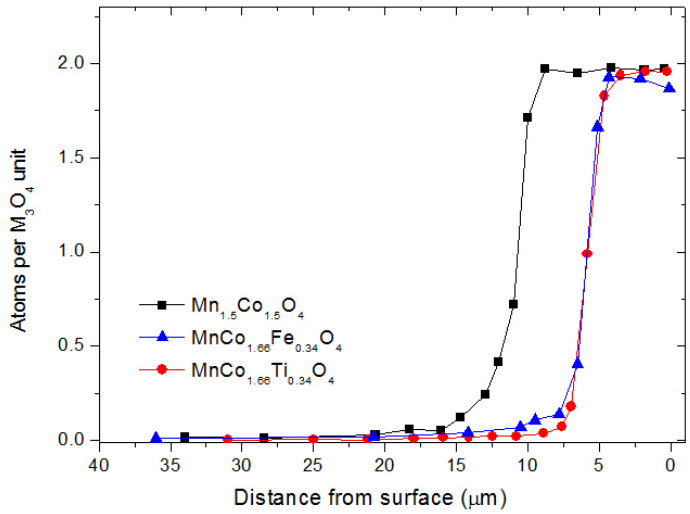

Fig. 4.12 Chromium concentration profile in $MnCo_{1.66}TM_{0.34}O_4$ (TM=Fe and Ti) and $Mn_{1.5}Co_{1.5}O_4$ after reaction in contact with Cr_2O_3 for 72 h at 1000°C.[148]

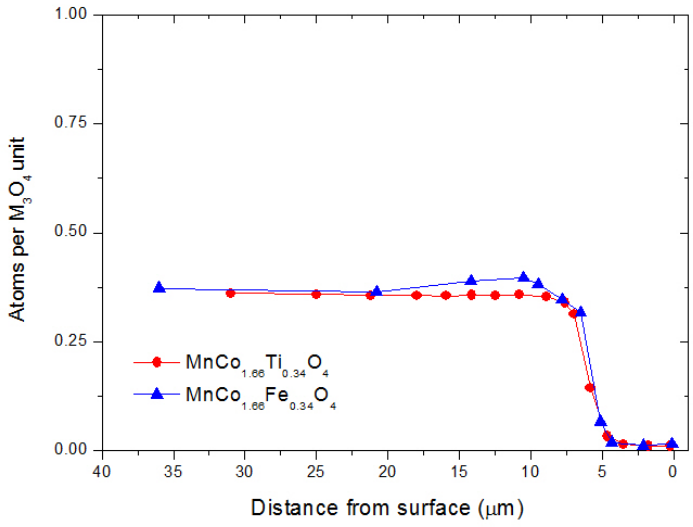

Fig. 4.13 Dopant (Fe and Ti) concentration profile in $MnCo_{1.66}TM_{0.34}O_4$ (TM=Fe and Ti) after reaction in contact with Cr_2O_3 for 72 h at 1000°C. [148]

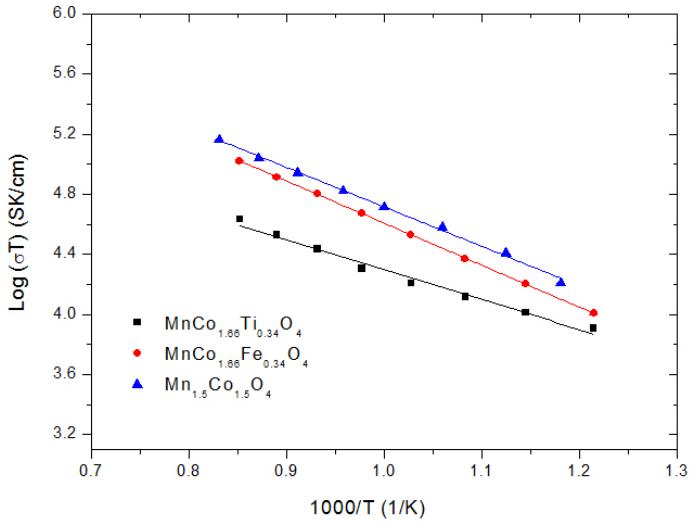

Fig. 4.14 Comparison in electrical conductivities of $MnCo_{1.66}TM_{0.34}O_4$ (TM=Fe and Ti) spinel oxides.

The electrical conductivities of $MnCo_{1.66}TM_{0.34}O_4$ (TM=Fe and Ti) spinel oxides as a function of temperature are plotted in Fig. 4.14. It is shown that the electrical conductivity of $MnCo_{1.66}Ti_{0.34}O_4$, about 25 S/cm at 800°C, is lower than that of $MnCo_{1.66}Fe_{0.34}O_4$ in air.

Table 4.3 lists the CTE values of $MnCo_{1.66}TM_{0.34}O_4$ (TM=Fe and Ti) and $(Mn,Co)_3O_4$ spinels.[149] $MnCo_2O_4$ had a much higher CTE than most of the stainless steels interconnect (11.5-14 $x10^{-6}/\,^oC$), and mismatch in thermal expansion may result in local spallation and crack. After substitution with iron and titanium, CTEs were reduced to compatible values, about 11.2×10^{-6}/°C for $MnCo_{1.66}Ti_{0.34}O_4$ and 12.0×10^{-6}/°C for $MnCo_{1.66}Fe_{0.34}O_4$. Higher cobalt can lead to a higher CTE, but both Fe and Ti can adjust CTE value of manganese cobalt spinel oxide to match that of stainless steels interconnect.

Table 4.3 CTEs of $MnCo_{1.66}TM_{0.34}O_4$ (TM=Fe and Ti) and $(Mn,Co)_3O_4$ spinel oxides.[149]

Composition	CTE (room temperature-1000°C, $x10^{-6}/°C$) in air
$Mn_{1.5}Co_{1.5}O_4$	10.8
$MnCo_2O_4$	14.1
$MnCo_{1.66}Fe_{0.34}O_4$	12.0
$MnCo_{1.66}Ti_{0.34}O_4$	11.2

4.4 Conclusions

$MnCo_{2-x}TM_xO_4$ (TM = Fe, x = 0-0.7) spinel oxides were synthesized to investigate the effects of Fe doping on the reaction with chromia and electrical property at high temperature. When Fe was doped up to 0.5, the thickness of the reaction layer did not increase. Although Fe dopant is increased to 0.7, it did not appear in the Cr-rich reaction layer, which would be related to that Fe may not prefer the tetrahedral site as Co and Mn cations during the reaction. As Fe content increased from x = 0.15, the conductivity decreased, but is still high enough. The electrical conductivity of $MnCo_{1.66}Fe_{0.34}O_4$ at 800°C was quite close to that of $Mn_{1.5}Co_{1.5}O_4$, the most promising coating candidate.

The comparison between iron and titanium doping on the performance of $MnCo_{1.66}TM_{0.34}O_4$ (TM=Fe and Ti) coatings was also performed. With the substitution of iron and titanium, the thicknesses of reaction layer formed between $MnCo_{1.66}TM_{0.34}O_4$ and Cr_2O_3 were obviously reduced as compared with $Mn_{1.5}Co_{1.5}O_4$, which could improve the adherence of the coating on the alloy and the long-term stability of the SOFC interconnect. The thermal expansion was also well adjusted after doping with Fe or Ti. But neither Fe nor

Ti were detected in the outer reaction layer. The reason for the decreased growth in the reaction layer after doping with Fe and Ti is not clear yet, but could be related to the change in the transport properties of $MnCo_{1.66}TM_{0.34}O_4$ and/or site (octahedral/tetrahedral) preferences in the spinel. The electrical conductivity of $MnCo_{1.66}Ti_{0.34}O_4$ is lower than that of $MnCo_{1.66}Fe_{0.34}O_4$, but still high enough for the spinel coating. Based on the high temperature properties (conductivity and reaction with Cr_2O_3), $MnCo_{2-x}Fe_xO_4$ with iron content lower than 0.5 would be the potential composition as SOFC interconnect coating.

CHAPTER 5

Interaction of transition metal-doped $(Mn,Co)_3O_4$ (TM = Ni, Cu) spinels with chromia for SOFC interconnect coatings

5.1 Introduction

Manganese cobalt spinel oxides $(Mn,Co)_3O_4$ are promising coating candidates which can be applied on SOFC metallic interconnect ferritic stainless steels. As discussed in the forth chapter, doping iron and titanium in $(Mn,Co)_3O_4$ can depress the thickness and growth of the outer reaction layer in $(Mn,Co)_3O_4$, and the Cr concentrate gradient in the intermediate layer became steep. However no iron and titanium dopants were detected in the Cr-rich spinel area, which could be related to the cation site preference in spinel structure. It was reported that chromite spinel oxides (ACr_2O_4) are normal spinel structure, in which Cr^{3+} occupy all the octahedral holes, and A-site cations occupy the tetrahedral holes.[77,122,154,160] Since titanium has large octahedral site preference, but not as strong as chromium in the spinel oxide, it would explain why in the interaction with chroma, titanium cation is reluctant to occupy the octahedral sites in the Cr-rich reaction layer. Ni^{2+} also exhibits high preference in octahedral sites in many spinel oxides.[148,161,162] Then the effect of Ni doping in $Mn_{1.5}Co_{1.5}O_4$ on the reaction behavior with chromia is studied here. Wei et al reported copper has a much greater tendency to occupy the tetrahedral sites in $Cu_xMn_{3-x}O_4$ spinel oxides.[95] So copper is also

considered as a dopant as compared with nickel. In this work, the interaction with chromia of transition metal (TM)-doped $(Mn,Co)_3O_4$ (TM = Ni, Cu) at high temperature were investigated as potential SOFC interconnect coatings.

5.2 Experimental

(TM)-doped $(Mn,Co)_3O_4$ (TM = Ni, Cu) spinel oxides spinel oxides were synthesized by solid state reaction. MnO (99% pure, Alfa Aesar, Ward Hill, MA), Co_3O_4 (99.83% pure, Fisher, Pittsburgh, PA) and NiO (99% pure, Alfa Aesar, Ward Hill, MA) or CuO (99% pure, Alfa Aesar, Ward Hill, MA) were weighed in appropriate ratio to form the desired stoichiometry. Then the powder mixtures were ball-milled for 48 h with zirconia milling medium in de-ionized water, and the slurry was dried overnight in an oven. The pre-mixed powders were die-pressed, and then sintered at 1200^oC in air.

The interaction between the prepared TM-doped $(Mn,Co)_3O_4$ (TM = Ni, Cu) pellets and Cr_2O_3 was performed by placing the pellets in contact, and heating in air at high temperature using the sample configurations in Fig. 2.1 (a). After reaction, the microstructure and composition of samples on the surface and cross sections were characterized using a JEOL JSM-7000F scanning electron microscope (SEM) equipped with energy-dispersive X-ray (EDS). The cation concentration gradients were measured at locations in different images of each sample. The electrical conductivity was measured by four-probe d.c. method on rectangular bars with the dimension about 14 mm x 5 mm x 2 mm which were cut from sintered specimens. The measurements were conducted between 500^oC and 900^oC in random order leaving 10 h to reach equilibration. Pt paste and wire were used as current collector and

electrodes. A current chosen from 300mA -500mA was applied during measurement.

5.3 Results and discussion

5.3.1 Mass transport in $Mn_{1.5-0.5x}Co_{1.5-0.5x}TM_xO_4$ (TM=Ni,Cu)

The interactions with chromia were performed to simulate the SOFC working condition. Fig. 5.1(a) shows the surface of the as-prepared $Mn_{1.3}Co_{1.3}Ni_{0.4}O_4$ pellet. The pellet was sintered dense with close packing grains and little isolated pores. After reaction with Cr_2O_3 at 800^{o}C, similar to undoped $(Mn,Co)_3O_4$ samples investigated in the second chapter, a dense faceted morphology was formed in the region in contact with Cr_2O_3 as shown in Fig. 5.2 (b). EDS analysis indicate the chemical composition of this outer reaction scale is $Mn_{0.25}Co_{0.89}Cr_{1.86}O_4$ spinel oxide. The surface morphologies of the other $Mn_{1.5-0.5x}Co_{1.5-0.5x}TM_xO_4$ (TM=Ni, x=0.2, 0.6, TM=Cu, x=0.2, 0.4) spinel samples after reaction in contact with Cr_2O_3 at 800^{o}C for 96 h are shown in Fig. 5.2. They all have faceted morphologies in the region in contact with Cr_2O_3 after reaction, which indicated the growth mechanism of their reaction layer could be the same as the $(Mn,Co)_3O_4$ spinel oxides .

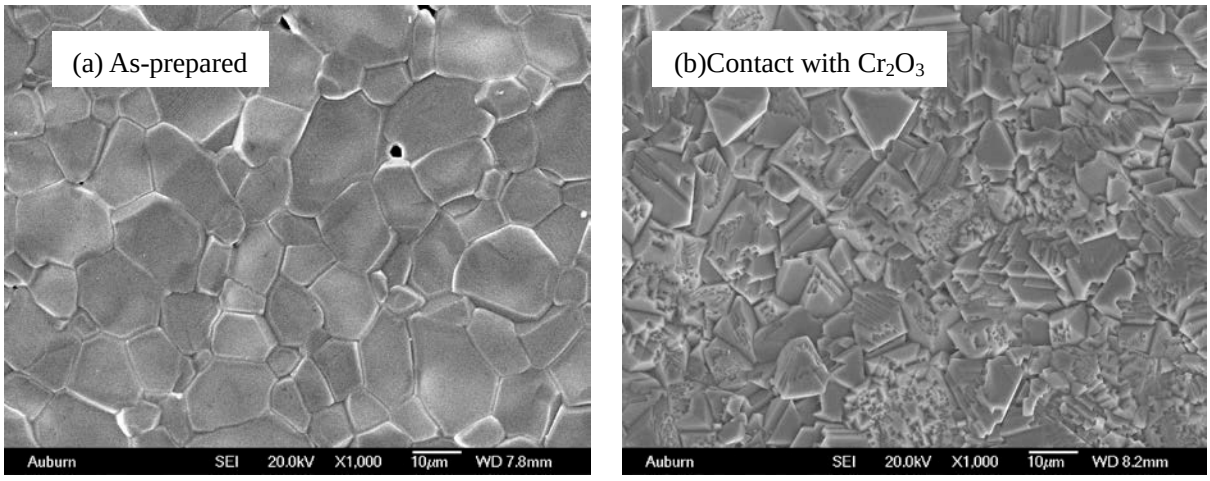

Fig. 5.1 SEM images of surface of $Mn_{1.3}Co_{1.3}Ni_{0.4}O_4$ before (a) and after (b) reaction at 800^{o}C in contact with Cr_2O_3 for 96 h.

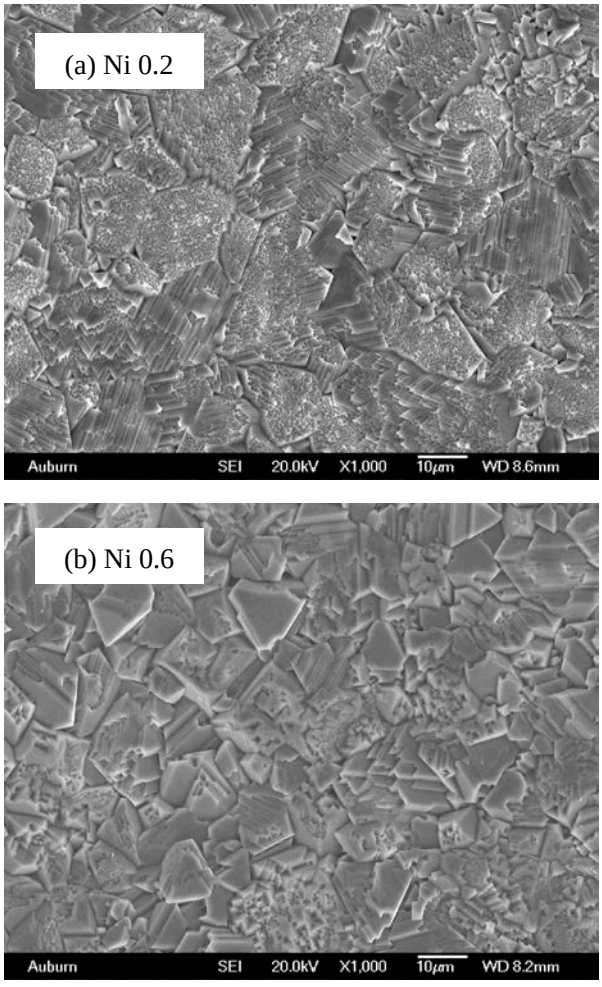

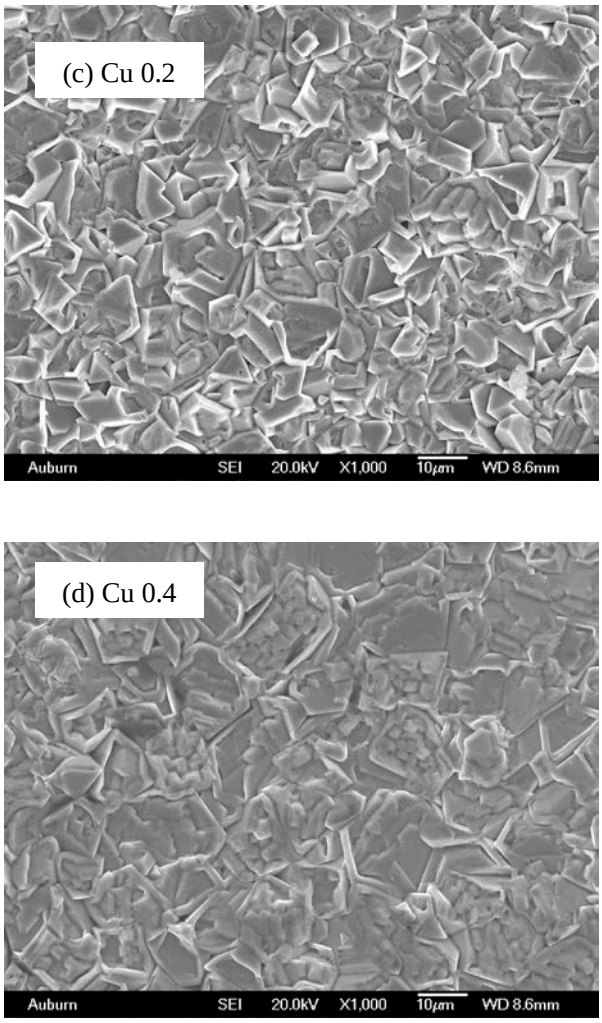

Fig. 5.2 SEM images of surface of $Mn_{1.5-0.5x}Co_{1.5-0.5x}TM_xO_4$ (TM=Ni, x=0.2, 0.6, TM=Cu, x=0.2, 0.4) after reaction at 800^{o}C in contact with Cr_2O_3 for 96 h.

Table 5.1 also lists the chemical compositions of the interface of $Mn_{1.5-0.5x}Co_{1.5-0.5x}TM_xO_4$ (TM=Ni, x=0.2-0.6, TM=Cu, x=0.2, 0.4) in contact with Cr_2O_3 after reaction at 800^{o}C for 96 h. Similar to the iron and titanium, even nickel content is increased up to 0.6 in $Mn_{1.2}Co_{1.2}Ni_{0.6}O_4$, no nickel is observed in the interface in contact with Cr_2O_3, with the composition of $Mn_{0.21}Co_{0.92}Cr_{1.87}O_4$, which would also suggest nickel may not prefer to occupy the tetrahedral site as compared with manganese and cobalt during the interaction with Cr_2O_3. However, unlike previous dopants, copper appeared in the outer Cr-rich reaction

layer, and its content increased as increasing in the $Mn_{1.5-0.5x}Co_{1.5-0.5x}Cu_xO_4$ samples, which showed copper had a significant different behavior in the mass transport, and indicated it tends to occupy the tetrahedral site in the interaction with Cr_2O_3. Besides, the Co/Mn ratio in the outer reaction layer is still much higher than that in the original $Mn_{1.5-0.5x}Co_{1.5-0.5x}TM_xO_4$ spinel oxides. It did not change much when the nickel contact increased, but decreased a little in $Mn_{1.5-0.5x}Co_{1.5-0.5x}Cu_xO_4$ as copper concentration increased in the outer reaction layer.

Table 5.1 Chemical compositions of $Mn_{1.5-0.5x}Co_{1.5-0.5x}TM_xO_4$ (TM=Ni, x=0.2-0.6, TM=Cu, x=0.2, 0.4) before and after reaction at 800 ^oC in contact with Cr_2O_3 for 96 h.

Chemical Composition	
As-prepared	After reaction
$Mn_{1.4}Co_{1.4}Ni_{0.2}O_4$	$Mn_{0.2}Co_{0.9}Cr_{1.9}O_4$
$Mn_{1.3}Co_{1.3}Ni_{0.4}O_4$	$Mn_{0.2}Co_{0.9}Cr_{1.9}O_4$
$Mn_{1.2}Co_{1.2}Ni_{0.6}O_4$	$Mn_{0.2}Co_{0.9}Cr_{1.9}O_4$
$Mn_{1.4}Co_{1.4}Cu_{0.2}O_4$	$Mn_{0.2}Co_{0.7}Cu_{0.2}Cr_{1.9}O_4$
$Mn_{1.3}Co_{1.3}Cu_{0.4}O_4$	$Mn_{0.1}Co_{0.5}Cu_{0.5}Cr_{1.9}O_4$

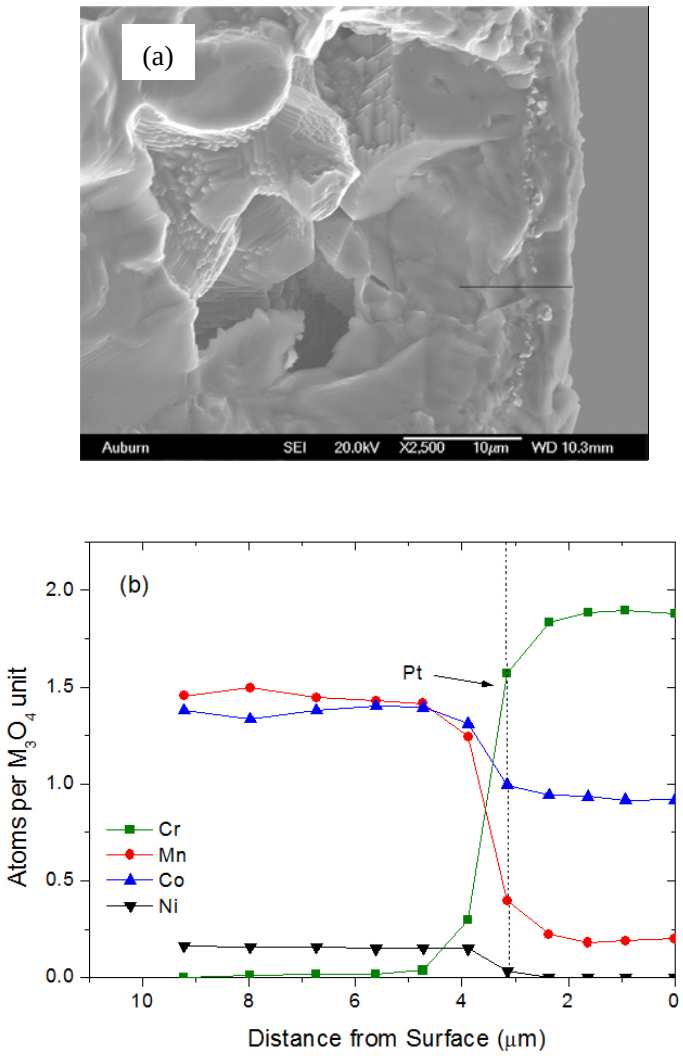

Fig. 5.3 (a) SEM image of cross section of $Mn_{1.4}Co_{1.4}Ni_{0.2}O_4$ in contact with Cr_2O_3 after reaction at 800^{o}C for 96 h and (b) its corresponding cations concentration profile.

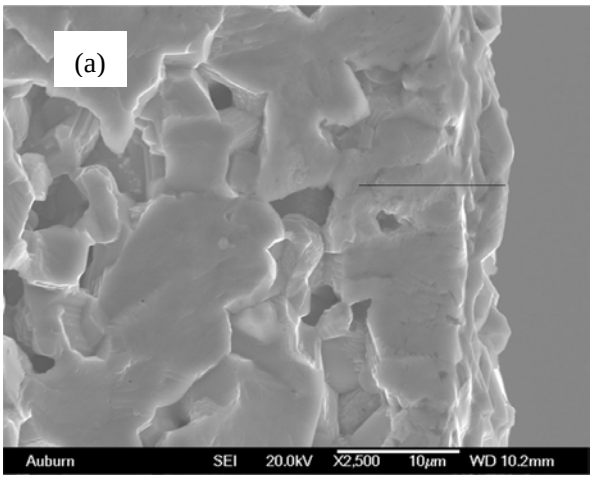

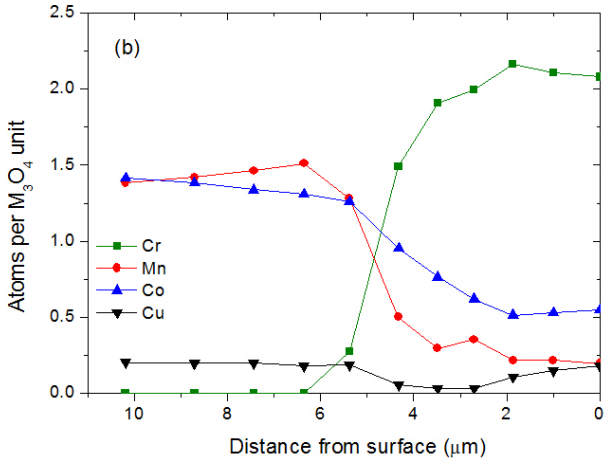

Fig. 5.4 (a) SEM image of cross section of $Mn_{1.4}Co_{1.4}Cu_{0.2}O_4$ in contact with Cr_2O_3 after reaction at 800°C for 96 h and (b) its corresponding cations concentration profile.

Fig. 5.3 shows (a) the SEM image of cross section of $Mn_{1.4}Co_{1.4}Ni_{0.2}O_4$ in contact with Cr_2O_3 after reaction at 800°C for 96 h and (b) its corresponding cations concentration profile. The lighter spots in a line in Fig. 5.3(a) are platinum makers which locates the original surface before reaction. Their current location indicates the growth mechanism of the reaction layer in $Mn_{1.4}Co_{1.4}Ni_{0.2}O_4$ is the same as that of $(Mn,Co)_3O_4$ spinel oxides investigated before. Chromium content profile in Fig. 5.3(b) also exhibited two layer contained in the reaction region. The outer Cr-rich spinel layer contacted with chromia grew by diffusion of cobalt and manganese from $Mn_{1.4}Co_{1.4}Ni_{0.2}O_4$. At the same time, chromium dissolved into $Mn_{1.4}Co_{1.4}Ni_{0.2}O_4$ and formed the inner layer with Cr content decreased to 0. Fig. 5.4 shows (a) the cross section of $Mn_{1.4}Co_{1.4}Cu_{0.2}O_4$ in contact with Cr_2O_3 (b) its corresponding cations concentration profile after reaction at 800°C for the same condition for comparison. Its morphology of the cross section is similar to that of $Mn_{1.4}Co_{1.4}Ni_{0.2}O_4$. Cr content profile in Fig. 5.4(b) also showed two-scale reaction layer, and Co/Mn ratio was much higher than 1,

the original in the sample, which could be due to higher diffusion rate of cobalt in the reaction layer than that of manganese or higher preference of cobalt cation for tetrahedral site than that of manganese cation which is also determined in the third chapter. However, it should be noted that copper appeared in the reaction layer, and its content was comparable to that in the $Mn_{1.4}Co_{1.4}Cu_{0.2}O_4$ spinel oxide, which was observed in the sample $Mn_{1.3}Co_{1.3}Cu_{0.4}O_4$ after reaction too. Copper showed a quite different behavior in the mass transport from any transition metals dopant which had been studied in this work. As discussed before, the composition differences after reaction are probably related to the preference for the cation occupancy. In the Cr-rich outer layer, Cr^{3+} still has the strongest preference for the octahedral site in the spinel structure, so during reaction Cr pushed Co, Mn and Cu to the tetrahedral site. The observation of copper in the Cr-rich reaction layer would indicate that Cu prefer the tetrahedral site to the octahedral site, which is consistent with Wei et al's results.[95]

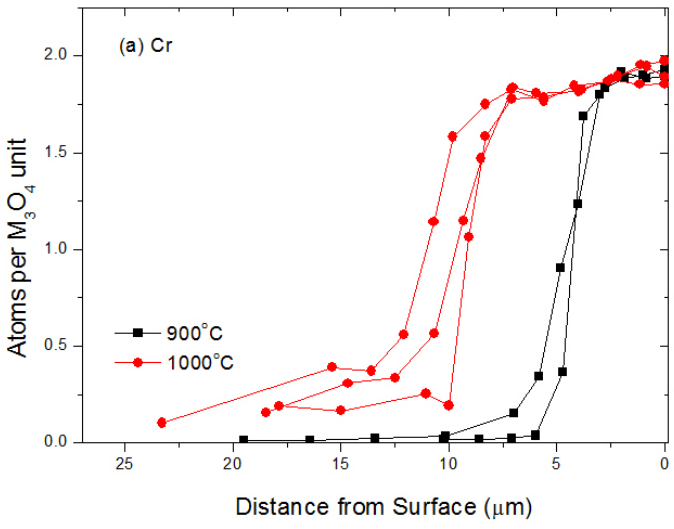

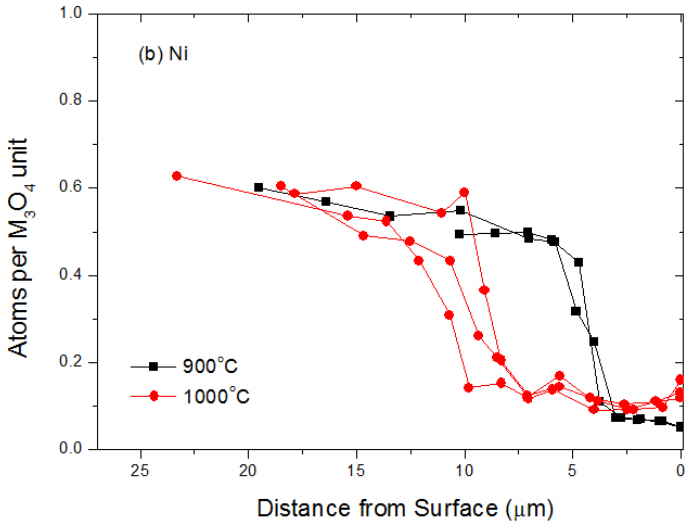

Fig. 5.5 (a) chromium and (b) nickel concentration profiles of $Mn_{1.2}Co_{1.2}Ni_{0.6}O_4$ in contact with Cr_2O_3 after reaction at 900 ^oC and 1000 ^oC for 72 h.

Fig. 5.5 shows the (a) chromium and (b) nickel concentration profiles of $Mn_{1.2}Co_{1.2}Ni_{0.6}O_4$ in contact with Cr_2O_3 after reaction at 900 ^oC and 1000 ^oC for 72 h. The dash line in Fig. 5.5(a) indicates the location of the platinum makers, where the original surface is before reaction. The thickness of Cr-rich outer reaction layer in $Mn_{1.2}Co_{1.2}Ni_{0.6}O_4$ increases significantly as the reaction temperature. Different from the interaction at 800^oC, Ni is observed to diffuse into the Cr-rich layer in Fig. 5.5(b), and its concentration in this region increases with the temperature, which may suggest enhancing reaction temperature can promote Ni diffusion into the reaction layer.

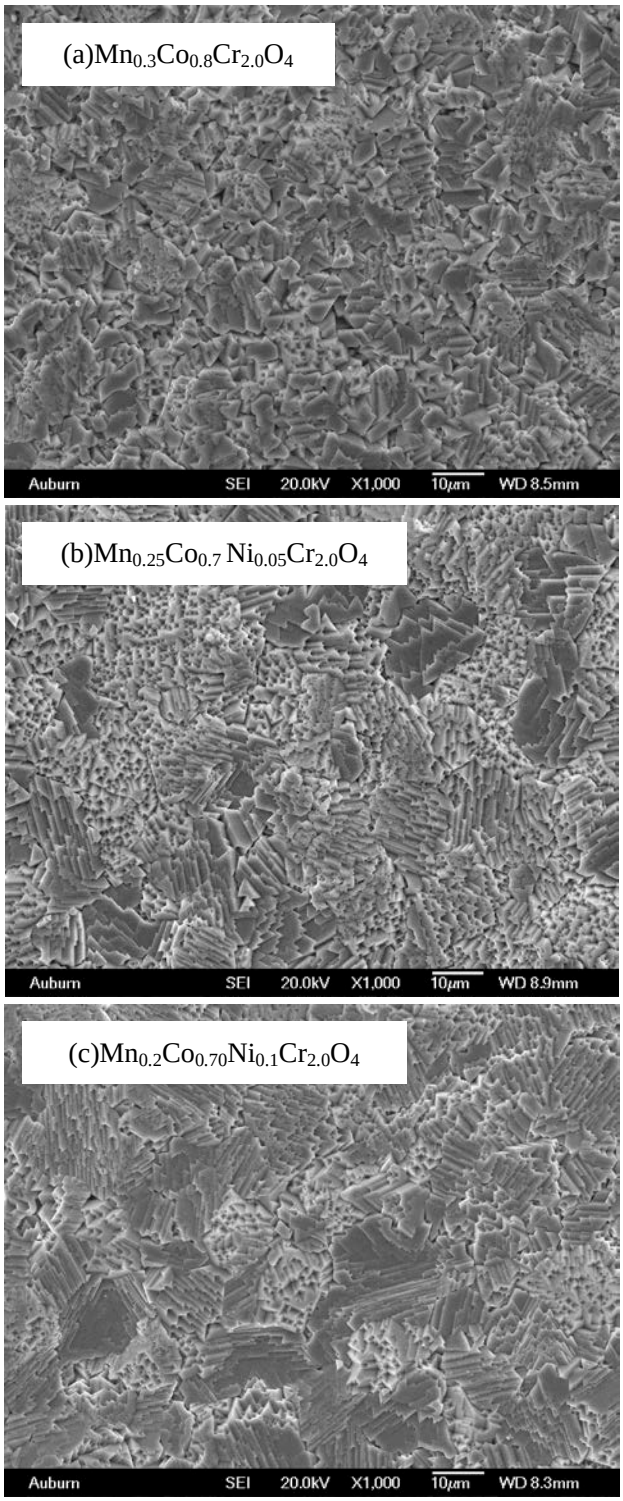

Fig. 5.6 Surface morphologies and corresponding chemical compositions of (a) $Mn_{1.4}Co_{1.4}Ni_{0.2}O_4$, (b) $Mn_{1.3}Co_{1.3}Ni_{0.4}O_4$, and (c) $Mn_{1.2}Co_{1.2}Ni_{0.6}O_4$ after reaction at 1000^oC in contact with Cr_2O_3 for 72 h.

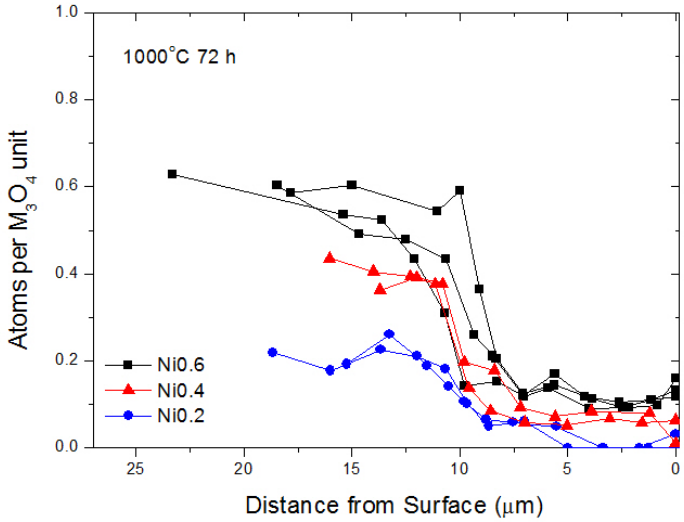

Fig. 5.7 Nickel concentration profiles of $Mn_{1.5-0.5x}Co_{1.5-0.5x}Ni_xO_4$ (x = 0.2 - 0.6) in contact with Cr_2O_3 after reaction at 1000 °C for 72 h.

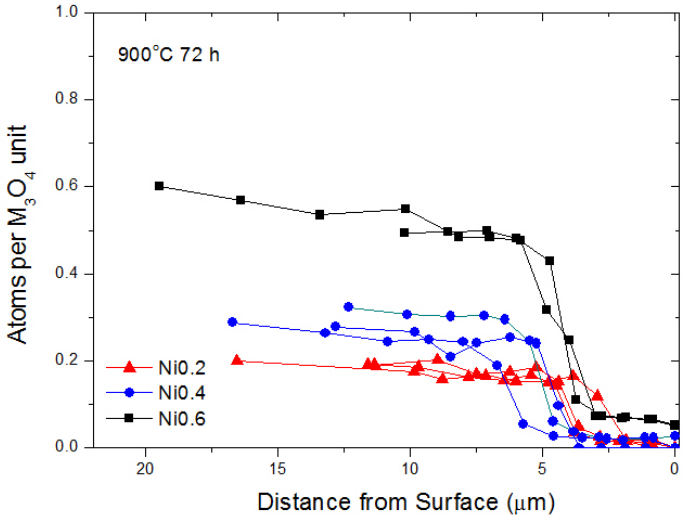

Fig. 5.8 Nickel concentration profiles of $Mn_{1.5-0.5x}Co_{1.5-0.5x}Ni_xO_4$ (x = 0.2 - 0.6) in contact with Cr_2O_3 after reaction at 900 °C for 72 h.

Fig. 5.6 are surface morphologies and corresponding chemical compositions of $Mn_{1.5-0.5x}Co_{1.5-0.5x}Ni_xO_4$ (x = 0.2 - 0.6) after reaction at 1000^oC in contact with Cr_2O_3 for 72 h, and Fig. 5.7 shows their nickel concentration profiles in contact with Cr_2O_3. Ni is detected in the outer reaction layer, and its content is shown to increase with the original Ni content in $Mn_{1.5-0.5x}Co_{1.5-0.5x}Ni_xO_4$ after reaction at 1000 ^oC. Similar results are also observed after reaction at 900 ^oC for 72 h in Fig. 5.8, which is different from the reaction behavior at 800^oC.

5.3.2 Effect of Co/Ni ratio

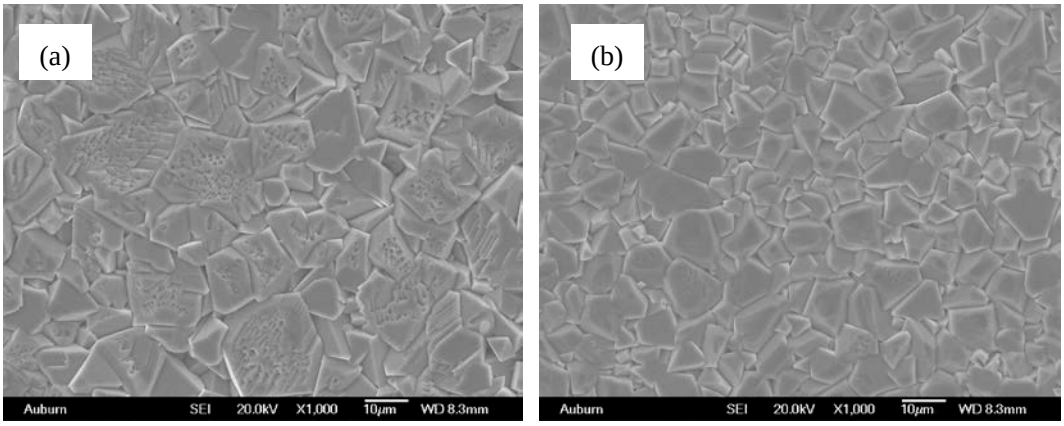

Fig. 5.9 Surface morphologies of (a) $Mn_{1.5}Co_{0.9}Ni_{0.6}O_4$ and (b) $Mn_{1.5}Co_{0.6}Ni_{0.9}O_4$ after reaction at 900^oC in contact with Cr_2O_3 for 144 h.

Fig. 5.9 are surface morphologies of (a) $Mn_{1.5}Co_{0.9}Ni_{0.6}O_4$ and (b) $Mn_{1.5}Co_{0.6}Ni_{0.9}O_4$ after reaction at 900 ^oC in contact with Cr_2O_3 for 144 h. The EDS analyses show their chemical compositions are $Mn_{0.38}Co_{0.62}Ni_{0.06}Cr_{1.94}O_4$, and $Mn_{0.53}Co_{0.36}Ni_{0.16}Cr_{1.95}O_4$, respectively. Fig. 5.10 shows their Ni concentration profiles in contact with Cr_2O_3 at the same reaction condition. The Co/Ni ratio is observed to have effect on the composition of both the

reaction interface and outer layer. Similar to the mass transport behavior of $Mn_{1.5-0.5x}Co_{1.5-0.5x}Ni_xO_4$ (x = 0.2 - 0.6) at high temperature (e.g. 1000 ^oC), Ni cations diffuse outward into the Cr-rich reaction layer, and its content is increased with the Ni content in the original spinel oxide. Fig. 5.11 shows Cr concentration profiles of $Mn_{1.5}Co_{0.9}Ni_{0.6}O_4$, $Mn_{1.5}Co_{0.6}Ni_{0.9}O_4$ and $Mn_{1.5}Co_{1.5}O_4$[148] after reaction at 900 ^oC in contact with Cr_2O_3 for 144 h. As compared with $Mn_{1.5}Co_{1.5}O_4$, their thicknesses of the Cr-rich layer are similar. For $Mn_{1.5}CoNi_{0.5}O_4$, its thickness of the Cr-rich layer is almost the same as that of $Mn_{1.5}Co_{1.5}O_4$ after reaction at 700 ^oC as long as 30 days, which is shown in Fig. 5.12. All these results could indicate the Co/Ni ratio in the spinel oxides may not affect the growth of the reaction layer.

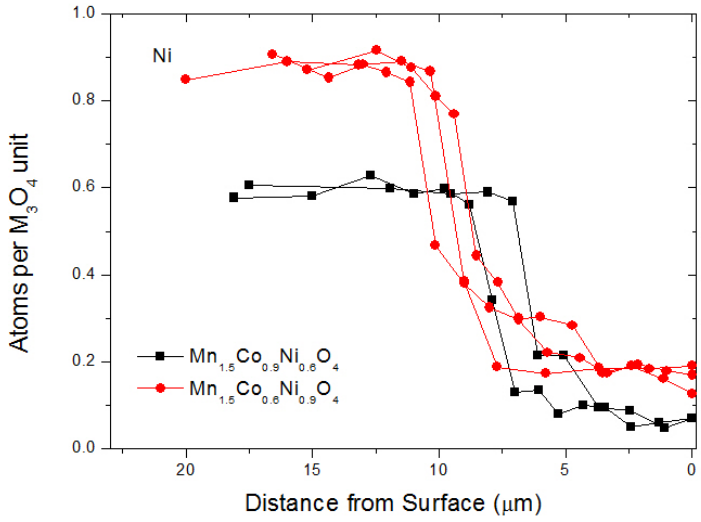

Fig. 5.10 Ni concentration profiles of $Mn_{1.5}Co_{0.9}Ni_{0.6}O_4$ and $Mn_{1.5}Co_{0.6}Ni_{0.9}O_4$ after reaction at 900^oC in contact with Cr_2O_3 for 144 h.

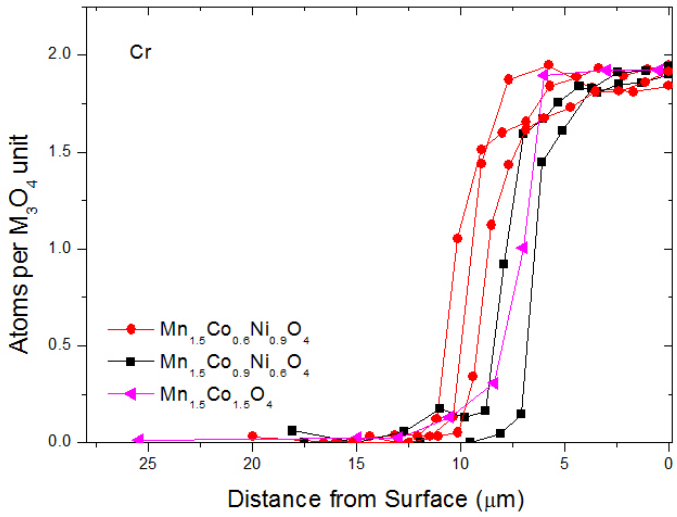

Fig. 5.11 Cr concentration profiles of $Mn_{1.5}Co_{0.9}Ni_{0.6}O_4$, $Mn_{1.5}Co_{0.6}Ni_{0.9}O_4$ and $Mn_{1.5}Co_{1.5}O_4$[148] after reaction at 900°C in contact with Cr_2O_3 for 144 h.

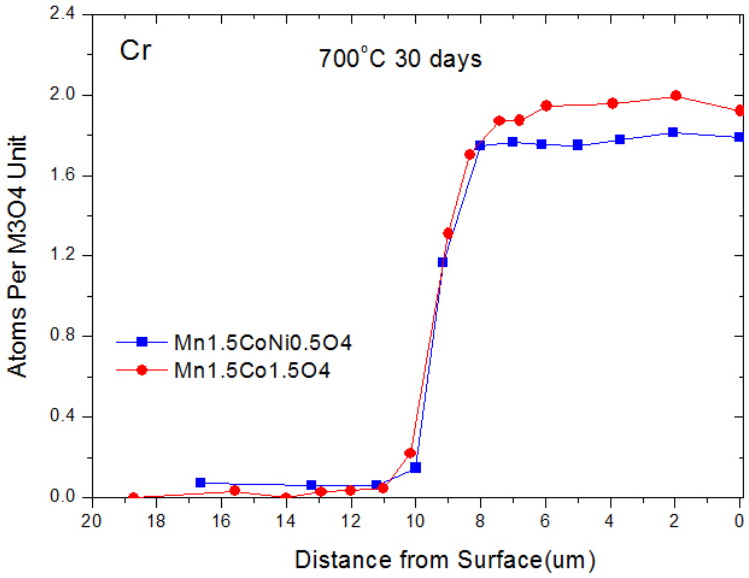

Fig. 5.12 Cr concentration profiles of $Mn_{1.5}CoNi_{0.5}O_4$ and $Mn_{1.5}Co_{1.5}O_4$ after reaction at 700°C in contact with Cr_2O_3 for 30 days.

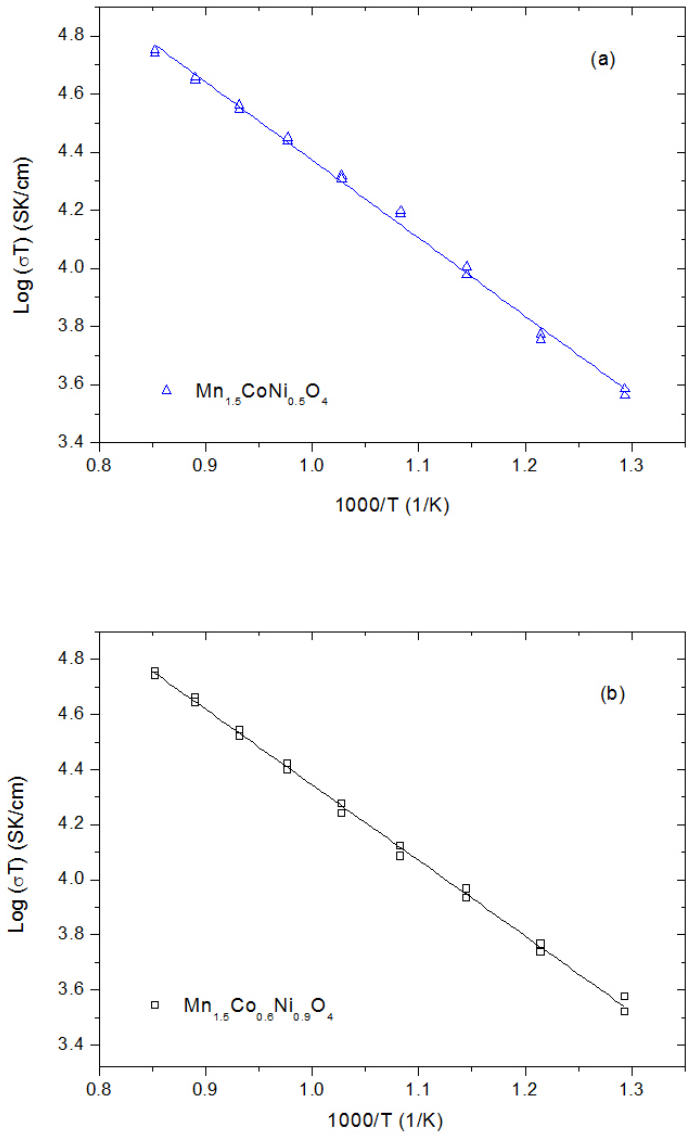

Fig. 5.13 Electrical conductivities of (a) $Mn_{1.5}CoNi_{0.5}O_4$, and (b) $Mn_{1.5}Co_{0.6}Ni_{0.9}O_4$ spinels as a function of temperature.

The electrical conductivities of $Mn_{1.5}CoNi_{0.5}O_4$ and $Mn_{1.5}Co_{0.6}Ni_{0.9}O_4$ spinel oxides as a function of temperature are shown in Fig. 5.12, respectively. Similar to other spinel oxides, the conductivities of $Mn_{1.5}CoNi_{0.5}O_4$ and $Mn_{1.5}Co_{0.6}Ni_{0.9}O_4$ increase with temperature in a linear relationship between $\log(\sigma T)$ and 1000/T, and suggest their conduction belongs to the

small polaron hopping mechanism. [122, 156-158] Their activation energies are 0.53 eV and 0.55 eV, respectively, which were calculated from the slope of the fitting line in Fig. 5.13. Their conductivities at 800 ^{o}C are close to each other, about half of that of $Mn_{1.5}Co_{1.5}O_4$. The results may suggest the Co/Ni ratio might not influence the conductivity when Mn composition is kept fixed.

5.4 Conclusions

Ni and Cu-doped $(Mn,Co)_3O_4$ spinel oxides were synthesized by solid-state reaction method to investigate the effects of nickel and copper doping on the interaction with chromia at high temperature. Their Cr content profiles indicate a two-scale reaction layer, and Co/Mn ratio in the outer layer is much higher than 1 in the original $Mn_{1.5-0.5x}Co_{1.5-0.5x}TM_xO_4$ samples. As for the reaction at 800 ^{o}C, Ni is not detected in the Cr-rich reaction layer, while copper appears in this region where its content was comparable to the original Cu level in the spinel oxide. The different behavior of Cu in the mass transport from other dopants could be probably related to the preference for the cation occupancy in the spinel oxide. Further increasing reaction temperature (e.g. 1000^{o}C), Ni was observed to diffuse outwards into the reaction layer in which its content also increases. The Co/Ni ratio was shown to have effect on the interface composition after reaction with chromia, but the thickness of reaction layer does not change. The electrical conductivities of $Mn_{1.5}CoNi_{0.5}O_4$ and $Mn_{1.5}Co_{0.6}Ni_{0.9}O_4$ are close and high enough for the ceramic coating. As for Ni and Cu-doped $(Mn,Co)_3O_4$ samples, their thicknesses of the reaction layer are similar to that of $Mn_{1.5}Co_{1.5}O_4$, therefore their potential as the coating to SOFC interconnect needs further investigation. These two

transition metal dopants showed different mass transport behavior in the reaction with chromia, which is helpful for the dopant identification and the study on the interaction between spinel coating and oxides scale during long-term operation.

CHAPTER 6

Conclusions and Perspectives

The oxidation of SOFC metallic interconnects and chromium volatilization can cause cathode poisoning and cell degradation. Ceramic conductive coating can provide long-term protection for the alloy interconnects. Manganese cobalt spinel oxides have demonstrated promising performances as coating material for metallic interconnect. However, the reasons for their excellent properties have not been completely understood. In this work, the interaction between $(Mn,Co)_3O_4$ spinel coatings and chromia and the transport properties and phase stability of the reaction layer are investigated to provide a fundamental understanding of $(Mn,Co)_3O_4$ coating in high-temperature operation. In addition, the effects of different transition metal dopants in the coating material on the mass transport behavior were studied for the development of improved coatings.

After reaction, the interfaces of $(Mn,Co)_3O_4$ in contact with Cr_2O_3 are shown a facetted dense morphology. At the steady state (e.g. 1200^oC), this outer reaction layer has a chemical composition of $(Mn,Co)Cr_2O_4$ with a cubic spinel structure, in which the chromium content is achieved to the maximum 2 Cr per M_3O_4 unit. Their cations concentration profiles of the cross section and the location of platinum markers indicate the reaction layer between $(Mn,Co)_3O_4$ and Cr_2O_3 contains two scales, Cr-rich $(Mn,Co)Cr_2O_4$ outer scale and

Cr-containing $(Mn,Co,Cr)_3O_4$ intermediate scale. In the outer layer in contact with Cr_2O_3, $(Mn,Co)Cr_2O_4$ grows by the outward diffusion of cobalt and manganese from $(Mn,Co)_3O_4$ coating material. At the same time, chromium diffuses into $(Mn,Co)_3O_4$ and formed the $(Mn,Co,Cr)_3O_4$ intermediate layer. At low reaction temperature (800^oC and 900^oC), the growth of the Cr-rich outer layer becomes dominant, which is beneficial to block the diffusion of chromium species.

To evaluate the long-term stability, the properties of the reaction layer between the $Mn_{1.5}Co_{1.5}O_4$ coating and Cr_2O_3 scale formed on the alloy surface needs further characterization. $Mn_{1.5-0.5x}Co_{1.5-0.5x}Cr_xO_4$ (x = 0 - 2) were prepared to investigate their electrical properties, cation distributions and thermal expansion behavior at high temperature. With increasing Cr content the cubic crystal structure is stabilized, the electrical conductivity and thermal expansion coefficient both decrease. The temperature dependence of conductivities in $Mn_{1.5-0.5x}Co_{1.5-0.5x}Cr_xO_4$ indicates their conduction is through a small polaron hopping mechanism. $Mn_{1.5}Co_{1.5}O_4$ and $MnCoCrO_4$ were chosen for the neutron diffraction at SOFC operation temperature. The cation distributions determined from neutron data show Cr had stronger preference on octahedral sites compared with Mn and Co, which could suggest why Cr diffusion leads to reduction in conductivity of the spinel coating after operation. The tetrahedral site preference of Co over Mn may give the reason for higher Co/Mn ratio in the reaction layer than the original. Therefore, reducing the thickness of Cr-containing reaction layer between the oxide scale and the spinel coating could improve the overall electrical conduction and avoid local spallation of ceramic coating.

Different transition metal substitutions were also studied in this work. The effects of Fe

doping in $MnCo_{2-x}Fe_xO_4$ (x = 0.15 - 0.7) spinel oxides were investigated on the reaction with chromia and electrical property at high temperature. Their lattice parameter expands as increasing iron content due to its larger cation size than that of cobalt. It is interesting to note that even iron content is increased to 0.7, it is not detected in the Cr-rich reaction layer, which would reflected that Fe may not prefer the tetrahedral site as Co and Mn during the reaction with Cr_2O_3. The electrical conductivity of $MnCo_{1.66}Fe_{0.34}O_4$ at 800 ^oC is close to that of $Mn_{1.5}Co_{1.5}O_4$, the current promising spinel coating material.

$MnCo_{1.66}Ti_{0.34}O_4$ was also prepared to compare the effect of doping with iron and titanium. Their thicknesses of reaction layer formed are depressed when compared with $Mn_{1.5}Co_{1.5}O_4$. The CTE of $MnCo_2O_4$ can be also effectively decreased after iron and titanium doping. Similar to iron, no titanium is detected in the outer reaction layer. Ti cations prefer the octahedral site in spinel oxides, and the observed phenomenon may suggest Ti would not like the tetrahedral sites during the interaction. The conductivity of $MnCo_{1.66}Ti_{0.34}O_4$ is lower than that of $MnCo_{1.66}Fe_{0.34}O_4$ at high temperatures.

In addition, the effects of nickel and copper doping on the interaction with chromia at high temperature were evaluated. Ni is not detected in the Cr-rich reaction layer after reaction at 800 ^oC. However, when the reaction temperature is further increased (e.g. 900 ^oC and 1000 ^oC), Ni is observed to diffuse outward into the reaction layer in which its content increases with the temperature. Improving Ni content in the spinel oxides and reaction temperature are found to promote Ni diffusion into the Cr-rich region. As for the Cu doped samples, copper appears in the reaction layer even with a low level at x = 0.2 after reaction at 800 ^oC. The different behavior in mass transport between nickel and copper could suggest they may

possess different site preference. The differences in the mass transport behavior of transition metal dopants studied in our work provide useful information to identify new spinel coatings.

The proposed future work to further understanding the interaction between the $(Mn,Co)_3O_4$ spinel coating materials and chromia scale and the compatiblilty of the reaction layer with coating material and oxidation scale related to SOFC interconnect application are as the following:

When the interconnect alloy is coated with dense spinel coating, there will be oxygen partial pressure gradient through the interface of coating/scale to the coating layer during SOFC working condition. The interaction of $(Mn,Co)_3O_4$ with Cr_2O_3 during the reaction under low oxygen partial pressure will be investigated. The samples preparation will be the same as this work, but the reaction atmosphere will be controlled at low level of oxygen partial pressure (e.g. 10^{-4} - $10^{-0.7}$ atm, the pressure range on the cathode side [2]). The reaction will be performed first higher than the SOFC operation temperature to overcome kinetic limitations, and then at 800^{o}C. The phase structure of the reaction will be examined by XRD. Their reaction interface morphologies, compositions and the mass transport of the reaction layer are studied by SEM and EDS. The cation distribution in the reaction region under low oxygen pressure will be analyzed to learn the mass transport from neutron diffraction. The effect of low oxygen pressure on the growth rate of the reaction layer will be compared with that in air of this work for the same reaction temperature.

The effect of low oxygen pressure will be tested on the properties of the reaction scales. $(Mn,Co,Cr)_3O_4$ spinel oxides will be prepared for bulk analyses of the reaction layer. The electrical conductivities and CTE will be measured at low oxygen partial pressure. The

oxygen partial pressure dependence of the conduction behavior of $(Mn,Co,Cr)_3O_4$ at 800 ^oC will be investigated, which can provide better understanding of effect of the raction layer on the cell resistance for SOFC coating application.

This work focus on the interaction behavior between the Cr-free spinel oxides and Cr_2O_3, and theses spinel oxides are expected to suppress the chromium migration problems. The $MnCo_{1.66}Fe_{0.34}O_4$ and $MnCo_{1.66}Ti_{0.34}O_4$ are observed to depress the growth of the reaction layer, so the long-term stability of $MnCo_{1.66}Fe_{0.34}O_4$, $MnCo_{1.66}Ti_{0.34}O_4$ and $Mn_{1.5}Co_{1.5}O_4$ coating applied on the surface of alloy interconnect will be studied. The coated alloys will be oxidized at dual atmospheres at 800 ^oC (e.g. in air and H_2/H_2O, respectively) to simulate the SOFC working condition. After oxidation, the microstructures of the coating and will be characterized by SEM. The mass transport behavior (e.g. cations concentration gradient, thickness growth of the reaction layer formed between the coating and scale) will be analyzed by SEM and EDS. The mass transport behavior of dopant will be compared with results of bulk analysis in this work. The coated alloys will also be evaluated in the weight gain and ASRs. The comparison work between bulk and coating analyses can give useful information to further understand the transport property of the spinel coatings during operation.

REFERENCES

[1] O. Yamamoto, Solid oxide fuel cells: Fundamental Aspects and Prospects, *Electrochimica Acta*, 45(2000) 2423–2435.

[2] W. Z. Zhu, and S.C. Deevi, Development of interconnect materials for solid oxide fuel cells, *Mater. Sci. Eng. A,* 348 (2003) 227- 243.

[3] S. C. Singhal, K. Kendall, High temperature solid oxide fuel cells: Fundamentals, Design and Applications, *Elsevier Advanced Technology,* Oxford, UK, 2003.

[4] N. Q. Minh, Ceramic fuel cells, *J. Am. Ceram. Soc.,* 76 (1993) 563-588.

[5] M. Mori, T. Yamamoto, H. Itoh, and T. Watanabe, Compatibility of alkaline earth metal (Mg, Ca, Sr) - doped lanthanum chromites as sparators in planar-type high-temperature solid oxide fuel cells, *J. Mater. Sci.,* 32 (1997) 2423-2431.

[6] D. Bhattacharyya, and R. Rengaswamy, A Review of Solid Oxide Fuel Cell (SOFC) Dynamic Models, *Ind. Eng. Chem. Res.,* 48 (2009) 6068 - 6086.

[7] A. Boudghene Stambouli, and E. Traversa, Solid oxide fuel cells (SOFCs): a review of an environmentally clean and efficient source of energy, *Renewable and Sustainable Energy Reviews,* 6 (2002) 433 -455.

[8] M. C. Williams, J. P. Strakey, and W. A. Surdoval, The U.S. Department of Energy, Office of Fossil Energy Stationary Fuel Cell Program, *J. Power Sources,* 143 (2005) 191-196.

[9] P. Singh, and N. Q. Minh, Solid oxide fuel cells: Technology status, *Int. J. Appl. Ceram. Technol,* 1 (2004) 5-15.

[10] L. Blum, W. A. Meulenberg, H. Nabielek, and R. S. Wilckens, Worldwide SOFC technology overview and benchmark, *Int. J. Appl. Ceram. Technol,* 2 (2005) 482-492.

[11] N. Sakai, H. Yokokawa, T. Horita, and K. Yamaji, Lanthanum chromite-based internonnects as key materials for SOFC stack development, *Int. J. Appl. Ceram. Technol,* 1 (2004) 23-30.

[12] W. Vielstich, A. Hubert, M. Gasteiger and A. Lamm, Handbook of fuel cells – Fundamentals, Technology and Applications, *Willy*, New York, 2003.

[13] H. Yokokawa, N. Sakia, T. Kawada, and M. Dokiya, $LaCrO_3$-Based perovskites, *J. Electronchem. Soc.,* 138 (1991) 1018-1027.

[14] M. Mori, Y. Hiei, and N. M. Sammes, Sintering behavior of Ca- or Sr-doped $LaCrO_3$ perovskites including second phase of $AECrO_4$ (AE = Sr, Ca) in air. *Solid State Ionics,* 135 (2000) 743-748.

[15] M. Mori, and N. M. Sammes. Sintering and thermal expansion characterization of Al-doped and Co-doped lanthanum strontium chromites synthesized by the Pechini method, *Solid State Ionics,* 146 (2002) 301-312.

[16] M. Mori, T. Yamamoto, T. Ichikawa, et al. Dense sintered conditions and sintering mechanisms for alkaline earth metal (Mg, Ca and Sr) - doped $LaCrO_3$ perovskites under reducing atmosphere, *Solid State Ionics,* 148 (2002) 93-101.

[17] S. Simmer, J. Hardy, J. Stevenson, et al, Sintering of non-stoichiometric strontium doped lanthanum chromite, *J. Mater. Sci. Lett.,* 19 (2000) 863-865.

[18] M. Mori, Y. Hiei, and N. M. Sammes, Sintering behavior and mechanism of Sr-doped lanthanum chromites with A site excess composition in air, *Solid State Inoics*, 123(1999) 103-111.

[19] N. M. Sammes, R. Ratnaraj, and M. G. Fe, The effect of sintering on the mechanical properties of SOFC ceramic interconnect materials, *J. Mater. Sci.*, 29 (1994) 4319-4324.

[20] L. W. Tai, and P. A. Lessing, Tape casting and sintering of strontium-doped lanthanum chromite for a planar solid oxide fuel cell bipolar plate, *J. Am. Ceram. Soc.*, 74 (1991) 155- 160.

[21] J. W. Fergus, Lanthanum chromite-based materials for solid oxide fuel cell interconnects. *Solid State Ionics*, 171 (2004) 1-15.

[22] B. Barnes, $La_{1-x}Sr_xMnO_3$ based ceramics for use in solid oxide fuel cells, *MS. Thesis.* Queen's university, Kingston, Ontario, CA, 2003.

[23] K. P. Bansal, S. Kumari, B. K. Das, et al, On some transport properties of strontium-doped lanthanum chromite ceramics, *J. Mater. Sci.*, 18 (1983) 2095-2100.

[24] I. Yasuda, and T. Hikita, Electrical conductivity and defect structure of calcium - doped lanthanum chromites, *J. Electrochem. Soc.*, 140 (1993) 1699-704.

[25] S. Jiang, L. Liu, K. P. Ong, P. Wu, J. Li, and J. Pu, Electrical conductivity and performance of doped $LaCrO_3$ perovskite oxides for solid oxide fuel cells, *J. Power Sources*, 176 (2008) 82–89.

[26] K. P. Ong, P. Wu, L. Liu, and S. Jiang, Optimization of electrical conductivity of $LaCrO_3$ through doping: A combined study of molecular modeling and experiment, *Appl. Phys. Lett.* 90 (2007) 1-3.

[27] M. Mori, Y. Hiei, and T. Yamamoto, Control of the thermal expansion of stronitium-doped lanthanum chromite perovskites by B-site doping for high - temperature solid oxide fuel cell separators, *J. Am. Ceram. Soc.,* 84 (2001) 781-786.

[28] S. Srilomsak，D. P. Schilling, and H. U. Anderson, Thermal expansion studies on cathode and interconnect oxide, *Proceedings of the First International Symposium on Sold Oxide Fuel Cells,* The Electrochemical Society, Pennington, NJ, 1989, 129-140.

[29] M. Mori, H. Miyamoto, K. Takenobu, and T. Matsudaira, Controlling the chromite expansion under reductive atmosphere, *in: Proceedings of 2nd European Solid Oxide Fuel Forum,* Oslo, Norway, 1996, 541-546.

[30] P. Duran, J. Tartaj, F. Capel, and C. Moure. Formation, sintering and thermal expansion behaviour of Sr- and Mg-doped $LaCrO_3$ as SOFC interconnector prepared by the ethylene glycol polymerized complex solution synthesis method. *J. Euro. Ceram. Soc.,* 24 (2004) 2619–2629.

[31] A. J. McEvoy, Thin SOFC electrolytes and their interfaces – A near-term research strategy, *Solid State Inoics,* 132 (2000) 159-165.

[32] H. Moon, S. D. Kim, S. H. Hyun, and H. S. Kim, Development of IT-SOFC unit cells with anode-supported thin electrolytes via tape casting and co-firing, *Int. J. Hydrogen Energy*, 33 (2008) 1758-1768.

[33] B. Zhu, and M. D. Mat, Studies on dual phase ceria-based composites in electrochemistry, *Int. J. Electrochem. Sci.,* 1 (2006) 383-402.

[34] A. Moure, A. Castro, J. Tartaj, and C. Moure, Single-phase ceramics with $La_{1-x}Sr_xGa_{1-y}Mg_yO_{3-t}$ composition from precursors obtained by mechanosynthesis, *J. Power Sources,* 188 (2009) 489-497.

[35] Y. J. Leng, S. H. Chan, K. A. Khor, and S. P. Jiang, Performance evaluation of anode - supported solid oxide fuel cells with thin film YSZ electrolyte, *Int. J. Hydrogen Energy,* 29 (2004) 1025–1033

[36] Z. Yang, Recent advances in metallic interconnects for solid oxide fuel cells, *Intl Mater. Rev.,* 53 (2008) 39-16.

[37] K. Huang, P. Y. Hou, J. B. Goodenough, Characterization of iron-based alloy interconnects for reduced temperature solid oxide fuel cells, *Solid State Ionics,* 129 (2000) 237-250.

[38] J. Wu, and X. Liu, Recent development of SOFC metallic interconnect, *J. Mater. Sci. Technol.,* 26 (2010) 293-305.

[39] C. Wagner, Atom Movements, *Am. Soc. Metals,* Cleveland, OH (1951).

[40] K. Hauffe, Oxidation of Metals, *Plenum Press,* New York (1965).

[41] W. J. Quadakkers, H. Greiner, M. Hansel, A. Pattanaik, A. S. Khanana, E. Mallener, Compatibility of perovskite contact layers between cathode and metallic interconnector plates of SOFCs, *Solid State Ionics,* 91 (1996) 55-67.

[42] H. Hattendorf, R. Hojda, D. Naumenko, and A. Kolb-Telieps, A new austenitic alumina forming alloy: an aluminum-coated FeNi32Cr20, *Mater. Corro.,* 59 (2008) 449-454.

[43] N. Shaigan, W. Qu, D. G. Ivey, and W. Chen, A review of recent progress in coatings, surface modifications and alloy developments for solid oxide fuel cell ferritic stainless

steel interconnects, *J. Power Sources*, 195 (2010) 1529-1542.

[44] A. Holt, and P. Kofstad, Electrical conductivity and defect structure of Cr_2O_3. I. Higher temperatures (>~1000^{o}C), *Solid State Ionics*, 69 (1994) 127-136.

[45] A. Holt, and P. Kofstad, Electrical conductivity and defect structure of Cr_2O_3. II. Reduced temperatures (<~1000^{o}C), *Solid State Ionics*, 69 (1994) 137-143.

[46] W. C. Hagel, and A. U. Seybolt, Cation diffusion in Cr_2O_3, *J. Electrochem. Soc.*, 108 (1961) 1146-1152.

[47] H. Nagai, T. Fujikawa, and K. I. Shoji, Electrical Conductivity of Cr_2O_3 Doped with La_2O_3, Y_2O_3 and NiO, *Trans. Japan Inst. Met.*, 24 (1983) 581-588.

[48] P. Kofstad, Nonstoichometry, diffusion and electrical conductivity in binary metal oxides, *Robert E. Krieger Publishing Company*, Malabar, FL, 1983.

[49] Z. Yang, K. S. Weil, D. M. Paxton, and J. W. Stevenson, Selection and evaluation of heat-resistant alloys for SOFC interconnect applications, *J. Electrochem. Soc.*, 150 (2003) A1188-A1201.

[50] Y. F. Gu, H. Harada, and Y. Ro, Chromium and chromium-based alloys: Problems and possibilities for high-temperature service, *J. Minerals Metals Mater. Soc.*, 56 (2004) 28-33.

[51] A. H. Sully, Ductile Chromium and its Alloys, *Am. Soc. Metals*, Materials Park, OH, 1957.

[52] P. Kofstad, R. Bredesen, High temperature corrosion in SOFC environments, *Solid State Ionics*, 52 (1992) 69-75.

[53] S. Linderoth, P. V. Hendriksen, M. Mogensen, Investigations of metallic alloys for use

as interconnects in solid oxide fuel cell stacks, *J. Mater. Sci.*, 31 (1996) 5077-5082.

[54] J. Fergus, Metallic interconnects for solid oxide fuel cells, *Mater. Sci. Eng. A*, 397 (2005) 271-283.

[55] Y. Larring, R. Haugsrud, and T. Norby, HT corrosion of a Cr-5wt% Fe-1wt% Y_2O_3 alloy and conductivity of the oxide scale: Effects of water vapor, *J. Electrochem. Soc.*, 150 (2003) B374-B379.

[56] W. J. Quadakkers, H. Greiner, and W. Knock, *Proceedings of the First European Solid Oxide Fuel Forum,* Lucerne, Switzerland, (1994) 525.

[57] N. Lahl, D. Bahadur, K. Singh, L. Singheiser, and K. Hilpert, Chemical interactions between aluminosilicate base sealants and the components on the anode side of solid oxide fuel cells. *J. Electrochem. Soc.,* 149 (2002) A607-A614.

[58] D. M. England, and A. V. Virkar, Oxidation kinetics of some nickel based supperalloy foils and electronic resistance of the oxide scale formed in air Part I, *J. Electrochem. Soc.*, 146 (1999) 3196-3202.

[59] D. M. England, and A. V. Virkar, Oxidation kinetics of some nickel-based supperalloy foils in humidified hydrogen and electronic resistance of the oxide scale formed Part II, *J. Electrochem. Soc.*, 148 (2001) A330-A338.

[60] Z. Yang, G. Xia, and J. W. Stevenson, Evaluation of Ni-Cr-base alloys for SOFC interconnect applications, *J. Power Sources,* 160 (2006) 1104-1110.

[61] M. F. Rothman, and H. M. Tawancy, Low thermal expansion superalloy, *U.S. Pat. 4,818,486,* (1988).

[62] S. J. Geng, J. H. Zhu, and Z. G. Lu, Evaluation of Haynes 242 alloy as SOFC interconnect material, Solid State Inoics, 177 (2006) 559-568.

[63] S. J. Geng, J. H. Zhu, and Z. G. Lu, Investigation on Haynes 242 Alloy as SOFC Interconnect in Simulated Anode Environment, *Electrochem. Solid-State Lett.*, 9 (2006) A211-A214.

[64] P. Jablonski, and D. Alman, Oxidation resistance and mechanical properties of experimental low coefficient of thermal expansion (CTE) Ni-base alloys, *Int J. Hydro. Energy*, 32 (2007) 3705-3712.

[65] J. O. Anderson and B. Sundman, *CALPHAD: Comput. Coupling Phase Diagrams Thermochem.*, 11 (1987).

[66] Z. Yang, J. S. Hardy, M. S. Walker, G. Xia, S. P. Simner, and J. W. Stevenson, Structure and conductivity of thermally grown scales on ferritic Fe-Cr-Mn steel for SOFC interconnect applications, *J. Electrochem. Soc.*, 151 (2004) A1825-A1831.

[67] T. Brylewski, M. Nanko, T. Maruyama, K. Przybylski, Application of Fe-16Cr ferritic alloy to innterconnector for a solid oxide fuel cell, *Solid State Ionics*, 143 (2001) 131–150.

[68] N. K. Othman, J. Zang, D. J. Young, Temperature and water vapour effects on the cyclic oxidation behaviour of Fe–Cr alloys, *Corr. Sci.*, 52 (2010) 2827-2836.

[69] B. A. Pint, Experimental observations in support of the dynamic-segregation theory to explain the reactive-element effect, *Oxida. Met.*, 45 (1996) 1-37.

[70] E-Brite superferritic stainless steel (UNS S44627) product specifications, *from website: http://www.atimetals.com/products/Pages/e-brite.aspx.*

[71] S. Geng, and J. Zhu, Promising alloys for intermediate-temperature solid oxide fuel cell interconnect application, *J. Power Sources*, 160 (2006) 1009-1016.

[72] Crofer 22 APU material data sheet No. 4046, *from website:* http: //*www.thyssenkrupp-vdm.com/*.

[73] J. Robertson, The mechanism of high temperature aqueous corrosion of stainless steels, *Corro. Sci.*, 32 (1991) 443-465.

[74] Y. Liu, Performance evaluation of several commercial alloys in a reducing environment, *J. Power Sources*, 179 (2008) 286-291.

[75] S. Fontana, S. Chevalier, and G. Caboche, Metallic interconnects for solid oxide fuel cell: Effect of water vapor on oxidation resistance of differently coated alloys, *J. Power Sources*, 193 (2009) 136-145.

[76] E. Konysheva, U. Seeling, A. Besmehn, L. Singheiser, an K. Hilpert, Chromium vaporization of the ferritic steel Crofer22APU and ODS Cr5Fe1Y_2O_3 alloy, *J. Mater. Sci.*, 42 (2007) 5778-5784.

[77] Z. Lu, J. Zhu, E. A. Payzant, M. P. Paranthaman, Electrical conductivity of the manganese chromite spinel solid solution, *J. Am. Ceram. Soc.*, 88 (2005) 1050-1053.

[78] J. Rufner, P. Gannon, P. White, M. Deibert, S. Teintze, R. Smith, and H. Chen, Oxidation behavior of stainless steel 430 and 441 at 800 degrees C in single (air/air) and dual atmosphere (air/hydrogen) exposures, *Int. J. Hydro. Energy*, 33 (2008) 1392-1398.

[79] N. Shaigan, D. G. Ivey, and W. Chen, Metal-oxide scale interfacial imperfections and performance of stainless steels utilized as interconnects in solid oxide fuel cells, *J. Elelctrochem. Soc.*, 156 (2009) 765-B770.

[80] Fuel Cell Interconnector, *from website: http://www.hitachimetals.com/.*

[81] A. Toji, and T. Uehara, Stability of oxidation resistance of ferritic Fe-Cr alloy for SOFC interconnects, *ECS Trans.*, 7 (2007) 2117-2124.

[82] A. Martinez-Villafane, J. G. Chacon-Nava, C. Gaona-Tiburcio, F. Almeraya-Calderon, G. Dominguez-Patino, and J. G. Gonzalez-Rodriguez, Oxidation performance of a Fe-13Cr alloy with additions of rare earth elements, *Mater. Sci. Eng. A*, 363(2003) 15-19.

[83] X. Yu and Y. Sun, The oxidation improvement of Fe3Al based alloy with cerium addition at temperature above 1000^{o}C, *Mater. Sci. Eng. A*, 363 (2003) 30-39.

[84] P. Y. Hou, J. Stringer, The effect of reactive elements additions on the selective oxidation growth and adhesion of chromia scales, *Mater. Sci. Eng. A*, 202 (1995) 1-10.

[85] W. J. Quadakkers, J. Piron-Abellan, V. Shemet, and L. Singheiser, Metallic interconnectors for solid oxide fuel cells - a review, *Mater. High Temp.*, 20 (2003) 115-127.

[86] S. Geng, J. Zhu, M. P. Bardy, H. U. Anderson, X. Zhou, and Z. Yang, A low-Cr metallic interconnect for intermediate-temperature solid oxide fuel cells, *J. Power Sources*, 172 (2007) 775-781.

[87] M. Monteiro, S. Saunders, and F. Rizzo, The effect of water vapour on the oxidation of high speed steel, kinetics and scale adhesion, *Oxida. Met.*, 75 (2011) 57-76.

[88] G. Hultquist, B. Tveten, and E. Hörnlund, Hydrogen in chromium: Influence on the high-temperature oxidation kinetics in H_2O, oxide-growth mechanisms, and scale adherence, *Oxida. Met.*, 54 (2000) 1-10.

[89] Y. Matsuzaki, and I. Yasuda, Electrochemical properties of a SOFC cathode in contact

with a chromium-containing alloy separator, *Solid State Ionics*, 132 (2000) 271-278.

[90] Y. Matsuzaki, and I. Yasuda, Dependence of SOFC cathode degradation by chromium-containing alloy on compositions of electrodes and electrolytes, *J. Elelctrochem. Soc.*, 148 (2001) A126.

[91] S. P. Jiang, J. P. Zhang, L. Apateanu, and K. Foger, Deposition of chromium species at Sr-doped $LaMnO_3$ electrodes in solid oxide fuel cells. I. Mechanism and kinetics, *J. Elelctrochem. Soc.*,147 (2000) 4013-4022.

[92] S. P. Jiang, J. P. Zhang, L. Apateanu, and K. Foger, Deposition of chromium species at Sr-doped $LaMnO_3$ electrodes in solid oxide fuel cells. II. Effect on O_2 reduction reaction, *J. Elelctrochem. Soc.*,147 (2000) 3195-3205.

[93] S. P. Jiang, J. P. Zhang, L. Apateanu, and K. Foger, Deposition of chromium species at Sr-doped $LaMnO_3$ electrodes in solid oxide fuel cells. III. Effect of Air Flow, *J. Elelctrochem. Soc.*,148 (2001) C447.

[94] H. Asteman, J. E. Svensson, and L. G. Johansson, Evidence for chromium evaporation influencing the oxidation of 304L: The effect of temperature and flow rate, *Oxida. Met.*, 57 (2002) 193-216.

[95] P. Wei, Spinel coatings for solid oxide fuel cell interconncts and crystal structure of Cu-Mn-O, *Thesis, McMaster University*, 2009.

[96] D. Chatterjee, and S. Biswas, Development of chromium barrier coatings for solid oxide fuel cells, *Int. J. Hydro. Energy*, 36 (2011) 4530-4539.

[97] H. Yokokawa, T. Horita, N. Sakai, K. Yamaji, M. E. Brito, Y. P. Xiong, and H. Kishimoto, Thermodynamic considerations on Cr poisoning in SOFC cathodes, *Solid*

State Ionics, 177 (2006) 3193-3198.

[98] C. Sun, R. Hui, and J. Roller, Cathode materials for solid oxide fuel cells: a review, *J. Solid State Electrochem.*, 14 (2010) 1125-1144.

[99] Z. Shao, and S. M. Haile, A high-performance cathode for the next generation of solid-oxide fuel cells. *Nature*, 431 (2004) 170-173.

[100] C. Fu, K. Sun, X. Chen, N. Zhang, and D. Zhou, Electrochemical properties of A-site deficient SOFC cathodes under Cr poisoning conditions, *Electrochim. Acta*, 54 (2009) 7305-7312.

[101] B. Liu, Y. Gu, L. Kong, Y. Zhang, Evaluation of nano-structured $Ir_{0.5}Mn_{0.5}O_2$ as a potential cathode for intermediate temperature solid oxide fuel cell, *J. Power Sources*, 185 (2008) 946-951.

[102] G. Y. Lau, M. C. Tucker, C. P. Jacobson, S. J. Visco, S. H. Gleixner, and L. C. DeJonghe, Chromium transport by solid state diffusion on solid oxide fuel cell cathode, *J. Power Sources*, 195 (2010) 7540-7547.

[103] A. Montenegro-Hernandez, J. Vega-Castillo, L. Mogni, and A. Caneiro, Thermal stability of $Ln_2NiO_{4+\delta}$ (Ln: La, Pr, Nd) and their chemicalcompatibility with YSZ and CGO solid electrolytes, *Int. J. Hydro. Energy*, 36 (2011) 15704-15714.

[104] Y. Li, M. W. Xu, and J. B. Goodenough, Electrochemical performance of $Ba_2Co_9O_{14}$ + SDC composite cathode for intermediate-temperature solid oxide fuel cells, J. Power Sources, 209 (2012) 40-43.

[105] W. J. Quadakkers, M. Hänsel, T. Rieck, Carburization of Cr-based ODS alloys in SOFC relevant environments, *Mater. Corros.*, 49 (1998) 252–258.

[106] W. Qua, J. Lia, and D. G. Iveyb, Sol-gel coatings to reduce oxide growth in interconnects used for solid oxide fuel cells, *J. Power Sources*, 138 (2004) 162-173.

[107] S. Chevalier, C. Valot, G. Bonnet, J. C. Colson, and J. P. Larpin, The reactive element effect on thermally grown chromia scale residual stress, *Mater. Sci. Eng. A*, 343 (2003) 257-264.

[108] S. Fontana, R. Amendola, S. Chevalier, P. Piccarod, G. Caboche, M. Viviani, R. Molins, and M. Sennour, Metallic interconnects for SOFC : characterization of corrosion resistance and conductivity evaluation at operating temperature of differently coated alloys, *J. Power Sources*, 171 (2007) 652-662.

[109] S.H. Kim, J.Y. Huh, J.H. Jun, J.H. Jun, J. Favergeon, Thin elemental coatings of yttrium, cobalt, and yttrium/cobalt on ferritic stainless steel for SOFC interconnect applications, *Curr. App. Phys.*, 10 (2010) S86-S90.

[110] R. Lacey, A. Pramanick, J. C. Lee, J. Jun, B. Jiang, D. D. Edwards, R. Naum, S. T. Misture, Evaluation of Co and perovskite Cr-blocking thin films on SOFC interconnects, *Solid State Ionics*, 181 (2010) 1294-1302.

[111] J. H. Zhu, Y. Zhang, A. Basu, Z. G. Lu, M. Paranthaman, D. F. Lee, and E. A. Payzant, $LaCrO_3$-based coatings on ferritic stainless steel for solid oxide fuel cell interconnect applications, *Surf. Coat. Technol.*, 177-178 (2004) 65-72.

[112] N. Shaigan, D. G. Ivey, and W. Chen, Co/$LaCrO_3$ composite coatings for AISI 430 stainless steel solid oxide fuel cell interconnects, *J. Power Sources*, 185 (2008) 331-337.

[113] W. J. Shong, C. K. Liu, C. Y. Chen, C. C. Peng, H. J. Tu, G. T. Fey, R. Y. Lee, and H. M. Kao, Effects of lanthanum-based perovskite coatings on the formation of oxide scale for ferritic SOFC interconnect, *Mater. Chem. Phys.*, 127 (2011) 45-50.

[114] G. V. Pattarkine, N. Dasgupta, and A. V. Virkar, Oxygen transport resistant of electrically conductive perovskite coatings for solid oxide fuel cell interconnects, *J. Electrochem. Soc.*, 155 (2008), B1036-B 1046.

[115] Z. Yang, G. Xia, G. D. Maupin, and J. W. Stevenson, Evaluation of perovskite overlay coatings on ferritic stainless steels for SOFC interconnect applications, *J. Electrochem. Soc.*, 153 (2006) A1852-A1858.

[116] R. V. Chopdekar, F. J. Wong, Y. Takamura, E. Arenholz, and Y. Suzuki, Growth and characterization of superconducting spinel oxide $LiTi_2O_4$ thin films, *Physica C: Superconductivity*, 469 (2009) 1885-1891.

[117] C.B. Carter, N.M. Grant, Ceramic materials: Science and Engineering, *Springer Science and Busines Media, LLC*, New York, USA, 2007.

[118] X. Liu and C. T. Prewitt, High-temperature X-ray diffraction study of Co_3O_4: Transition from normal to disordered spinel, *Phys. Chem. Miner.*, 17 (1990) 168 -172.

[119] S. Sasaki, Radial distribution of electron density in magnetite, Fe_3O_4, *Acta. Cryst.*, B53 (1997) 762-766.

[120] R. J. Harrison, S. A. T. Redfern, and H. S. C. O'Neill, The temperature dependence of the cation distribution in synthetic hercynite from in-situ neutron structure refinements, *Am. Miner.*, 83 (1998), 1092–1099.

[121] A. Petric, H. Ling, Electrical conductivity and thermal expansion of spinels at elevated

temperatures, *J. Am. Ceram. Soc.*, 90 (2007) 1515-1520.

[122] B. E. Martin, A. Petric, Electrical properties of copper–manganese spinel solutions and their cation valence and cation distribution, *J. Phys. Chem. Solids*, 68 (2007) 2262-2270.

[123] M. R. Bateni, P. Wei, X. Deng, A. Petric, Spinel coatings for UNS 430 stainless steel interconnects, *Surf. Coat. Technol.*, 201 (2007) 4677-4684.

[124] P. Wei, X. Deng, M.R. Bateni, A. Petric, Oxidation and electrical conductivity behavior of spinel coatings for metallic interconnects of solid oxide fuel cells, *Corrosion Science Section*, 63 (2007) 529-536.

[125] P. Wei, X. Deng, M. R. Bateni, and A. Petric, Oxidation behavior and conductivity of UNS 430 stainless steel and Crofer 22 APU with spinel coatings, *ECS Trans.*, 7 (2007) 2135-2143.

[126] B. Hua, W. Zhang, J. Wu, J. Pu, B. Chi, L. Jian, A promising $NiCo_2O_4$ protective coating for metallic interconnects of solid oxide fuel cells, *J. Power Sources*, 195 (2010) 7375-7379.

[127] Z. H. Bi, J. H. Zhu, and J. L. Batey, $CoFe_2O_4$ spinel protection coating thermally converted from the electroplated Co–Fe alloy for solid oxide fuel cell interconnect application, *J Power Sources*, 195 (2010), 3605-3611.

[128] Y, Liu, D. Y. Chen, Protective coatings for Cr_2O_3-forming interconnects of solid oxide fuel cells, *Inter J. Hydrogen Energy*, 34 (2009) 9220-9226.

[129] W. Zhang, J. Pu, B. Chi, and L. Jian, $NiMn_2O_4$ spinel as an alternative coating material for metallic interconnects of intermediate temperature solid oxide fuel cells, *J. Power Sources*, 196 (2011) 5591-5594.

[130] Z. Yang, G. Xia, X. Li, and J. W. Stevenson, $(Mn,Co)_3O_4$ spinel coatings on ferritic stainless steels for SOFC interconnect applications, *Inter J. Hydrogen Energy,* 32 (2007) 3648-3654.

[131] Z. Yang, G. Xia, C. Wang, Z. Nie, J. Templeton, J. W. Stevenson, and P. Singh, Investigation of iron-chromium-niobium-titanium ferritic stainless steel for solid oxide fuel cell interconnect applications, *J. Power Sources,* 183 (2008) 660-667.

[132] Y. Larring, and T. Norby, Spinel and perovskite functional layers between plansee metallic interconnect (Cr-5 wt % Fe-1 wt % Y_2O_3) and ceramic $(La_{0.85}Sr_{0.15})_{0.91}MnO_3$ cathode materials for solid oxide fuel cells, *J. Electrochem. Soc.*, 147 (2000) 3251-3256.

[133] X. Chen, P. Y. Hou, C. P. Jacobson, S. J. Visco, and L. C. De Jonghe, Prptective coating on stainless steel interconnect for SOFCs: oxidation kinetics and electrical properties, *Solid State Ionics,* 176 (2005) 425-433.

[134] J. J. Choi, J. Ryu, B. D. Hahn, W. H. Yoon, B. K. Lee, and D. S. Park, Dense spinel $MnCo_2O_4$ film coating by aerosol deposition on ferritic steel alloy for protection of chromic evaporation and low-conductivity scale formation, *J Mater Sci.,* 44 (2009): 843-848.

[135] B. Hua, Y. Kong, F. Lu, J. Zhang, J. Pu, and J. Li, The electrical property of $MnCo_2O_4$ and its application for SUS 430 metallic interconnect, *Chin. Sci. Bulletin*, 55 (2010) 3831-3837.

[136] Y. Fang, C. Wu, X. Duan, S. Wang, and Y. Chen, High-temperature oxidation process analysis of $MnCo_2O_4$ coating on Fe-21Cr alloy, *Inter. J. Hydro. Energy,* 36 (2011)

5611-5616.

[137] R. S. Roth, Phase Equilibria Diagrams, Fig. 9570, Vol. 11, *The American Ceramic Society,* Westerville, OH, 1995.

[138] Z. Yang, G. Xia, S. P. Simmer, J. W. Stevenson, Thermal growth and performance of manganese cobaltite spinel protection layers on ferritic stainless steel SOFC interconnects, *J. Electrochem. Soc.,* 152 (2005) A1896-A1901.

[139] X. Xin, S. Wang, Q. Zhu, Y. Xu, T. Wen, A high performance nano-structure conductive coating on a crofer22 APU alloy fabricated by a novel spinel powder reduction coating technique, *Electrochem. Commun.,* (2009), doi: 10.1016 /j.elecom.2009.10.031.

[140] X. Montero, F. Tietz, D. Sebold, H.P. Buchkremer, A. Ringuede, M. Cassir, A. Laresgoiti, I. Villarreal, $MnCo_{1.9}Fe_{0.1}O_4$ spinel protection layer on commercial ferritic steels for interconnect applications in solid oxide fuel cells, *J Power Sources,* 184 (2008) 172-179.

[141] X. Montero, N. Jordan, J. Piron-Abellan, F. Tietz, D. Stover, M. Cassir, and I. Villarreal, Spinel and Perovskite Protection Layers Between Crofer22APU and $La_{0.8}Sr_{0.2}FeO_3$ Cathode Materials for SOFC Interconnects, *J. Electrochem. Soc.,*156 (2009) B188 - B196.

[142] J. Wu, C. D. Johnson, R. S. Gemmen, X. Liu, The performance of solid oxide fuel cells with Mn–Co electroplated interconnect as cathode current collector. *J. Power Sources,* 15 (2009) 1106 -1113.

[143] W. Wei, W. Chen, and D. G. Ivey, Oxidation resistance and electrical properties of anodically electrodeposited Mn-Co oxide coatings for solid oxide fuel cell interconnect

applications, *J. Power Sources*, 186 (2009) 428-434.

[144] Z. Yang, G. Xia, G. D. Maupin, and J. W. Stevenson, Conductive protection layers on oxidation resistant alloys for SOFC interconnect applications, *Surf. Coat. Tech.*, 201 (2006) 4476-4483.

[145] M. J. Lewis, and J. H. Zhu, A process of synthesis $(Mn,Co)_3O_4$ spinel coatings for proctecting SOFC Interconnect Alloys, *Electrochem. Solid-State Lett.*, 14 (2011) B9-B12.

[146] E. Saoutieff, G. Bertrand, M. Zahid, and L. Gautier, APS deposition of $MnCo_2O_4$ on commercial alloys K41X used as solid oxide fuel cell interconnect: The importance of post heat-treatment for densification of the protective layer, *ECS Trans.*, 25 (2009) 1397-1402.

[147] A. Navrotsky, O.J. Kleppa, The thermodynamics of cation distributions in simple spinels, *J. Inorg. nucl. Chem.*, 29 (1967) 2701-2714.

[148] K. Wang, data report, Auburn, 2009.

[149] K. Wang, Y. Liu, J. W. Fergus, Interactions between SOFC interconnect coating materials and chromia, *J. Am. Ceram. Soc.*, 94 (2011) 4490-4495.

[150] W. Qu, L. Jian, J. M. Hill, and D. G. Ivey, Electrical and Microstructural Characterization of Spinel Phases as Potential Coatings for SOFC Metallic Interconnects, *J. Power Sources*, 153 (2006) 114-124.

[151] V. F. Sears, *Neutron News*, 3 (1992) 29-37.

[152] J. Rodriguez-Carvajal, *Proceedings of the Satellite Meeting on Powder Diffraction*, Toulouse, France (1990).

[153] JCPDS, International Center for Diffraction Data.

[154] A. Purwanto, A. Fajar, H. Mugirahardjo, J. W. Fergus, K. Wang, Cation distribution in spinel $(Mn,Co,Cr)_3O_4$ at room temperature, *J. Appl. Cryst,* 43 (2010), 394-400.

[155] R. D. Shannnon, Revised effective ionic radii and systematic studies of interatomic distance in Halides and Chalcogenides, *Acta. Cryst.*, A32 (1976) 751.

[156] R. Schmidt, A. Basu, and A. W. Brinkman, Small Polaron Hopping in Spinel Manganates, *Phys. Rev. B*, 72 (2005) 1-9.

[157] N. M. Kovtun, V. K. Prokopenko, and A. A. Shamyakov, Electroconductivity and Electron Exchange in Spinel Structures, *Solid State Comm.*, 26 (1978) 877-878.

[158] R. Schmidt, A. Basu, and A. W. Brinkman, Small polaron hopping in spinel manganates, *Phys. Rev. B*, 72 (2005) 1-9.

[159] H. Bordeneuve, A. Rousset, C. Tenailleau, and S. Guillement-Fritsch, Cation distribution in manganese cobaltite spinels $Co_{3-x}Mn_xO_4$ ($0 \leqslant x \leqslant 1$) determined by thermal analysis, *J. Therm. Anal. Calorim.*, 101 (2010) 137-142.

[160] S. Wang, X. Liu, Y. Feng, Q. He, and H. Wang, In situ high-temperature powder X-ray diffraction study on the spinel solid solutions $(Mg_{1-x}Mn_x)Cr_2O_4$, *Phys. Chem. Mater.*, (2011) 10.1007/s00269-011-0474-8.

[161] B. Gillot, J. L. Baudour, F. Bouree, R. Metz, R. Legros, and A. Rousset, Ionic configuration and cation distribution in cubic nickel manganite spinels $Ni_xMn_{3-x}O_4$ ($0.57<x<1$) in relation with thermal histories, *Solid State Ionics*, 58 (1992) 155-161.

[162] G. D. C. Csete de Gyorgyfalva, and I. M. Reaney, Decomposition of $NiMn_2O_4$ spinel: an NTC thermistor material, *J. Euro. Ceram. Soc.*, 21 (2001) 2145-2148.